METEOROLOGICAL DRIVERS OF ARCTIC RAIN-ON-SNOW EVENTS AND HOW CLIMATE CHANGE MAY INFLUENCE ASSOCIATED RISKS

by

JESSICA JANE VOVERIS

B.S., University of Oklahoma, 2013

A thesis submitted to the

Faculty of the Graduate School of the

University of Colorado in partial fulfillment

of the requirement for the degree of

Master of Arts

Department of Geography

2022

Committee Members:

Mark Serreze

Peter Blanken

John Cassano

Voveris, Jessica Jane (M.A., Geography)

Meteorological Drivers of Arctic Rain-on-Snow Events and How Climate Change May Influence Associated Risks

Thesis directed by Professor Mark Serreze

Much of what is known and recognized about the Arctic climate and weather patterns is dynamically changing due to anthropogenic warming, which may lead to both altered occurrences and strengthening of extreme events. Rain-on-snow or ROS events continue to produce extreme event criteria and impacts, especially when they occur over Arctic regions. These events generate hazards ranging from flooding to icing concerns for the transportation sector. Ecologists have studied how ROS events affect hooved animal species' ability to forage for their natural food sources – animals that are heavily relied upon by Indigenous Peoples. Ice growth resulting from ROS blocks access to food sources, leading to massive starvation events.

This research seeks to understand much of the meteorological setup of Arctic ROS events by focusing on five case studies of major events that led to serious impacts on the affected areas. From a synoptic scale standpoint, blocking patterns played leading roles in the initiation of ROS conditions over an area, with atmospheric rivers also lending to both direct and indirect effects in each ROS case. Other mesoscale features – like cyclone-induced low-level jets and resultant "warm noses" of higher air temperatures and moisture transport – represented other key features of ROS initiation. This study concludes by postulating how climate change may alter the severity and frequency of Arctic ROS events, drawing on this improved knowledge of weather patterns leading to ROS conditions.

ACKNOWLEDGEMENTS

The author would like to thank her committee chair and thesis advisor, Mark Serreze, for his support, time, and guidance provided throughout the development of this thesis, including the many hours spent reading and editing the final paper. The author would also like to thank her committee members, Peter Blanken and John Cassano, for their suggestions and patience throughout this process, made even more difficult by a once-in-a-hundred-years pandemic. The author singularly appreciates the suggestion from Peter Blanken to “think like a biologist” when working with case studies, and John Cassano’s passion for Arctic boundary layer weather and knowledge on the subject.

The author would also like to extend her gratitude to Christine Shields from the National Center for Atmospheric Research (NCAR), for providing additional references regarding atmospheric rivers and the suggestion to use HYSPLIT modeling analysis with this study, and Andrew Barrett from the National Snow and Ice Data Center (NSIDC), for his guidance in coding aspects utilized with this thesis.

ERA5 atmospheric reanalysis data was provided by the Copernicus Climate Data Store from the European Centre for Medium-Range Weather Forecasts (ECMWF). Code for the sounding data was provided through MetPy by Unidata, a community program with the University Corporation for Atmospheric Research (UCAR).

The author gratefully acknowledges the NOAA Air Resources Laboratory (ARL) for the provision of the HYSPLIT transport and dispersion model and/or READY website (https://www.ready.noaa.gov) used in this publication.

This study was supported by National Science Foundation Grant ICER 1928230 “NNA Track 1: A Systematic Pan-Arctic Analysis of Rain on Snow and Extreme Precipitation Events and their Impacts on Human-Environment Systems.”

CONTENTS

FIGURES

Chapter 1: Introduction

The Arctic is truly a fascinating geographic region, and the mechanisms that govern its weather and climate are just as interesting. In the context of this thesis, it is important that the factors that influence weather and climate are understood, both in terms of what makes this region unique and what it shares with middle latitudes. As will be seen, this understanding is crucial in determining why rain-on-snow (ROS) events in the Arctic – the topic of this thesis – are so impactful, and why a changing climate has implications for the occurrence of these events. General atmospheric science subjects will be covered in this chapter so that the reader has a grasp of the process driving not just the Arctic weather in general, but ROS events as well.

The Arctic remains, in some ways, an enigma. There are significant factors that make it different from regions in lower latitudes, especially when considering the range in the region's topography, how far north much of the region is located, and earth-system components affecting the climate, like the cryosphere. However, it does share some similarities with mid-latitude locations when it comes to the types of weather systems that frequent the region. Notably, this includes extratropical cyclones, associated features such as atmospheric rivers, and larger-scale aspects of the atmospheric circulation– including "blocking", that affects the movement and initiation of these features. This thesis shows how important these meteorological phenomena are to the formation of ROS events in the Arctic.

1.1: The Arctic Climate and Weather Systems

Many people associate the Arctic and Antarctic regions as dark, icy, and cold places for much of the year, but these lands represent much more than that.

Climatologists (specifically) classify much of the Arctic as a “polar desert,” a term Roger Barry and Mark Serreze use in their book *The Arctic Climate System* (Serreze and Barry 2014). Serreze and Barry (2014) use the term “polar desert” to describe a land that is both cold and dry. The average annual precipitation for these Arctic regions is 300 millimeters (12 inches) or less (Serreze and Hurst 2000). This is comparable to precipitation amounts for desert locations found across the globe, which may only receive up to 254 millimeters per year (or about 10 inches). However, in contrast to these hot and dry deserts, very low temperatures (at many times well below freezing) throughout much of the year represent a divergent characteristic for the Arctic. Persistent low temperatures largely account for these smaller precipitation ranges. The cold conditions limit the amount of moisture in the atmosphere and what is made available for precipitation generating storm systems to utilize (Serreze and Barry 2014).

The extreme seasonal range in the incident solar radiation at both polar regions represent a unique feature of the Earth System that directly leads to these extreme low temperatures in the Arctic, especially during the winter. Earth’s axial tilt regulates this trait, providing 24-hour darkness north of the Arctic circle through the winter months. The seasonally varying atmospheric temperature gradient that develops due to this differential solar heating, between the warm equatorial region and cold polar regions, becomes strongest in winter and weakest in summer and drives the overall poleward atmospheric energy flow in both hemispheres (Wallace and Hobbs 2006). In this sense, the Arctic plays a key role by acting as the Northern Hemisphere’s “heat sink,” as stated by Lackmann (2011) and referenced in Figure 1.1:

"Comparison of the net radiant heating curve with the outgoing radiant emission curve demonstrates the well-known result that the tropics, equatorward of roughly 30° latitude in either hemisphere (corresponding to the yellow shading in [Figure 1.1]), receive a surplus of radiant energy, that is, these regions emit less radiant energy per unit area to space than they absorb from the sun. Conversely, polar regions experience a net deficit of radiant energy, shaded light blue in (Figure 1.1)."

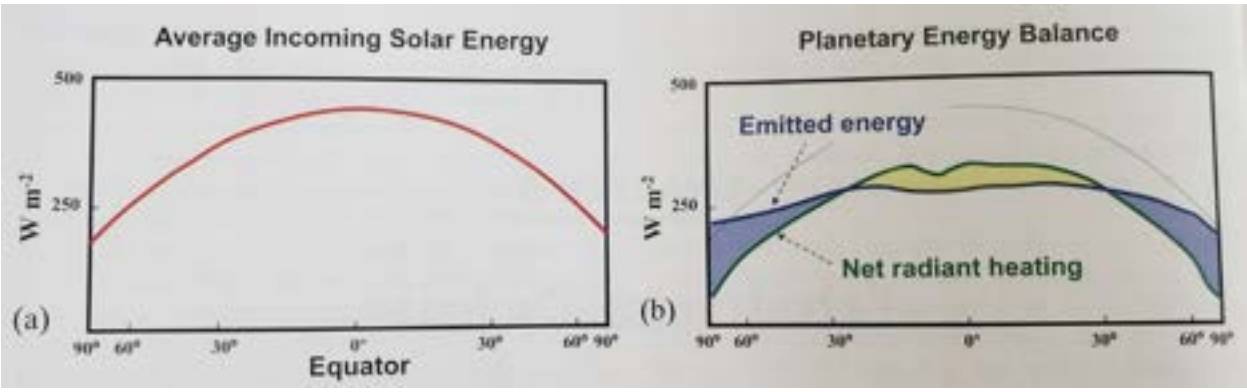

Figure 1.1: Global Average Incoming Solar Energy and Balance, courtesy of Lackmann (2011). (a) The average solar radiational flux reaching the top of the atmosphere dependent upon latitude. (b) The overall planetary energy balance, with thin black curve the same as in (a), green curve showing net radiant heating, and blue curve showing average outgoing radiant energy. Shading shows the difference between the blue and green curves.

At the macroscale concerning this energy transport, which includes the synoptic scale and highlights features in the upper levels, planetary waves consisting of troughs and ridges formed through differences in atmospheric pressure represent cores of fast moving, generally westerly (west-to-east moving) winds, known as the polar jet stream (Ahrens 2009). Troughs and ridges influence regional weather conditions that may be expected over a period of time through the general poleward transport of warm air and the equatorward transport of cold air. Jet stream winds represent and approximate (geostrophic) balance between the pressure gradient force, largely driven by this temperature difference between the poles and the equator, and the Coriolis force

associated with the earth's rotation (Ahrens 2009). These winds move at higher speeds during the winter in the Northern Hemisphere because this temperature gradient is at its strongest due to limited or no solar heating in the Arctic (Wallace and Hobbs 2006).

While the effects of atmospheric energy transport are large in the middle latitudes, cyclones, anticyclones, and the associated jet stream are no strangers to the higher latitudes. Extratropical cyclones tend to fall into spatial categories sized greater than 1000 kilometers and exist on time scales ranging from a few days to a few weeks (Ahrens 2009). Promoting lift of air parcels, extratropical cyclones and their associated fronts are an important driver of precipitation – albeit with generally low amounts in the Arctic. With this thesis, understanding ROS events requires understanding extratropical cyclones. Extratropical cyclones (sometimes referred to as extratropical lows, extratropical storms, or mid-latitude cyclones) rotate cyclonically (counterclockwise in the Northern Hemisphere) and are responsible for the atmospheric motions necessary for much of the global precipitation. Their anticyclonic counterparts spin clockwise (anticyclonically) in the Northern Hemisphere and are usually associated with fairer weather conditions and clearer skies.

The complete structure of an extratropical cyclone incorporates elements that extend from the surface to the upper levels of the atmosphere (Figure 1.2). In the upper atmospheric levels, the trough of the planetary wave train represents the cyclonic circulation at the jet stream level (Lackmann 2011). The associated surface low pressure system is typically displaced ahead of the upper-level trough; in the Northern Hemisphere, this is the eastern side of the trough, coinciding with the more northerly flow aloft (Lackmann 2011). This is especially true for an extratropical storm system experiencing strengthening or deepening (Lackmann 2011). Processes that lead to the movement or strengthening of these systems relate to quasi-geostrophic theory, which derives from two main processes that impact the change in local geopotential heights: 1) temperature advection and 2) the advection of vorticity, which is the advection of the clockwise or counterclockwise spin in the atmosphere (Lackmann 2011). In describing more of the meteorology, Howard Bluestein adds:

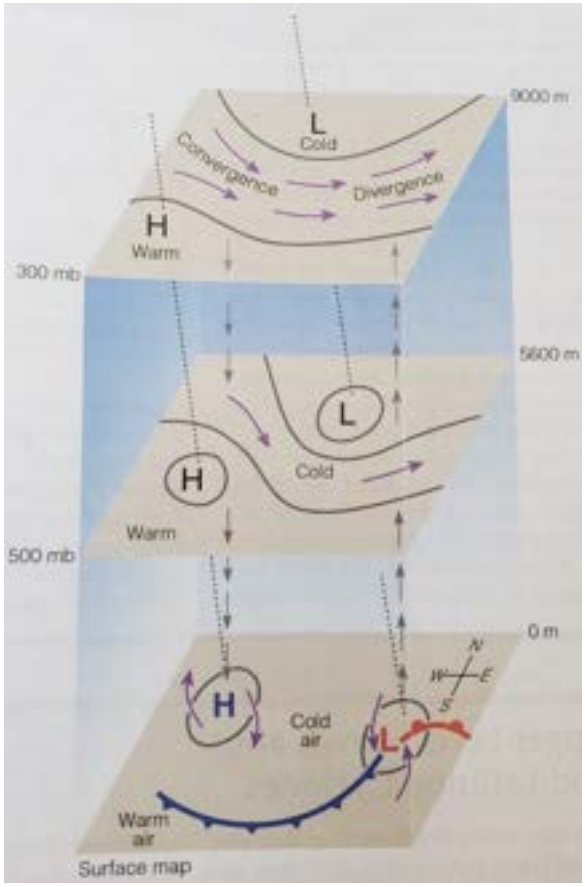

Figure 1.2: Extratropical Cyclone Structure, courtesy of Ahrens 2009. The standard surface to upper-level formation of an extratropical (middle-latitude) cyclone and anticyclone.

> "Warm advection at low levels downstream (relative to the flow in the middle troposphere; usually to the east or northeast in the Northern Hemisphere) from

the cyclone and cold advection upstream (usually to the west or southwest in the Northern Hemisphere) result in the movement of the surface cyclone approximately in the direction of the winds in the middle troposphere (i.e., toward the east or northeast). Anticyclogenesis occurs at the surface in response to the surface cold advection and vorticity advection becoming more anticyclonic with height upstream from the upper level trough," (Bluestein 1993).

Extratropical cyclones also incorporate various types of weather fronts, which play key roles in the temperature advection component and movement of air masses. When meteorologists refer to the differing densities of various air masses, this is most often due to temperature contrasts. Fronts represent the boundaries between these air masses, with moisture additionally influencing this process (Ahrens 2009). There are four primary front types that drive weather conditions: cold, warm, stationary, and occluded.

Cold fronts bring in dry and cold (usually stable) polar air, replacing the preceding moist and warm (conditionally unstable) subtropical air mass (Ahrens 2009). Cold fronts are areas where a meteorologist would find higher potential for precipitation or even severe weather due to the high temperature contrast between the air masses separated by the front, which provides the lifting mechanism necessary for precipitation (Ahrens 2009). Warm fronts represent a different dynamic, in that they push in moist and warm subtropical air to replace the diminishing dry, cold polar air; rising air along this type of front (frontal overrunning) also promotes precipitation (Ahrens 2009). Stationary fronts, the third type, have little to no movement (usually due to a very small temperature contrast between air masses), and these fronts depend on wind shifts (changes in

temperature or moisture advection) for progression (Ahrens 2009). The fourth frontal type is an occluded front – or occlusion – where (essentially) the cold front catches up to the warm front (Ahrens 2009).

While much of the Arctic is cold and dry (even polar desert-like), precipitation amounts vary widely across the region. Complex topography, geography, and influences from the cryosphere play large roles in the types of climate conditions a location may experience. The path of these extratropical cyclones will impact precipitation amounts across an area. Proximity to oceans or mountain ranges also affect both the weather and, consequently, local climate. One notable example of all these processes influencing Arctic climate is the terrain of Alaska, a topic that the author of this thesis gained expertise in as a National Weather Service operational meteorologist.

In Southeast Alaska, the waters of the northern Pacific and the overall atmospheric pattern, with progressive west to east moving storm systems, provide ample moisture for this part of the state. In addition, the inner channels and fjords, acting in concert with the Coast Mountains to the east, provide a source of enhanced orographic lift. Air masses forced up and over these landscapes of higher terrain work to produce additional precipitation for the Alaskan panhandle, and the precipitation amounts produced in this region qualify it as a temperate rainforest climate. Annual precipitation for Ketchikan, the southernmost city in the panhandle, receives 3,810 millimeters (about 150 inches) of precipitation per year, whereas Juneau, Alaska, the largest populated city in the panhandle, averages approximately 1,702 millimeters (or about 67 inches) per year; these data were obtained from the website

https://xmacis.rcc-acis.org/. The Aleutian Islands also receive heavy precipitation throughout the year by lying within the waters of both the Bering Sea and the warm North Pacific current. Southcentral Alaska has a comparable maritime weather pattern like Southeast Alaska but with the Brooks Range to the north providing enhanced orographic effects. On the opposite end of the spectrum, the North Slope and northern reaches of Alaska return to dry, polar desert-like conditions, primarily due to the rain shadow effect from the Brooks Range and the prevailing southern trajectory of storm systems through the state.

As with precipitation, many topographic and cryospheric features influence temperature. The presence of sea ice on the Arctic Ocean permits the surface air temperature to rise only to the melting point (or slightly above) in the summer months (Rigor, Colony, and Martin 2000; Serreze and Barry 2014). Locations with a more direct impact from continentality (more inland regions) may see surface air temperatures rise well above freezing during the summer months, but these temperatures then drop usually after the second half of August with waning insolation (Serreze and Barry 2014). Coastal regions tend to display a smaller annual range in air temperature, with the open water preventing temperatures from increasing or decreasing too quickly (Serreze and Barry 2014). Generally, the locations across the Arctic exhibiting extreme cold correlate to low precipitation amounts due to the Clausius-Clapeyron relationship:

$$e_s = e_0 * \exp\left(\frac{L}{R_v} * \left(\frac{1}{T_0} - \frac{1}{T}\right)\right)$$

This equation shows that for each 1 °C in warming this equates to a 6-7% increase in saturation vapor pressure. Consequently, precipitation occurring in this climate typically falls as snow for the majority of the year (Rigor, Colony, and Martin 2000).

The extreme seasonality in the higher latitudes influences polar environments on long timescales, with the planet's overall atmospheric circulation driven by the meridional temperature gradient between the poles and the equator. However, this extreme seasonality can also generate more localized effects at Arctic locations and on smaller timescales, especially with the total (or nearly total) darkness that occurs in Arctic winters. Arctic near surface temperature inversions are a prime example. Temperature inversions manifest during strong atmospheric stability and can form from extended periods of radiational cooling (Serreze, Kahl, and Schnell 1992). Radiational cooling involves a larger flux of outgoing longwave radiation during the polar winter. Other processes that lead to temperature inversions include warm air advection, subsidence, and surface melting of the snowpack (Serreze, Kahl, and Schnell 1992). Winter and autumn months exhibit the most favorable conditions for temperature inversions to occur because of the dearth of solar radiation (Serreze, Kahl, and Schnell 1992). In winter, the immediate surface temperature cools rapidly compared to the air layer found just above it (Bourne et al. 2010). In addition, warm air advection occurring above the inversion assists in generating more strongly stable environments (Bourne et al. 2010).

Air temperature inversions can influence meteorological conditions, such as the occurrence or onset of various precipitation types (rain versus snow versus freezing rain). Complex terrain may act to strengthen inversions in some cases. Valley locations

or low-lying areas are more susceptible to extreme temperature inversions due to cold air drainage and increased subsidence under strong anticyclonic conditions (Serreze, Kahl, and Schnell 1992). At Verkhoyansk Russia, the average winter change in temperature from the valley floor to the top of the inversion can be as large as 20 °C (Serreze, Kahl, and Schnell 1992). Heights of inversions across the Arctic have been found to extend from 300 meters up to 1200 meters in more extreme instances during the winter months (Serreze, Kahl, and Schnell 1992).

Additional key atmospheric features to understand in the context of this thesis include blocking patterns, atmospheric rivers (ARs), and their relationships to progressive extratropical cyclones. The American Meteorological Society defines blocking as “the obstructing, on a large scale, of the normal west-to-east progress of migratory cyclones and anticyclones,” (“Blocking - Glossary of Meteorology” n.d.). In addition:

> “A blocking situation is attended by pronounced meridional flow in the upper levels, often comprising one or more closed anticyclonic circulations at high latitudes and cyclonic circulations at low latitudes (cut-off highs and cut-off lows). This anomalous circulation pattern (the "block") typically remains nearly stationary or moves slowly westward, and persists for a week or more,” (“Blocking - Glossary of Meteorology” n.d.).

Atmospheric scientists have even discovered varying types of blocking patterns that occur within the overall atmospheric circulation (Figure 1.3). Blocks form primarily from a disruption in the normal west-to-east flow in the jet stream, which may be caused by any number of factors.

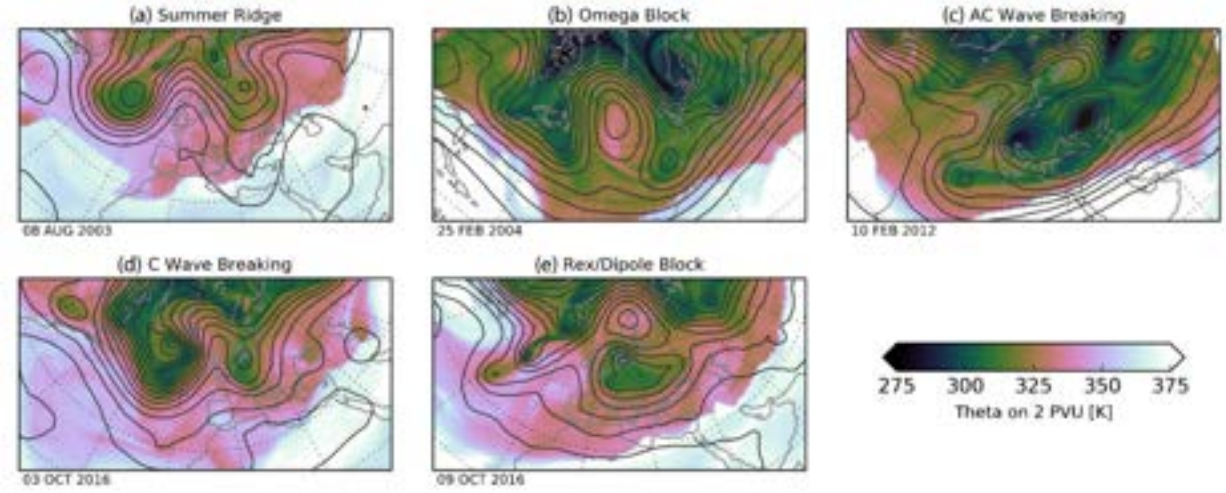

Figure 1.3: North Atlantic Blocking Types, courtesy of Woollings et al. (2018). The colored shading shows potential temperature on the dynamical tropopause (PV=2PV), and the black contours represent 500-mb geopotential heights with spacing of 60 meters.

Periodically, blocks may even result in a deep anticyclonic ridge of high pressure associated with a reversal in the normal westerlies to briefly become easterly (Woollings et al. 2018). Factors leading to these disruptions may include sea surface temperature anomalies, cryospheric influences (e.g., changes in sea ice coverage), impacts from teleconnections (e.g., El Niño-Southern Oscillation), and sudden stratospheric warming (SSW) events (Hall et al. 2015). SSW events result from upward tropospheric wave propagation that warms the stratosphere and disrupts the typical hemispheric polar vortex, which breaks down and reverses the natural meridional temperature gradient (Holton 2004).

The atmospheric scientist Daniel F. Rex conducted early research on blocking patterns and described his methodology for how to identify them, which many

researchers still use. He wrote that identification of a blocking pattern should be based on “the development of a particular contour pattern (circulation pattern) in the troposphere,” typically utilizing 500-mb constant pressure charts, and that “the pattern must persist with recognizable continuity for at least ten days,” (Rex 1950). However, alterations for the original definition have emerged – such as shorter time periods required and restrictions in occurrence based on latitude to not include semi-permanent anticyclones found in the subtropics (Barriopedro et al. 2006).

ARs represent an atmospheric phenomenon that shapes the movement of large amounts of moisture within the atmosphere. The American Meteorological Society’s accepted definition describes ARs as “a long, narrow, and transient corridor of anomalously strong horizontal water vapor transport that is typically located in the lowest 3 km of the troposphere and associated with a low-level jet stream ahead of the cold front of an extratropical cyclone,” (Ralph et al. 2017) The water vapor supplied to these systems usually has tropical or subtropical origins; this allows the system to produce heavy precipitation, especially when provided a surplus dose of lift through orographic ascent or by rising over the warm conveyer belt that originates in the cyclone’s warm sector (Ralph et al. 2017). Lackmann (2011) adds that extratropical cyclones accomplish much of the poleward transport of water vapor (and warm, moist air) but mentions that “a disproportionately large fraction of the total poleward moisture transport takes place within relatively narrow bands [ARs]. Ralph et al. (2017) conclude that over 90% of the poleward transport of moisture is accomplished by ARs in less than 10% of the zonal circumference of the planet. For comparison, it was also found that ARs carry 13-26 cubic kilometers per day of water vapor, which is an astonishing 7.5-15

times the daily average discharge at the mouth of the Mississippi River (Ralph and Dettinger 2011).

Atmospheric scientists in recent years identified connections between blocking patterns, specifically the blocking ridge or high, and AR development and genesis. For example, Benedict, Clement, and Medeiros (2019) identify a link between a retrograding ridge in the North Pacific and its influence on a landfalling AR in the US Pacific Northwest region. They concluded that the ridge was part of an atmospheric block. This study further described how the blocking "suppresses synoptic eddy activity over the central North Pacific while shifting the eddy-driven jet (storm track) equatorward roughly 7-10 days prior to AR landfall," (Benedict, Clement, and Medeiros 2019). Essentially, this process directs storm systems, some of which are linked to ARs and extreme precipitation events, to the US west coast (Benedict, Clement, and Medeiros 2019). Another study revealed similar traits, in that a blocked high pressure ridge in multiple cases enhanced moisture advection and increased integrated water vapor transport values (a key identifier of ARs), which led to large snowfall accumulations on the East Antarctic Coast (Gorodetskaya et al. 2014).

1.2: Implications of a Rapidly Changing North

Everything that we have come to understand about the Arctic climate and its weather systems is not immune to modification resulting from climate change. Sea ice extent is declining (Stroeve et al. 2012). Air temperature records are also being broken across the planet, especially during the winter and autumn months (Sommer et al. 2020; Viñas n.d.). Sea level has risen in the last few decades due primarily to both melting land ice and thermal expansion of the oceans (Moon et al. 2018). A powerful expression

of climate change, with significant implications for much of the Arctic, is Arctic amplification.

Arctic amplification refers to the observation that surface air temperatures are increasing at much higher rates in the Arctic than at lower latitudes, especially during the autumn through winter months (Figure 1.4) (Serreze and Barry 2011; Serreze et al. 2009; Serreze and Francis 2006). Climate models consistently show that Arctic amplification occurs as a response to enhanced greenhouse gas (GHG) concentrations from the burning of fossil fuels and the resulting increased radiative forcing (Serreze

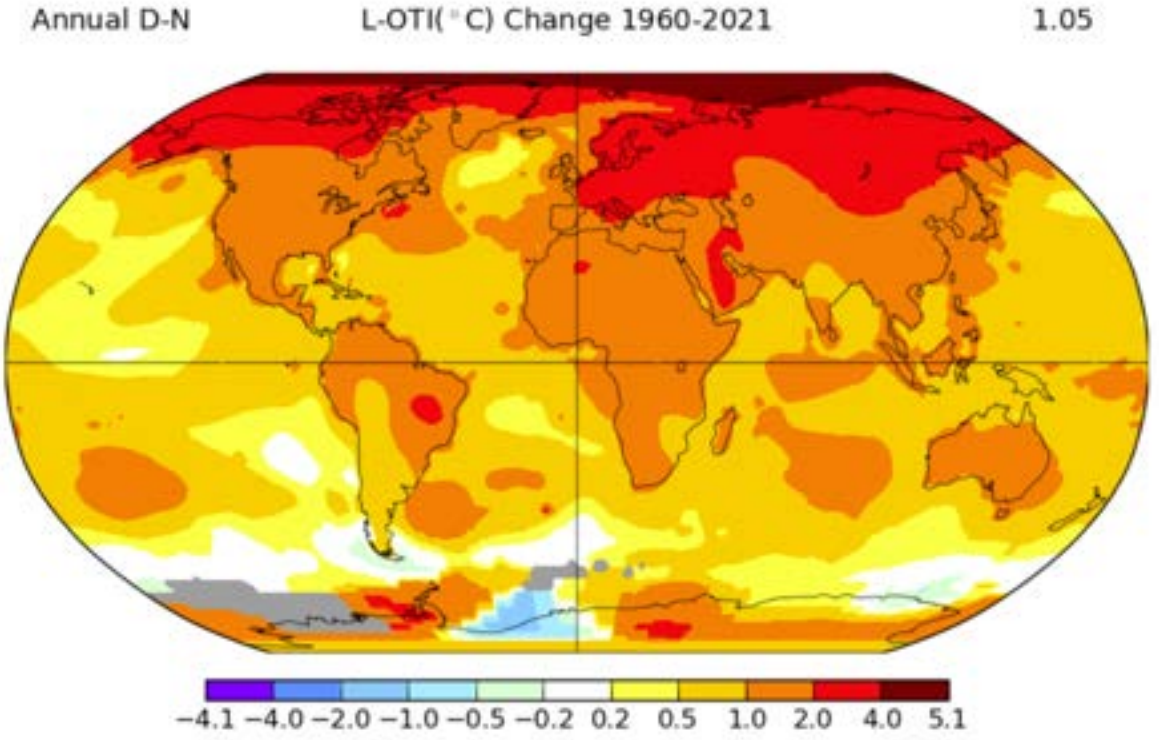

Figure 1.4: NASA GISS Temperature Analysis. This figure presents trends in annual mean surface air temperature from 1960–2021. L-OTI stands for Land-Ocean Temperature Index, which includes surface air temperatures from weather stations on land and water temperatures from ship and buoy reports.

and Barry 2011). A combination of feedback mechanisms is at work, predominantly involving changes in albedo from decreasing sea ice and changes in snow and land ice cover (Mark C. Serreze and Barry 2011). Albedo represents the fraction or ratio of

reflected incoming solar radiation redirected back to space. Serreze and Barry (2011) provide more detail regarding this change in albedo feedback:

> “Viewed in its simplest sense, initial warming will melt some of the Arctic's highly reflective (high albedo) snow and ice cover, exposing darker underlying surfaces that readily absorb solar energy, leading to further warming and further retreat of snow and ice cover. This feedback can work in reverse whereby initial cooling leads to expansion of the Arctic's snow and ice cover, leading to further cooling,” (Serreze and Barry 2011).

There are additional causes of Arctic amplification, and some processes may work in conjunction or tangentially to exacerbate its effects. Some studies point to sea ice loss as a primary cause of recent Arctic amplification through examinations of temperature with height, showing that the strongest Arctic warming is occurring at the surface (Screen and Simmonds 2010). Alternatively, sea ice loss alters the latent and sensible heat fluxes exchanged between open Arctic Ocean waters and the atmosphere above (Mark C. Serreze and Barry 2011). Serreze and Barry (2011) also address the uncertainty that comes with the effects from black carbon and other types of aerosols. With black carbon aerosols, these aerosol types have increased with the use of cleaner combustion technology; prior combustion methods primarily produced sulfate aerosols, which actually had a cooling effect because they reflected solar radiation (Serreze and Barry 2011). However, black carbon aerosols absorb solar radiation, creating a warming effect, and consequently, some climate models show that increasing black carbon aerosols in the atmosphere may have contributed to Arctic amplification (Serreze and Barry 2011).

There is growing urgency to determine how Arctic amplification may impact not just the Arctic climate system but also mid-latitude weather patterns and extreme weather events. As mentioned, the planet's overall atmospheric circulation is driven by differential solar heating, with planetary waves of troughs and ridges influencing the movement of cold and warm air masses through cyclone progression. Strong Arctic warming may disrupt the jet stream, and the body of research continues to expand in attempting to quantify how Arctic amplification may influence overall atmospheric circulations (Cohen et al. 2014; Francis and Vavrus 2012; Francis and Vavrus 2015; Screen and Simmonds 2013). As all latitudes, but especially northern latitudes, continue to see increasing temperatures, a warmer atmosphere also equates to more moisture made available for storm systems to utilize. Recall that the Clausius-Clapeyron equation dictates that each degree Celsius of warming results in a 6-7 percent increase in saturation vapor pressure. Consequently, higher temperatures may also increase evaporation rates. Furthermore, variations in cloud cover and water vapor concentrations in a more moist world may add to the feedback mechanisms relating to Arctic amplification by changing the longwave radiation flux, similar to how GHGs function (Serreze and Barry 2011). The rise in these two meteorological ingredients (warm air and moisture) represent important components for a very important type of weather phenomena becoming more prevalent across the Arctic, which is the focus of this thesis – rain-on-snow, or ROS, events.

1.3: Background on Arctic Rain-on-Snow (ROS) Events

ROS events occur when liquid precipitation, in the form of rain or freezing rain, falls overtop of an existing snowpack (Figure 1.5) (Bieniek et al. 2018; Grenfell and

Putkonen 2008; Rennert et al. 2009; Serreze et al. 2021). Air temperatures in the region of ROS occurrence generally increase dramatically preceding the onset of precipitation, but this increase typically occurs over a relatively short time period (Hansen et al. 2014; Rennert et al. 2009; Serreze et al. 2021). Near surface air temperatures may rise quickly enough to cause solid forms of precipitation to melt or to induce rain throughout the entirety of the event. For cases in the Arctic, recent research shows that air temperatures then decrease following the event, in many instances to well below freezing (Serreze et al. 2021). This allows the accumulated liquid from the event to freeze and form a thick glaze of ice along the surface of the snow layer (Serreze et al. 2021). This process likely results from the extratropical storm system (that generated the initial precipitation) advancing onward, with a cold front then progressing through the area (Rennert et al. 2009).

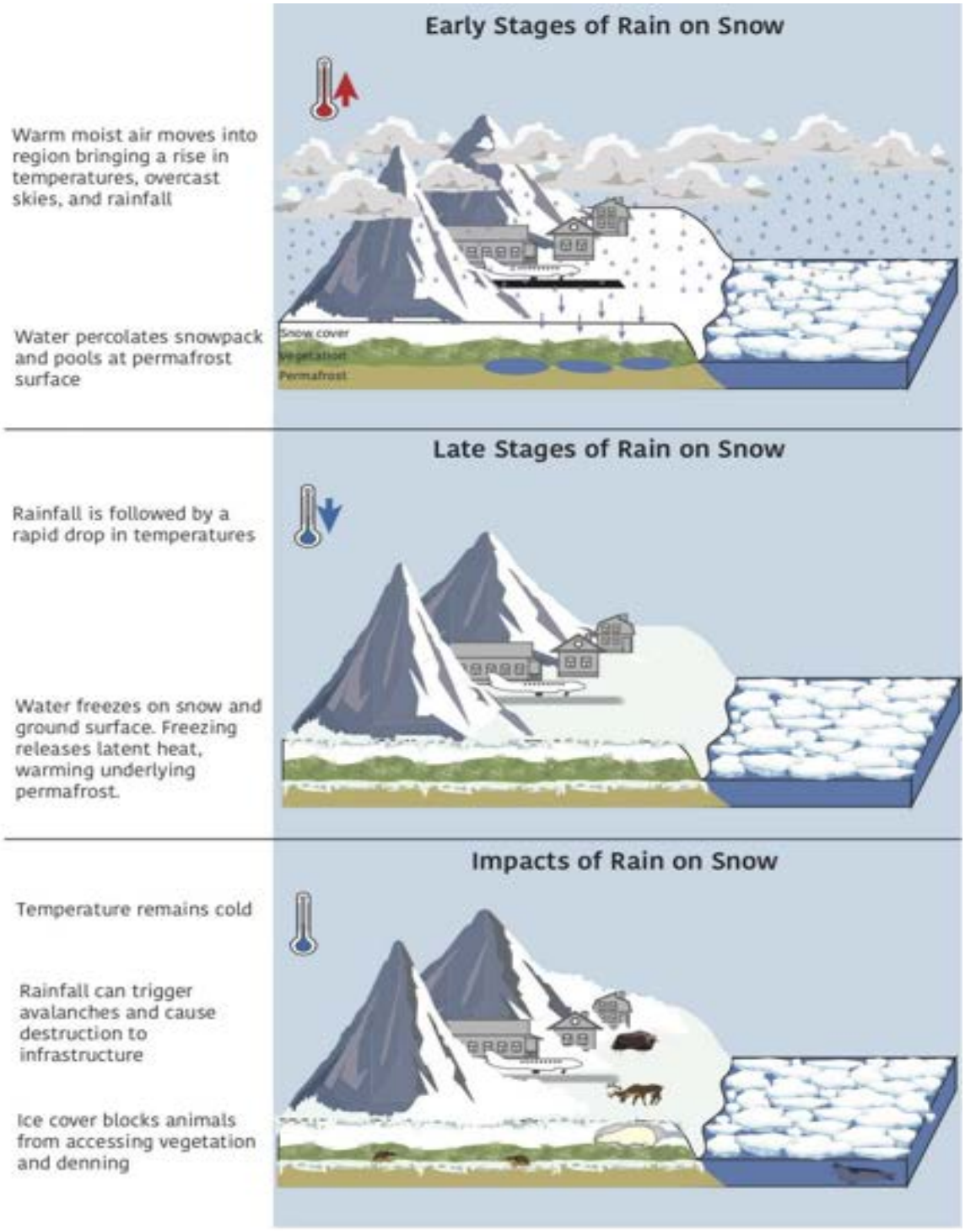

Figure 1.5: ROS Setup and Impacts, courtesy of Serreze et al. 2021. Conditions leading to ROS events and some of the impacts associated with them.

ROS events may be more common in the middle latitudes, based on geographic position relative to sources of maritime moisture or due to the number of rain days a

location may experience (Cohen et al. 2014; Leavesley 1997; McCabe, Clark, and Hay 2007). Some studies demonstrate how especially prevalent they are in the Pacific Northwest in the United States, based on the types of weather conditions required for them (McCabe, Clark, and Hay 2007). Impacts from flooding are well-known – with the combination of heavy rainfall and melting of the underlying snowpack (McCabe, Clark, and Hay 2007). Kattelmann (1997), in *Destructive Water: Water Caused Natural Disasters, their Abatement and Control*, describes ROS events in the Sierra Nevada:

> "The high potential for flood generation from rain-on-snow events is related to their large contributing area, intensity and duration of rainfall, opportunity for snowmelt contributions, and, sometimes, the timing of release of water from the snowpack. The primary factor is simply the increase in contributing area with rainfall-runoff production from the higher elevation portions of river basins that typically receive snow during other winter storms," (Leavesley 1997).

Other impacts from ROS events include disruptions to the transportation sector – including aviation operations – and "slush," or wet-snow, avalanche hazards (Hansen et al. 2014; Putkonen and Roe 2003). Officials may close roads and airports due to ice formation from these events; this then impacts access for isolated Arctic towns (Hansen et al. 2014). Hansen et al. (2014) also explain how wet-snow avalanches threaten infrastructure. For one particular event, Longyearbyen (in Svalbard) witnessed a slush avalanche destroying a pedestrian bridge, and major roads that led in and out of the community had to be closed for several days due, in part, to these avalanches (Hansen et al. 2014). They also add that these Arctic locations are susceptible to future wet-snow

avalanches, since infrastructure was not originally built with these in mind, and many buildings may lie in the resulting debris flow path.

Among indigenous Arctic communities, ROS events present another serious concern. Following the event, the ice layers that grow on, or within, the snowpack act as a barrier to ungulate animal populations foraging for food (Figure 1.6); this leads to massive starvation and die-off episodes among these animals, which may include caribou, reindeer, and musk oxen (Forbes et al. 2016; Rennert et al. 2009; Serreze et al. 2021). Ice formation may also trigger these species to seek other sources of food further away from their regular environments, exacerbating the conditions leading to starvation (Serreze et al. 2021). One example of this is through the growth of various fungi types and mold due to the warming of the underlying layers of the snowpack; this pressures animals to pursue other locations for food (Putkonen and Roe 2003). Some major examples of these large die-off events include a ROS event that occurred in Banks Island, Canada, and led to the killing of an estimated 20,000 musk oxen, an event in Svalbard in January of 2012 – which produced one of the largest numbers of reindeer carcasses found in the summer of 2012 – and an event in the Yamal Peninsula in northern Russia during the autumn of 2013 that starved approximately 61,000 reindeer (out of a total of 275,000) (Forbes et al. 2016; Hansen et al. 2014; Rennert et al. 2009; Serreze, Crawford, and Barrett 2015).

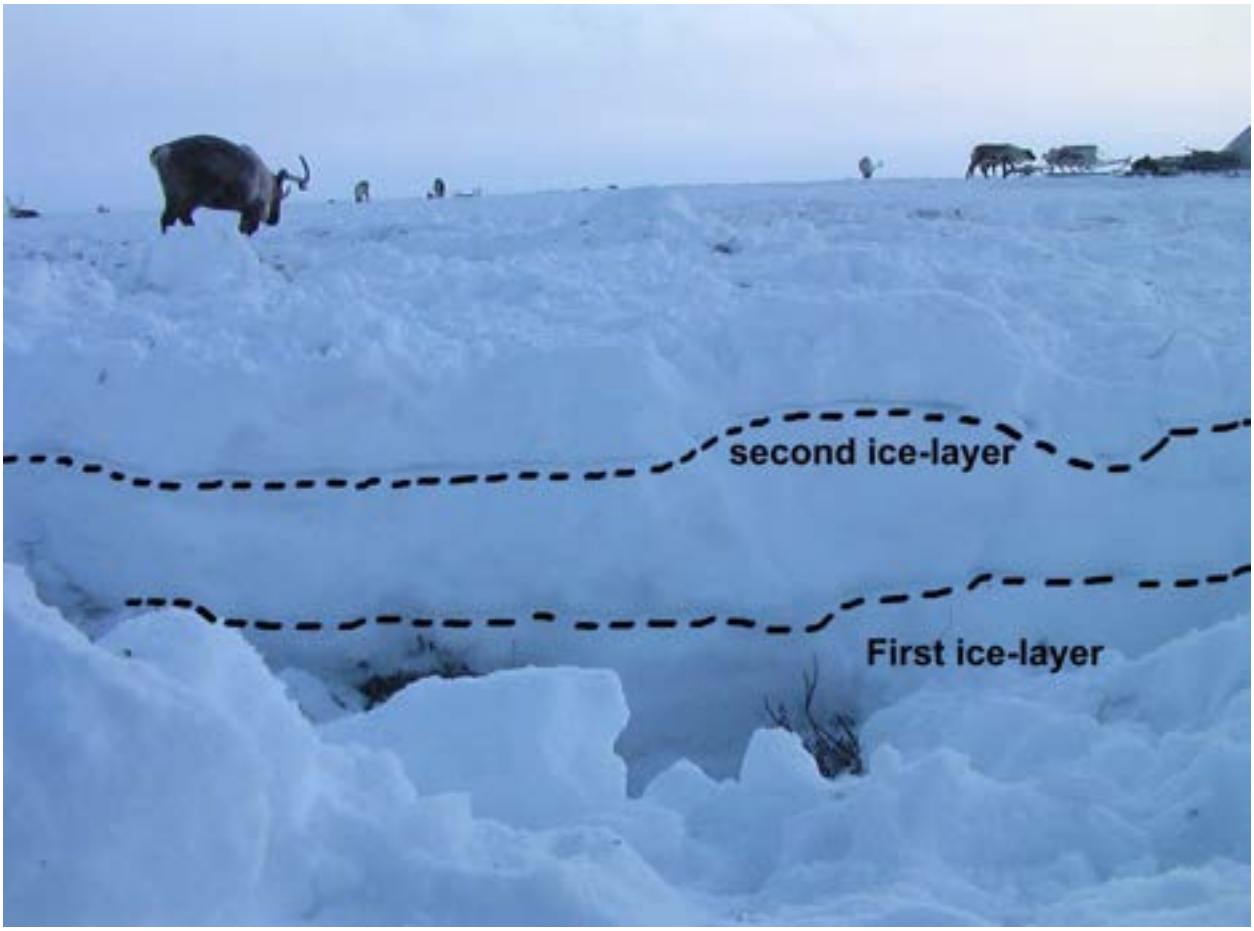

Figure 1.6: ROS Ice Layers Among Reindeer. Image courtesy of the National Snow and Ice Data Center (image credit to Florian Stammler). This image shows multiple ice layers formed as a result of two ROS events in November 2007 on the Yamal Peninsula in Siberia, Russia.

In Alaska, ROS events are most likely to occur from October through April – with some studies narrowing it to November through March – when conditions are favorable and a snowpack is present (Bieniek et al. 2018; Crawford et al. 2020; Pan et al. 2018). Studies for other regions of North America and Eurasia, where major ROS occurrences were examined, have noted this time range as well, with the season beginning in the fall and moving into the spring (Cohen, Ye, and Jones 2015). Cohen, Ye, and Jones (2015) add that ROS events occurring in the fall and winter generate more alterations in the underlying snowpack's thermal properties and affects the soil characteristics before the actual snowmelt season in the later spring months. Conversely, ROS events occurring

in spring may intensify the snowmelt process, adding to runoff and flooding concerns (Cohen, Ye, and Jones 2015). Working in tandem with the overall precipitation event, increased warm air advection with these systems causes additional melting of the surface snow layer through amplified mixing and turbulent fluxes (Semmens et al. 2013). Arctic ROS events may occur more frequently along coastal areas or in more maritime climates, such as those found across southern Alaska (south of the higher terrain) or in locations based within the North Atlantic cyclone track, such as Svalbard (Crawford et al. 2020).

Researchers have identified some synoptic scale meteorological components that contribute to ROS formation. For the ROS event over Banks Island, Canada (2003), it was determined that a strong upper-level anticyclonic ridge initially developed over the region (Rennert et al. 2009). These authors noted that this anticyclone produced strong, southwesterly flow that brought in warmer, moister air into the area. Lift (upward motion), triggered by an approaching shortwave trough, initiated precipitation across the region. The precipitation first began as snow then transitioned to rain due to the higher air temperatures (Rennert et al. 2009).

Some ROS studies also mentioned the importance of strong atmospheric blocking leading to the initiation of some ROS events and atmospheric river (AR) setups. When looking at the synoptic climatology of ROS events in Alaska, Crawford et al. (2020) discovered a connection between blocking patterns, especially considering the strong ridge of high-pressure component, and the deep pressure gradient that builds between it and an approaching extratropical storm system. This instigates further advection of higher air temperatures and higher precipitable water anomalies, leading to

the ROS event. Other studies noted the correlation between major ROS events and ARs and a higher percentage of ROS events associated with landfalling ARs along the US west coast (Guan et al. 2016; Trubilowicz and Moore 2017). Despite these studies, scientists acknowledged that additional research is needed to understand the weather patterns influencing ROS events and if large synoptic-scale features - such as ARs or blocking setups – impact the formation of ROS events across the Arctic (Bieniek et al. 2018; Rennert et al. 2009).

1.4: Motivation for Study, Research Questions, and Overview of Case Studies

As the Arctic continues to warm, scientists must persist in their examinations of how this will alter atmospheric circulation patterns, including extreme weather events. ROS events pose many hazards, especially for indigenous communities. Investigations of past ROS events yielded an improved understanding of some of the associated meteorology, and a growing body of published research has made the case that ROS events – and their resulting impacts – may constitute “extreme” events. As mentioned, researchers acknowledge that more data needs to be examined to comprehend the atmospheric features driving these events. This research should include examining the synoptic level (e.g., planetary waves, troughs, and ridges) and at smaller spatial scales that include possible localized weather effects. This prompts two major research questions guiding the present research:

1. *What are the primary meteorological conditions across varying spatial scales necessary for major ROS events to occur in the Arctic?*

2. *Can it be confirmed that synoptic blocking patterns are an influential setup in ROS formation, which may create atmospheric gradients that trigger strong southerly flow and allow atmospheric rivers to form?*

Determining the atmospheric drivers of major Arctic ROS events presents significant implications for climate change research. As noted, a rapidly warming Arctic raises the possibility of both extreme precipitation episodes through higher moisture amounts provided for storm systems (Clausius-Clapeyron relationship), and a shift from snowfall- to rainfall-dominated climates (McCrystall et al. 2021). From past research, several have consistently identified these two features – anomalously high temperatures and atmospheric moisture – for major ROS cases. These points emphasize the importance of determining the exact meteorological variables linked to hazardous ROS occurrence.

To this end, this research analyzes five ROS case studies, making use of ERA5 atmospheric reanalysis datasets from the European Centre for Medium-Range Weather Forecasts (ECMWF). Each of these ROS events contains documented eyewitness reports of rain falling on snow, surface observations of ROS conditions, or highly consequential ROS-based impacts (such as starvation events of hooved animals):

- The first case was the event in October 2003 that occurred on Banks Island, Canada that killed approximately 20,000 musk oxen (Rennert et al. 2009).
- The second ROS case occurred over Svalbard, Norway, in January 2012. This event also led to a high mortality event among native reindeer, and it coincided with the highest daily precipitation amount recorded at Ny Ålesund for the 1979-2014 period

(Serreze, Crawford, and Barrett 2015). That study also suggested an AR influence for this ROS event.

- The third ROS event affected the Yamal Peninsula in northern Russia in early November 2013. This was another high mortality event among reindeer and caribou that severely impacted native herders in the region (Forbes et al. 2016).
- The fourth case was a ROS event over western Greenland in April 2016. This case represents a unique ROS instance that led to major slush avalanches observed near Godthaab, Greenland, that coincided with unusually high temperatures and a significant precipitation event (Abermann et al. 2019).
- The fifth and final ROS event examined occurred in Iqaluit, Canada, in January 2021. An unusual stretch of above average air temperatures preceded this event for most of Canada, including the Iqaluit area. A team member of the Arctic Rain on Snow Study (AROSS) from the National Snow and Ice Data Center (NSIDC) personally witnessed the event, and local media organizations documented the warmer weather leading up to the event (CBC, News 2021; Nunatsiaq, News 2021). AROSS is the NSF-funded study under Navigating the New Arctic that has funded this thesis.

Chapter 2: Data and Methodology

2.1: Selected ROS Case Studies Chosen for this Research

It is important to recognize that the ROS events selected for this study (Figure 2.1) are confirmed events, whether through observations, eyewitness accounts, or recorded major impacts. These five case studies are associated with one (or all) of these forms of "ground truth." Some of the events have even been studied previously, but these studies may only describe the extent of the impacts connected to these events, not necessarily going in-depth on the meteorology. For example, previous

Figure 2.1: Case Study Map. Map of select ROS case studies with this research.

research has addressed impacts of the October 2003 case from Banks Island, Canada (Grenfell and Putkonen 2008; Rennert et al. 2009), where both write of the large mortality of musk oxen in the affected region, but their research methodology ranges from remote sensing to the synoptic meteorology of the event. Grenfell and Putkonen

(2008) describe using remote sensing techniques – specifically, passive microwave satellite sensors that detect changes in brightness temperature – to identify ROS conditions. Rennert et al. (2009) build on Grenfell and Putkonen's work to show the synoptic meteorology setup during the event using ERA-40 reanalysis datasets, an older atmospheric reanalysis from the European Centre for Medium-Range Weather Forecasting or ECMWF.

The case studies from Svalbard in 2012 and the Yamal Peninsula, Russia, event from 2013 were also studied previously, both covering some meteorology topics and impacts associated with the events. The Svalbard 2012 event led to a high mortality of the local reindeer population (Serreze, Crawford, and Barrett 2015). It also coincided with the highest daily precipitation amount recorded for the 1979-2014 period, and the event is suspected of being influenced by an atmospheric river (AR) (Serreze, Crawford, and Barrett 2015). The Yamal Peninsula event in 2013 generated a severe starvation episode among reindeer in the region; local herders also observed the resulting ice produced during this ROS event that led to these die-off conditions (Forbes et al. 2016). Forbes et al. (2016) also noted precipitation anomalies with this event using ERA-Interim reanalysis (another earlier atmospheric reanalysis dataset from the ECMWF) and included combined remote sensing data from the Atmospheric InfraRed Sounder and Advanced Scatterometer data to detect ROS conditions and support herders' observations.

Concerning the final two case studies, scientists noted significant combined warming and precipitation coinciding with increased wet-snow avalanche activity in the early to middle part of April leading to the western Greenland 2016 event (Abermann et

al. 2019). This study from Abermann et al. (2019) also used remote sensing to detect changes in landscapes near Nuuk, Greenland, to examine the impacts associated with the wet-snow avalanches. The ROS event that occurred in Iqaluit, Canada, in January of 2021 was very recent, and there are no previous studies (that this author is aware of) examining associated meteorological conditions. However, this event was confirmed through an eyewitness report from a team member affiliated with the NSF-funded Arctic Rain-on-Snow Study (AROSS). The AROSS team is based within the National Snow and Ice Data Center (NSIDC) under the Cooperative Institute for Research in Environmental Studies (CIRES) at the University of Colorado in Boulder. The AROSS team collaborates with several other organizations whose goal is researching the Arctic and understanding the changes occurring in this region.

2.2: Atmospheric Reanalysis

When attempting to understand the atmospheric structure at all levels, scientists place heavy reliance on atmospheric reanalysis datasets. These datasets “paint a picture” of what the atmosphere looked like at a specific time. Atmospheric reanalysis is produced from a combination of numerical weather prediction models and assimilated observational data (Keeley 2013). The observation types encompass station data, but also incorporate sounding and satellite data, buoy records, and ship and aircraft reports (Dee et al. 2016). Reanalysis represents a valuable tool in studying any changes to Earth’s atmosphere and climate when observational data may be lacking.

Researchers can monitor changes to the atmosphere resulting from fluctuations in other Earth processes or changes in dynamics (e.g., reduction in sea ice, changes in mass balance of glaciers and ice sheets, and the consequences of Arctic amplification),

and this is especially useful when dealing with a sparse surface observation network, which is the case across much of the Arctic (Lindsay et al. 2014). According to Hersbach et al. (2020):

> "Reanalyses have found a wide application in atmospheric sciences, not least in operational weather centres where, for example, reanalyses are used to assess the impact of observing system changes, to gauge progress in modeling and assimilation capabilities, and to obtain state-of-the-art climatologies to evaluate forecast-error anomalies," (Hersbach et al. 2020).

Unfortunately, no one selection from the various repositories of reanalysis data contains perfect measurements, with each presenting different biases for diverse meteorological parameters (Lindsay et al. 2014).

Among the numerous reanalysis datasets available, the ERA5 dataset (produced by the ECMWF) is the best option for the present study because it is the newest dataset available (becoming operational in 2016). Recent studies also show that the ERA5 dataset presents overall smaller biases and errors when compared to both the earlier ERA-Interim (also from ECMWF) and other reanalysis datasets (Graham, Hudson, and Maturilli 2019). It performs well on certain meteorological variables (temperature, specific humidity, and wind speed for this particular study) when compared to observational data (Graham, Hudson, and Maturilli 2019). Improvements in spatial and temporal resolutions and advancements in model physics and data assimilation make the ERA5 dataset more useful in analyzing weather systems (Hersbach et al. 2020).

A number of studies employed various atmospheric reanalysis datasets when examining previous ROS events ranging from Canada and the Svalbard Archipelago to

the Yamal Peninsula of Russia (Forbes et al. 2016; Rennert et al. 2009; Serreze, Crawford, and Barrett 2015; Serreze et al. 2021). Cohen, Ye, and Jones (2015) also utilized atmospheric reanalysis to examine potential trends in Arctic ROS events. Because it is a well-known tool among atmospheric scientists and used extensively in ROS research, atmospheric reanalysis is the primary dataset utilized with this case study research.

The ERA5 data were accessed via the Copernicus Climate Data Store API [Application Program Interface] from the 1979 to present dataset. ERA5 reanalysis data are available in hourly format, but only the 00Z (UTC) and 12Z files were selected for the present effort. These selected times coincided with upper air launch times (radiosondes), and twelve hour increments still provides enough of a picture to examine the synoptic makeup of these ROS events. The API tool allowed the different meteorological variables of interest to download to NETCDF (or Network Common Data Form) files on a local machine. The NETCDF file types utilized with this data store scientific data (atmospheric information in this instance) of multiple dimensions in binary format that can easily be accessed via various computer programming languages (“What Is NetCDF? | National Snow and Ice Data Center” n.d.). Subsequently, python code written to handle these files and display visualizations provided this study with the images containing plotted meteorological data and may be found in the “Results” chapter.

2.3: Explanation of Weather Procedures Utilizing ERA5 Reanalysis Data

To gain a perspective on how the atmosphere behaved during each of the ROS events, this research used seven different procedures applying ERA5 data, which

represents conditions at chosen levels of the atmosphere. The range of levels included representation from the upper levels to the middle levels (mid-levels) and down to the lower levels, which included the surface in some instances. “Procedures,” the language utilized in this research, means an analysis chart including multiple weather variables recorded for a particular level and plotted together on one chart. The upper-level procedures contained various data for the 250-mb level, typically classified as the jet stream level, and for the 500-mb level. The mid-level procedures comprised of atmospheric data at the 700-mb and the 850-mb levels. The low-level procedure included 925-mb level data. Two procedures utilized mean sea level pressure (MSLP) fields, one with precipitable water overlaid and integrated water vapor transport plotted on the other.

The two upper-level procedures (the 250-mb and 500-mb analysis) were designed to show the progression of planetary waves and the wind behavior aloft. The 250-mb procedure represents the jet stream level and shows the trough and ridge pattern through geopotential height contours, which are the features that influence overall global weather (see Chapter 1). The geopotential variable was downloaded and then converted to geopotential height by dividing by the gravitational constant; this task was also completed for height contours found at all levels. The 250-mb procedure also represents one of the visuals where one can easily see blocks or blocking patterns. The 500-mb procedure includes the height contours for that level and shows the upper-level winds. The shaded colors in the visualization for the 500-mb winds represent the isotachs, or lines of constant wind speed.

For the mid-levels, the 700-mb procedure utilized geopotential heights, relative humidity, and negative Omega (rising motion) for this level in the atmosphere. Omega is typically presented as a complex formula and a second component of quasi-geostrophic theory, but put simply, it represents the vertical motion within the atmosphere. The units for Omega were converted to millibars per second, which closely equates to centimeters per second. The sign is in relation to the earth's surface, so a negative sign means the movement is away (rising away) from the surface. Plotting areas of rising motion overlaid with relative humidity provides a general idea of where one might find precipitation occurring. Relative humidity represents the percentage relationship between the vapor pressure and the saturation vapor pressure relative to air temperature (Petty 2008). According to Petty:

> "Note, however, that the relative humidity is not a very useful measure of the absolute moisture content of the air because as the temperature changes, so does e_s [saturation vapor pressure] and therefore the RH [relative humidity], even if the actual vapor pressure e (or mixing ratio or vapor density) remains constant," (Petty 2008).

One hundred percent relative humidity does not mean that it is precipitating but that the air is saturated, which supplements the reasoning for also plotting negative Omega at this level. Dynamics and lift are required, in addition to moisture, for initiation of precipitation.

The 850-mb procedure utilized 850-mb heights, mixing ratio values, and 850-mb air temperatures in °C but only plotted for values above freezing. The NetCDF with

ERA5 reanalysis yields the specific humidity; the value of the mixing ratio can then be calculated from this value using the following equation:

$$w = \frac{q}{1 - q}$$

The specific humidity (q) is closely related to the mixing ratio in that it yields the mass of water vapor per unit mass of *moist* air (Petty 2008). However, the mixing ratio (w) returns the ratio of the mass of water vapor per unit mass of dry air; usually these two values are almost similar, since the mass of water vapor is usually no greater than one or two percent of the total mass (Petty 2008).

The specific humidity and mixing ratio values compare differently than the relative humidity value from the 700-mb procedure. Recall that relative humidity is the actual ratio between the vapor pressure and saturation vapor pressure and is often expressed as a percentage; therefore, it is also a function of air temperature. However, the mixing ratio value, calculated from specific humidity, determines the amount of water vapor. Additionally, Lackmann (2011) also uses an 850-mb procedure that includes winds at that level and mixing ratio values to show features associated with ARs, including cyclone-induced low-level jets and increased moisture flowing along narrow corridors.

The low-level procedure with this research included variables plotted for the 925-mb level. Because pressure level heights differ at varying locations based on elevation, the 925-mb level generally extends a few hundred meters above the surface. The meteorological variables included with this procedure were the heights, winds, temperatures, and relative humidity greater than 85 percent. This procedure was designed to continue showing trends in warm or cold air advection or the transport of

moisture, if both processes were occurring in the atmosphere. Both variables were instrumental in seeing the change in air masses occurring during these ROS events or where the warm, moist air may have originated from.

The other two procedures provided an idea of how the MSLP contours appeared, in addition to two other weather parameters. One procedure took MSLP and overlaid precipitable water (PWAT). PWAT yields the amount of water precipitated out at the surface if the entire column of air in the atmosphere had all vapor, liquid, and solid water condensed out (Stull 2000). In reality, various atmospheric interactions – like moisture advection and entrainment processes that replenish moisture lost to precipitation – may cause total precipitation accumulation to be greater at the surface after a storm passes, but PWAT gives a general idea of how much water is in the atmosphere (Stull 2000).

The other procedure plotted MSLP with integrated water vapor transport (IVT), displaying both vectors and kilograms per meters, per second, in the filled contours. The ERA5 data allows users to download vectors representing the u and v-components of the vertical integral water vapor flux, with the u-component as the eastward component and the v-component as the northward component. IVT is traditionally calculated by taking the integral of specific humidity multiplied by the total vector wind and then multiplying the integral equation by one over the gravitational constant. However, since the u- and v-components of the vertically integrated water vapor fluxes were downloaded, the IVT used in this procedure can be calculated using vector math:

$$IVT = \sqrt{{u_{vapor}}^2 + {v_{vapor}}^2}$$

(u_{vapor} and v_{vapor} represent the vertically integrated water vapor fluxes)

High IVT values represent a key characteristic in AR detection and have been utilized in research investigating the connection between ARs and ROS events (Guan and Waliser 2015; Guan et al. 2016).

2.4: Station Observations, Upper Air Soundings, and Eyewitness Reports

Observational data and eyewitness accounts assist in verifying the atmospheric reanalysis data, which is built from observations and weather models. By using both observations and upper air soundings with this study, one can supplement the atmospheric reanalysis data, gain insights as to the spatial scale of some of these environments, and possibly discern other mesoscale or even local-scale weather features impacting these ROS events.

Surface observations across the Arctic are somewhat sparse and sometimes may be unreliable. Because weather conditions may be quite harsh in Arctic regions, sometimes sensors may stop operating. This may lead to periods of no recorded data or incorrect weather conditions observed for a location. Many of these observation sites may be found in regions with complex terrain, so technicians may require additional time to make these stations operational again. Another concern with station data is that these point observations may not be representative of all conditions resulting from a strong weather system passing through the area. Many stations are collocated near airports, as their predominant purpose is for use by pilots or aviation stakeholders. However, other locations at different elevations or impacted by other maritime features – such as the ocean – may experience different conditions, especially during a potent winter storm with varying precipitation types.

There are also limitations with upper air sounding data. This data comes from weather balloons (radiosondes) launched at established sites around the world. As the balloon ascends through the atmosphere, the attached radiosonde records pressure, temperature, dewpoint temperature, and wind speed and direction data. Upper air soundings produce valuable data for input into reanalyses and operational numerical weather prediction systems and provide meteorologists with insight on how the atmospheric column appears from the surface to the upper levels. One can also glean a lot of information as a forecaster about a weather environment, whether considering precipitation types during a winter storm or understanding how favorable conditions may be for producing severe weather. Unfortunately, these weather balloons are generally launched only two times a day: one at 00Z and one at 12Z. Some sites may only launch once per day. A lot can happen in the span of 12 hours between balloon launches. Like station data, soundings represent a point measurement and may not capture all conditions associated with an extreme weather event.

In some instances, eyewitness reports are available. Despite the importance of station data, sometimes it is lacking for more rural locations or regions with less population, and they may not include all precipitation types that occurred during an event. Eyewitness reports represent another method for meteorologists to determine weather conditions. Eyewitness reports are used extensively by Weather Forecast Offices (WFOs) in the National Weather Service (NWS). In severe weather instances, eyewitness reports may be utilized in warning verification purposes. This research employs them when stations failed to report ROS conditions or were not available.

Upper air and station data were both obtained from various website databases through python module functions designed to download the data. Python code was provided through MetPy for downloading sounding (upper air) data from the University of Wyoming sounding archive and to build the skew-t visualizations of the upper air data. MetPy is a program under Unidata, a community program within the University Corporation for Atmospheric Research (UCAR). Observational station data were provided from the Iowa State University, Iowa Environmental Mesonet, Automated Surface Observation Station network page (https://mesonet.agron.iastate.edu/ASOS/). Python coding was then deployed to download the chosen data from the respective sites and time periods of interest to comma separated values files or CSVs.

All observational station data and upper air sounding data are presented using visualization techniques yielded from python code. The skew-t images exemplify a data visualization technique for upper air data gathered from weather balloon launches. Atmospheric scientists give skew-ts this moniker because the air temperature lines, which essentially correspond to the x-axis, are skewed. This is because pressure is plotted logarithmically with height, and this height-pressure parameter represents the y-axis. Skew-t plots usually display the air temperature and dewpoint temperature as red and green lines, respectively, plotted with height that link to a corresponding pressure level. Wind direction and speed are also plotted and displayed as wind barbs, typically on the right-hand side of the chart. In the code for these skew-t plots, a hodograph has also been provided in the upper right-hand corner. This plots the wind speed and direction using polar coordinates, and the wind vectors are added with these cases to make the changes in wind behavior with height easier to understand.

Station observations, when available, were coded to show both the changing air temperature and dewpoint temperature at the surface. The code was also written to display the present weather codes automatically taken for the observation at each site. Weather codes range from liquid to solid parameters, like rain or snow, to more mixed categories, such as periods of rain and snow or freezing rain (when the appropriate sensor is available). This link provides a list of corresponding abbreviations to their respective weather codes: https://www.weather.gov/media/wrh/mesowest/metar_decode_key.pdf. For some major airports collocated with these stations, there is a dedicated weather observer that may augment the station observation with physically observed conditions. As will be seen, visualizations from the station data capture similar conditions with these ROS events as what has been shown with Figure 1.5, presented in Section 1.4 from Serreze et al. (2021).

In summary, atmospheric reanalysis represents the main data source for this research in identifying the meteorological setup, and the observational data (including soundings and eyewitness reports) supplement reanalysis data. These additional datasets are added to confirm and provide more information on the meteorology surrounding the ROS events. Specifically, when available, observational data prove valuable in verifying the reanalysis data and confirming the reported weather conditions at the surface during these five ROS events. The eyewitness accounts add another perspective on all conditions during these ROS events that observational data missed and confirm that ROS conditions did occur with associated impacts.

2.5: HYSPLIT Modeling for Examining Atmospheric River Influences

Atmospheric reanalysis remains the method of choice in also analyzing the contribution of ARs, similar to the approach used in identifying other meteorological features contributing to Arctic ROS events. However, just like using the observations to supplement the reanalysis, it is valuable to utilize HYSPLIT modeling results to determine the amount of impact from ARs in all cases and if ARs contributed directly or indirectly to the ROS events. A number of uses exist with HYSPLIT modeling, from tracking pollution to understanding the path of release pertaining to hazardous chemicals (Stein et al. 2015). One of its main advantages is the ability to perform backwards trajectories of air parcels to understand where an air mass may have originated (Stein et al. 2015). According to Stein et al. (2015):

> "The model calculation is a hybrid between the Lagrangian approach, using a moving frame of reference for the advection and diffusion calculations as the trajectories of air parcels move from their initial location, and the Eulerian methodology, which uses a fixed three-dimensional grid as a frame of reference to compute pollutant air concentrations (the model name, no longer meant as an acronym, originally reflected this hybrid approach."

Using the HYSPLIT model to determine the origin of air masses assists in identifying if a moisture source for an AR-like object originated from the subtropics or tropics, further adding to the evidence of AR-influenced impacts.

HYSPLIT models were run using the user adapted READY website, which allows personalization of various model parameters and a wide variety of atmospheric datasets to choose from available with the model (Rolph, Stein, and Stunder 2017):

> “READY also has several archived analysis meteorological data sets available including the HRRR, NAM, NAM Data Assimilation System (NDAS), Global Data Assimilation System (GDAS), and the NCEP [National Centers for Environmental Prediction] / National Centers for Atmospheric Research (NCAR) Reanalysis data,” (Rolph, Stein, Stunder 2017).

For the present research, the archived global datasets with the highest resolution were chosen that were available for the time period applicable to each case. Backward trajectories were run for a 96-hour period (four days) to determine the air mass of origin prior to the day of interest. Heights of 750, 1500, and 2500 meters were also selected with each model, which represents the rough equivalent level of the 925-mb, 850-mb, and 700-mb pressure levels, respectively. The intent is to see how each of these levels evolved over the four-day progression of the model. This provides an idea of whether the air masses originated within the subtropics or tropics, another indication of the presence of an AR, or if the air masses originated elsewhere.

Chapter 3: Results

This chapter explores both the key meteorological similarities and differences among the five rain-on-snow (ROS) event case studies. The chapter is organized by two primary sections and successive subsections. The first section provides an overview of the primary meteorological drivers that were found to influence all events. The second section provides a more in-depth description of each event and identifies the diverging characteristics between it and the other ROS events. This layout supports the information needed to answer the initial research questions posed in Chapter 1: 1) the primary meteorological conditions across varying spatial scales necessary for major Arctic ROS events and 2) confirming if blocking patterns played a role in their formation and the development of other weather phenomena that affect the impacts experienced with these ROS events.

3.1: Key Meteorological Phenomena Influencing All ROS Cases

3.1.1: Pronounced Blocks or Blocking Patterns

Based on the atmospheric reanalysis for all ROS cases within this research, it was found that blocks and blocking patterns play important roles in their formation. Not only were these features crucial for initiating ROS conditions over a particular region, but the synoptic setup associated with these patterns influenced the severity of ROS conditions by generating substantial zones of warmer air and moisture transport. These zones in all cases had directly south-to-north moving air masses, which also affected the amount of warm, moist air moving into an Arctic region, where these conditions are not expected during the winter months. Obviously, the warming conditions necessary for liquid precipitation during these ROS events was transported through augmented south-

to-north meridional flow. This strong meridional flow occurred when the natural west-to-east moving flow representative of the normal approximately geostrophic movement aloft became disrupted due to the blocking pattern (Woollings et al. 2018).

All the blocking patterns in these cases began developing a few days prior to the day (or days) of witnessed ROS conditions for a location and required a few days after the event to retrograde. The duration for this meteorological setup was consistent with previous research on blocking patterns. The ERA5 reanalysis output confirmed that the synoptic pattern leading to the blocking and consequent ROS conditions was one of long, stationary patterns that persisted for more than a few days (Rex 1950; Woollings et al. 2018). In some cases, the identifying contour shapes may be different (i.e., a Rex Block versus an Omega Block), which is discussed further in each subsection detailing differences among the ROS cases. However, blocks represented the primary causal mechanism driving these ROS events, as can be seen in the atmospheric reanalysis data.

Figures 3.1.1-3.1.5 reveal how these blocks played an active part in the ROS events, as shown in the 250-mb geopotential height contours, and as noted, they are present in each of the five cases. The redder colors indicate higher heights in the upper levels, synonymous with warmer air masses, and the bluer colors correspond to lower heights and cooler air masses. The position of the anticyclonic component of the block (the ridge of high pressure) – represented by the red contours and usually situated between the blue contours of lower heights – remained the major factor in setting up ROS occurrence for a location. This was also identified in previous ROS research (Rennert et al. 2009; Crawford et al. 2020).

The ridge of high-pressure component of the block – or the anticyclone at the synoptic level – represented the main feature driving the movement of higher temperatures, associated with warmer air masses, and typically higher moisture amounts over an area. As noted in a previous ROS study for the Banks Island Canada event in 2003, strong, southwesterly flow associated with a ridge (identified in the 500-mb height analysis) contributed to the significant warm air advection preceding the onset of precipitation (Rennert et al. 2009). This provided the increased air temperatures necessary to cause liquid precipitation, as opposed to snow. Depending on the location of the ROS event in relation to the overall synoptic setup, this formation may also lead to onshore flow, which represents an air mass moving over water towards land. This also helps in moistening and warming much of the atmosphere and the boundary layer.

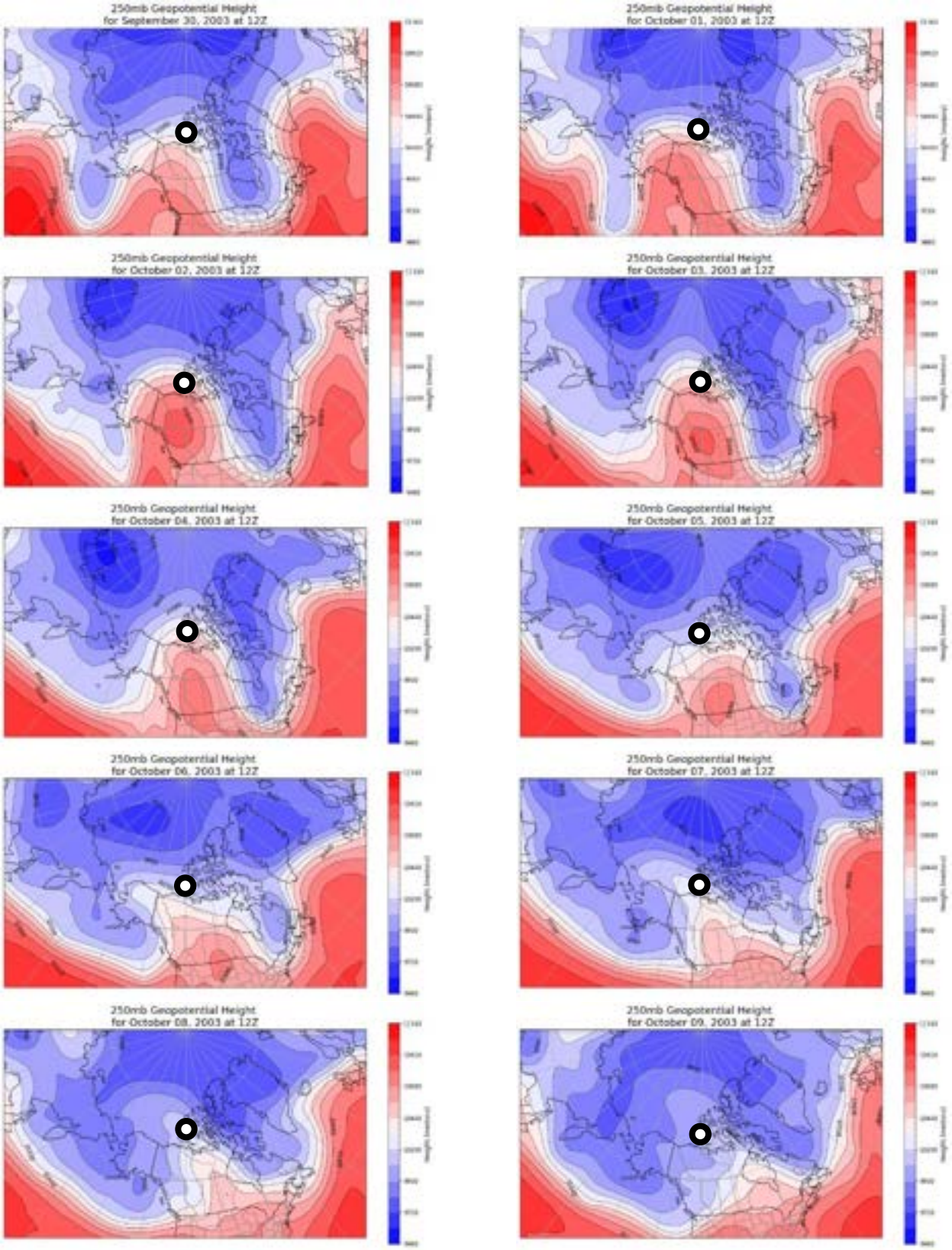

Figure 3.1.1: 2003 ROS Event Block. 250-mb geopotential height contours from September 30 to October 9, 2003, during the Banks Island, Canada, ROS event. The white dot represents ROS location.

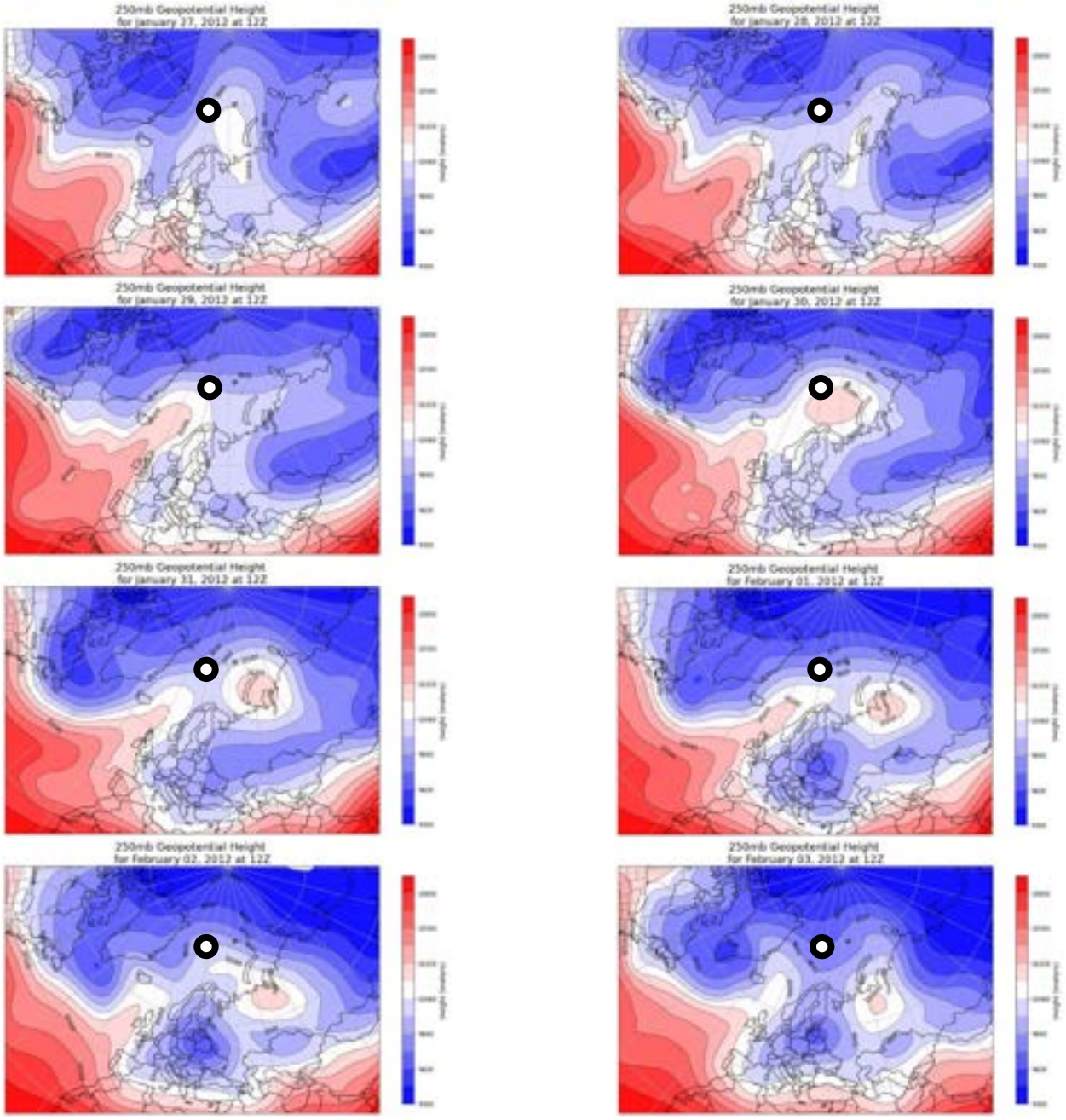

Figure 3.1.2: 2012 ROS Event Block. 250-mb geopotential height contours from January 27 to February 3, 2012, during the Svalbard, Norway, ROS event. The white dot represents the ROS location.

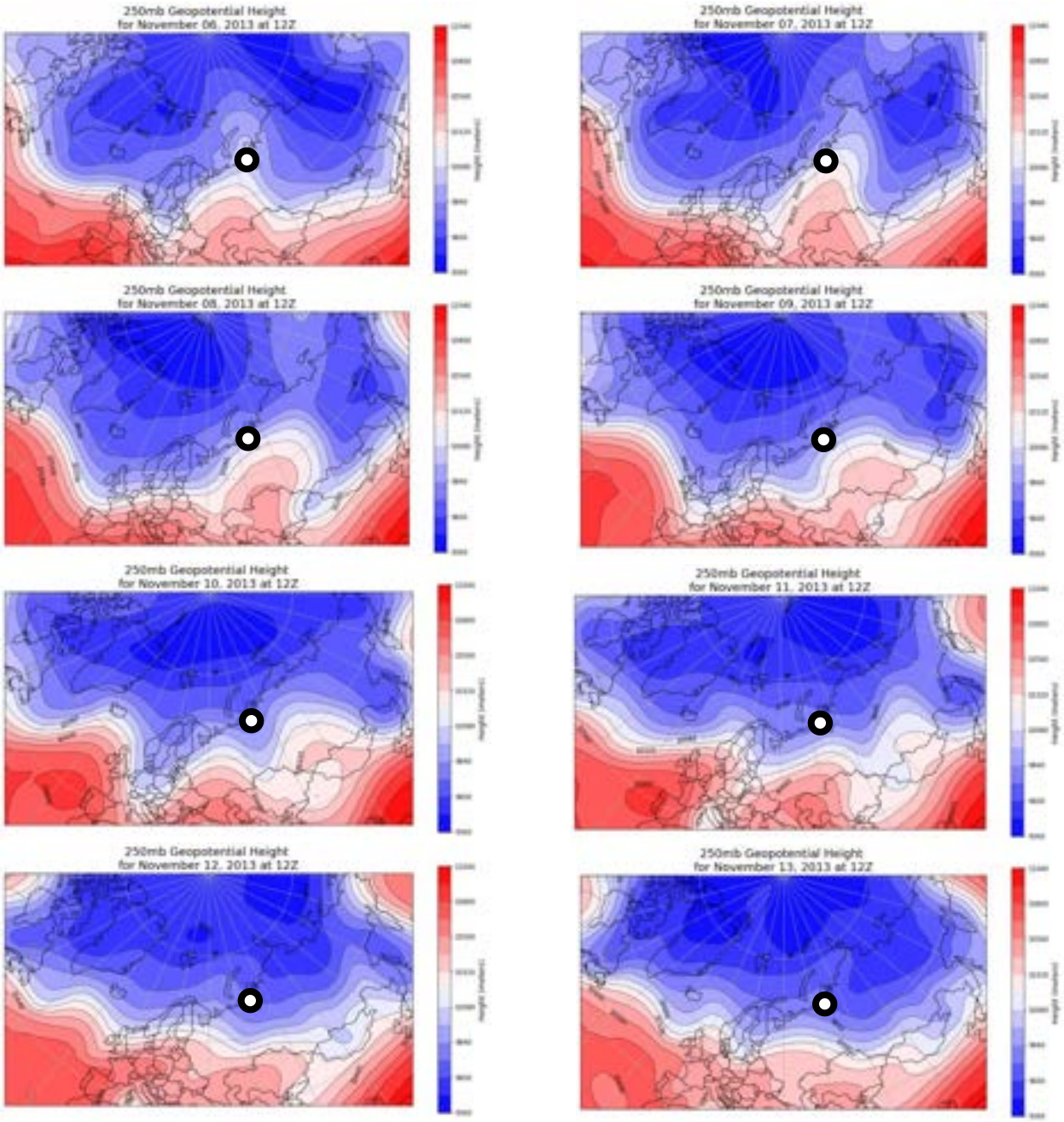

Figure 3.1.3: 2013 ROS Event Block. 250-mb geopotential height contours from November 6 to November 13, 2013, during the Yamal Peninsula, Russia, ROS event. The white dot represents the ROS location.

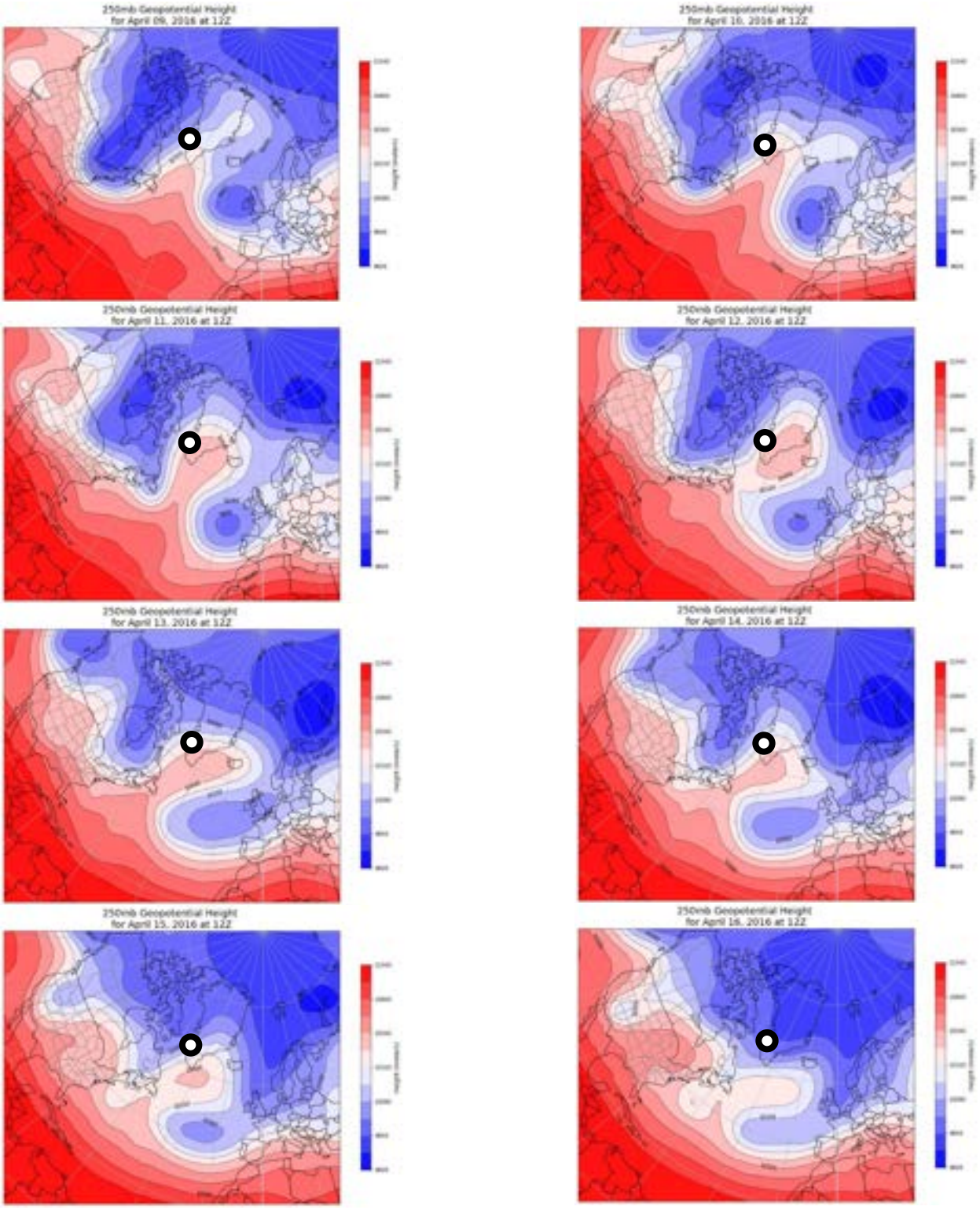

Figure 3.1.4: 2016 ROS Event Block. 250-mb geopotential height contours from April 9 to April 16, 2016, during the Western Greenland ROS event. The white dot represents the ROS location.

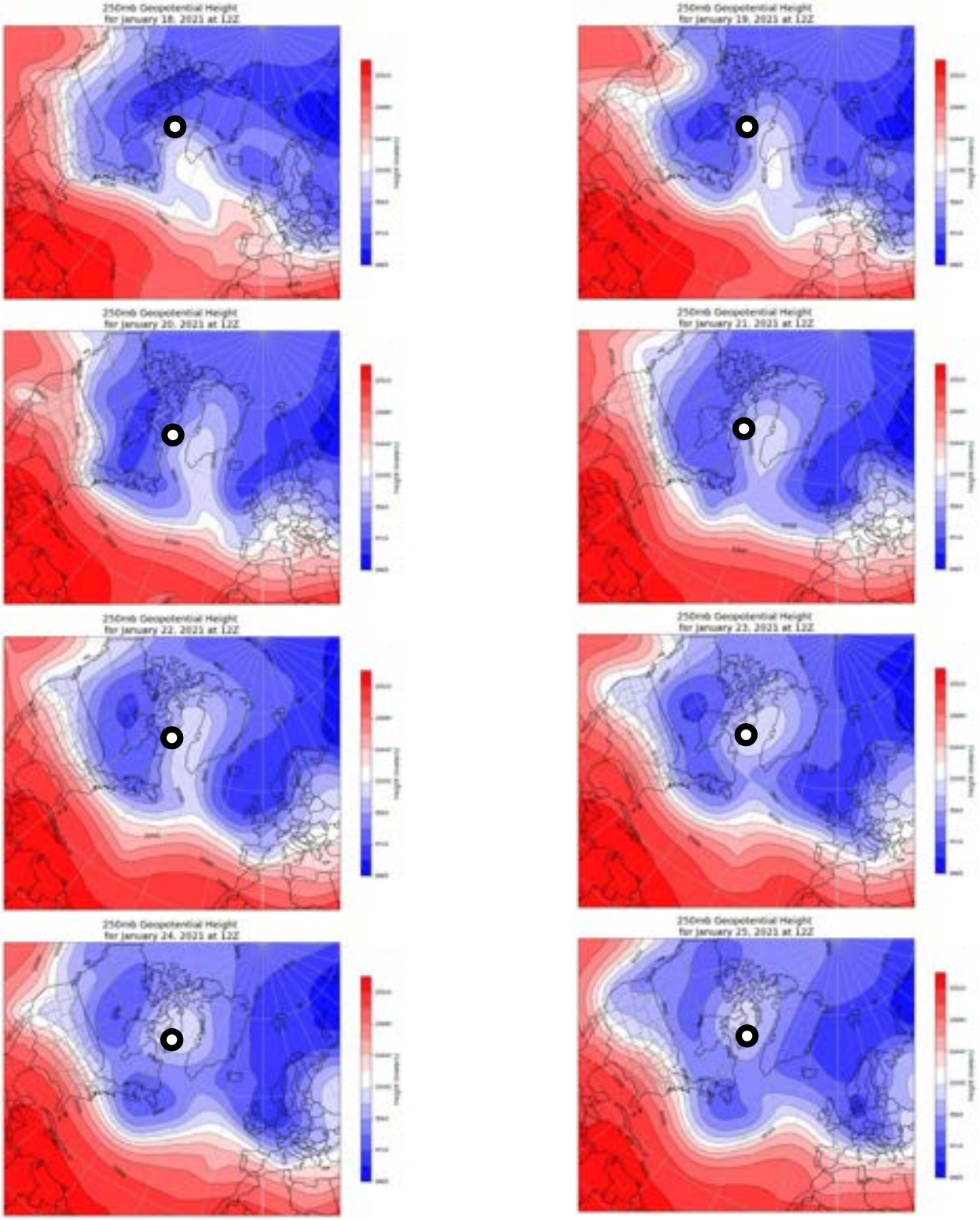

Figure 3.1.5: 2021 ROS Event Block. 250-mb geopotential height contours from January 18 to January 25, 2021, during the Iqaluit, Canada, ROS event. The white dot represents the ROS location.

When examining a single event's location in relation to the overall block, each case demonstrated an association between an area's position with respect to the occurrence of weather conditions needed for ROS occurrence. All of these locations that experienced a ROS event during these periods fell along the gradient between the main ridge (anticyclone) of the block and the western-most trough, which is seen in Figures 3.1.11-3.1.15. This is important in that this location within the block represents the area experiencing the strongest south-to-north (southerly) flow. This signifies a warm air mass and implies a strong combination of warm air advection and moisture transport through the middle to low levels of the atmosphere. In addition, the nearly stationary setup consistent with blocks provided the duration necessary for the higher temperatures and moisture to build in the warm sector of an approaching storm system or extratropical cyclone.

Locations that fall within this tightened gradient between the trough and the ridge of the block also experience more shortwaves traversing the area. Shortwaves refer to "the relative maximum in geostrophic vorticity associated with one trough portion of the wavetrain," (Bluestein 1993). Shortwaves may also be thought of as another name for cyclones or separate low-pressure or storm systems. The synoptic setup with the block basically guides these progressive shortwaves and associated surface lows through the ROS event area of interest. As these systems move through, each comes with their own warm spell moving with the cyclone's warm sector and subsequent precipitation episodes. Figures 3.1.6-3.1.10 display the evidence of precipitation indicated in the 700-mb procedures for each case; some cases showed additional rounds of shortwaves and consequent bouts of precipitation. The 700-mb procedures demonstrated areas of lift

(rising motion indicated by red negative Omega contours) that coincided with high humidities, which verifies that precipitation is likely occurring.

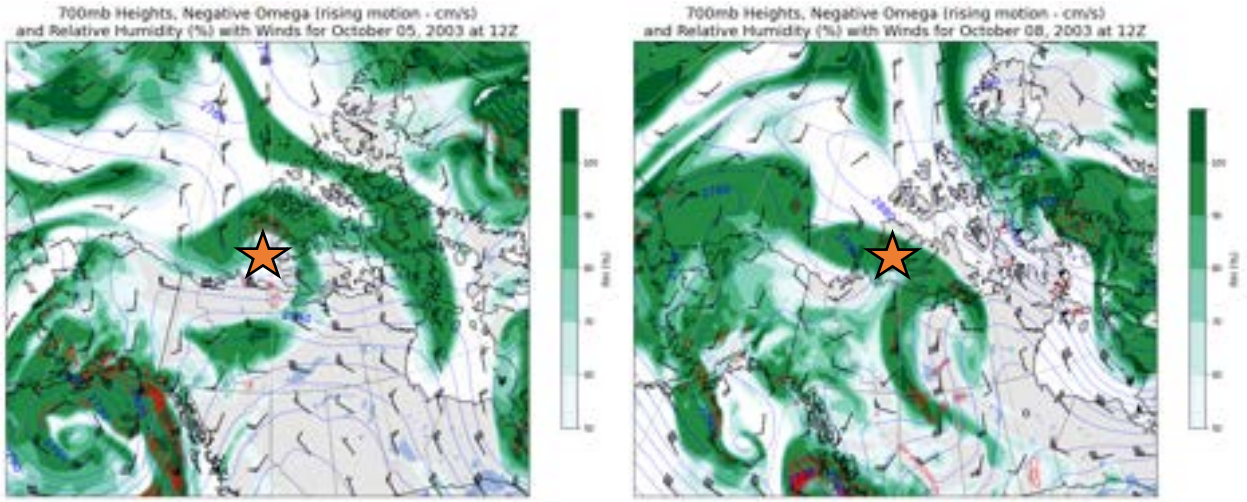

Figure 3.1.6: 2003 ROS Event 700-mb Procedure. This analysis is for the Banks Island, Canada, ROS event from October 2003. Two shortwaves were apparent that produced ROS precipitation during this event. One round of precipitation occurred on October 5, with negative Omega over the island, and another round occurred on October 8.

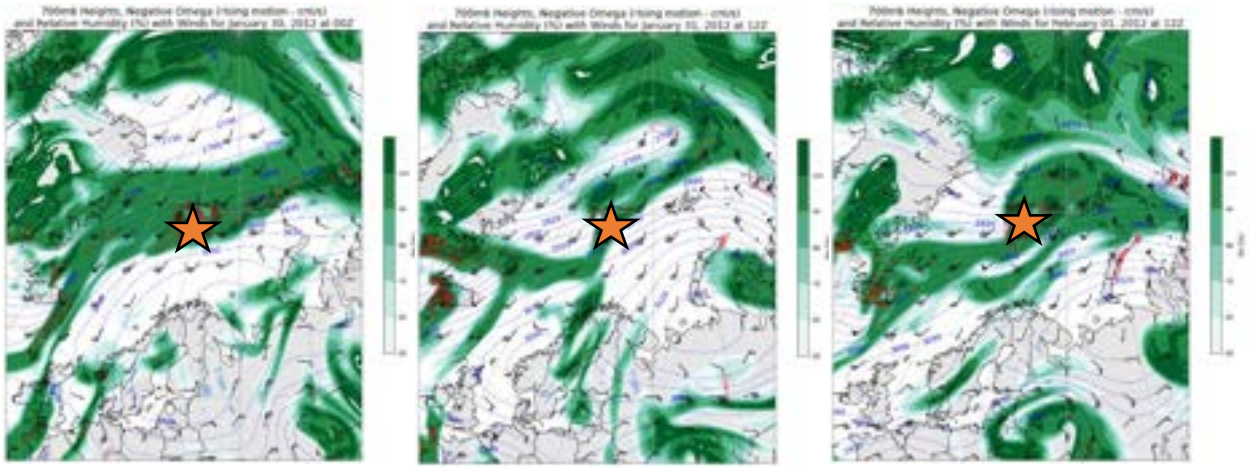

Figure 3.1.7: 2012 ROS Event 700-mb Procedure. This analysis is for the Svalbard ROS event from January 2012. Multiple rounds of precipitation that included ROS conditions fell across the archipelago during the January 30 through February 1 timeframe, with successive shortwaves passing through this North Atlantic corridor. Orographic lift was also likely a factor in delivering even higher localized precipitation amounts to the area.

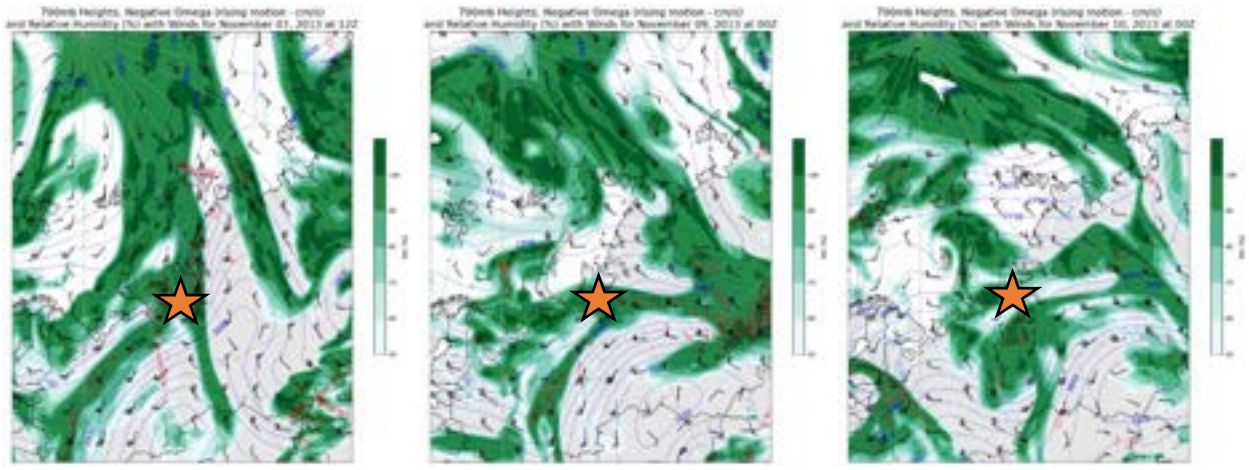

Figure 3.1.8: 2013 ROS Event 700-mb Procedure. This analysis is for the Yamal Peninsula, Russia, ROS event from November 2013. Progressive shortwaves, guided by the ridge of high-pressure over northern Siberia, allowed additional bouts of precipitation along the peninsula from November 7 through the 10, which included ROS conditions during this period.

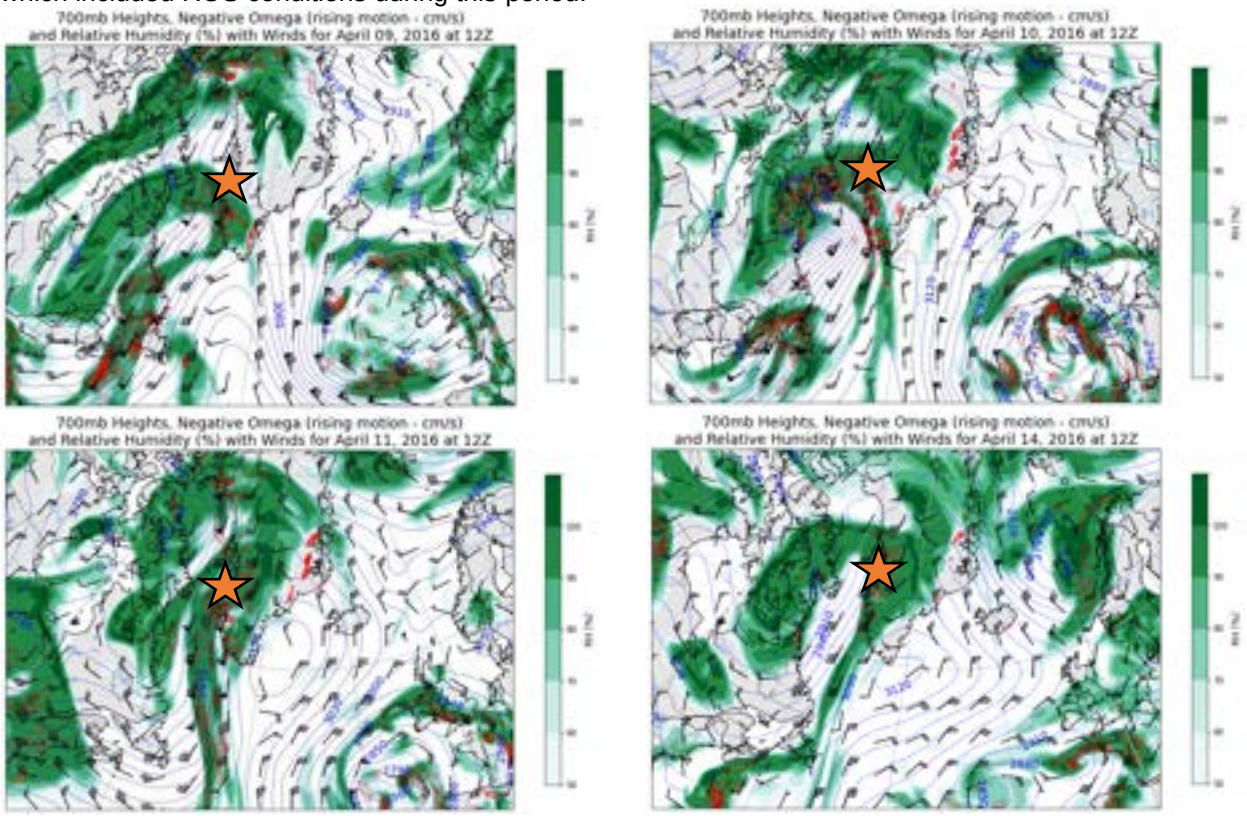

Figure 3.1.9: 2016 ROS Event 700-mb Procedure. This analysis is for the Western Greenland ROS event in April 2016. Leading up to the event, the anticyclonic ridge, seen in the 700-mb height contours, blocked multiple shortwaves from trekking eastward. Instead, the ridge directed them north towards the southwestern edge of Greenland. This generated subsequent precipitation episodes along the west side of the island. April 11 yielded the highest wet snow avalanche activity (see subsection 3.2.4) and concurrent rounds of ROS precipitation, even prior to this day. Like the Svalbard case, orographic lift likely contributed to enhanced localized precipitation amounts. The reanalysis continues to show shortwave activity even after the ROS event, which can be seen in the April 14 panel in the bottom right.

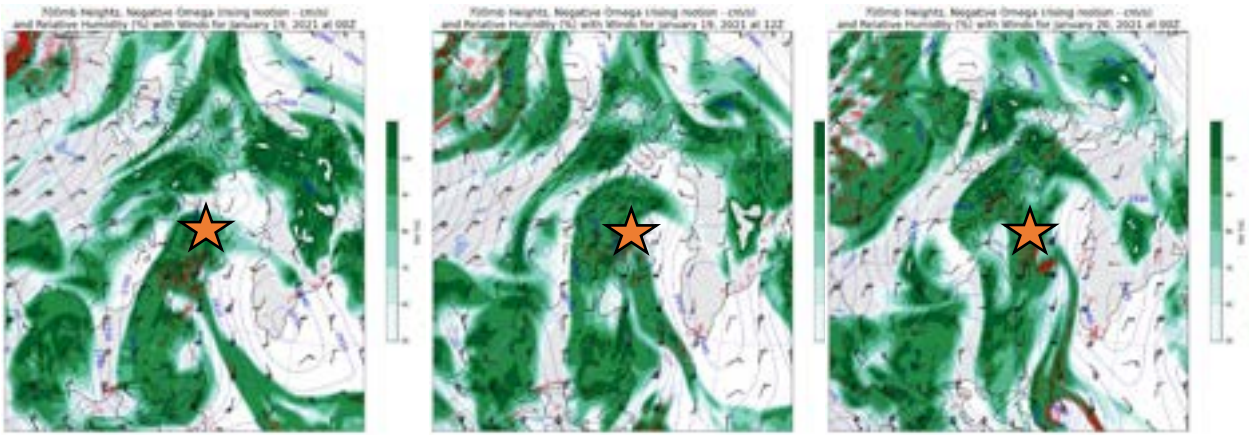

Figure 3.1.10: 2021 ROS Event 700-mb Procedure. This analysis is for the Iqaluit, Canada, ROS event in January 2021. For a period of 24 hours, what appears to be embedded shortwaves – rounding around the deep trough over eastern Canada – impacted the southern periphery of Baffin Island, including the community of Iqaluit. The far-left panel for January 19 represents the 700-mb reanalysis for the day of ROS occurrence. The Iqaluit ROS event represents another case of the blocking high directing shortwaves north to target locations with multiple rounds of precipitation.

The timing of ROS conditions for these locations generally lined up with a strong jet streak of typically southerly winds aloft (Figures 3.1.11-3.1.15). A jet streak defines an isotach (a line of constant wind speed) maximum within the jet stream (Bluestein 1993).This zone of stronger winds also coincided with the tightened gradient between the ridge and western-most trough. This jet streak also greatly influenced jet dynamics through this region, which may have caused additional precipitation through enhanced lift resulting from the jet areas of cyclonic and anticyclonic vorticity advection (Lackmann 2011). The only event where this is not the case (lack of stronger winds aloft) is the Banks Island, Canada, ROS event in 2003. This might be because this case was largely reported as drizzle, and based on the synoptic setup, this is entirely plausible (Rennert et al. 2009). More on this will follow in coming sections.

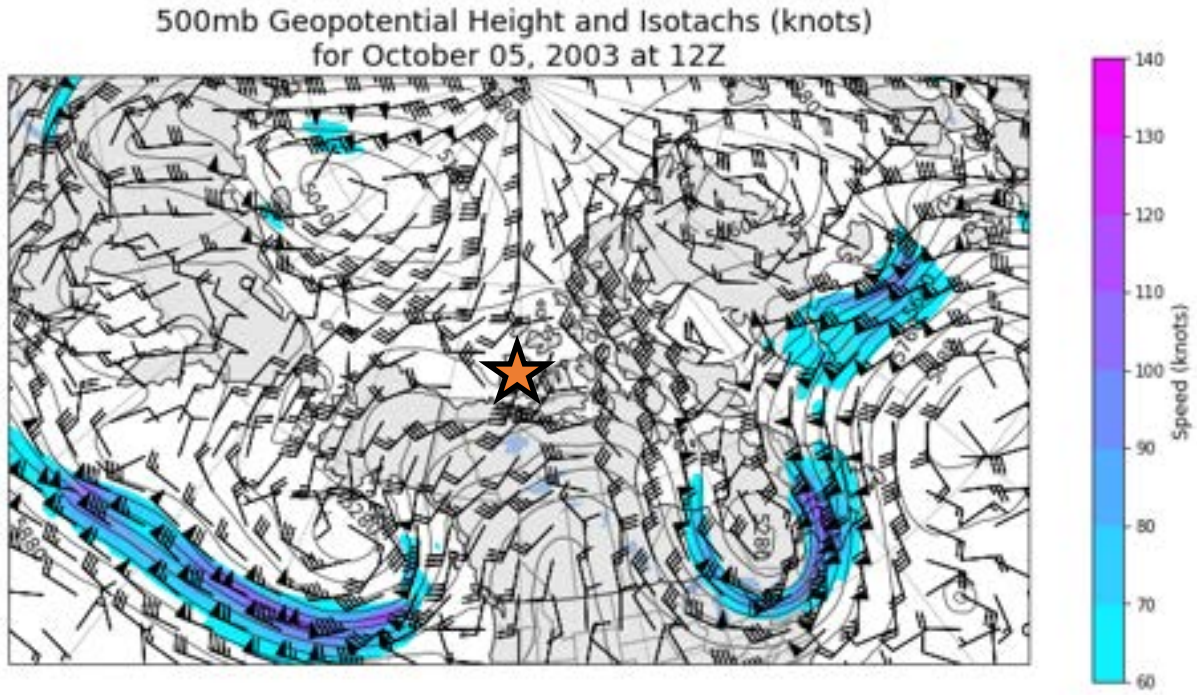

Figure 3.1.11: 2003 ROS Event Upper-Level Block and Winds (Oct 5). For the first part of the Banks Island, Canada, ROS event that began on October 5, 2003, the 500-mb procedure shows the well-defined blocking pattern, with the upper-level ridge centered over western Canada. The 500-mb winds demonstrate the pronounced south-to-north flow on the west side (upstream side) of the ridge and opposite north-to-south flow on the east side (downstream side). The upper-level winds likely contributed to the overall blocking pattern with mostly meridional transport, as opposed to the normal west-to-east geostrophic flow. However, this is the only case where stronger southernly winds were not found directly above the location in the upper levels when ROS conditions were occurring.

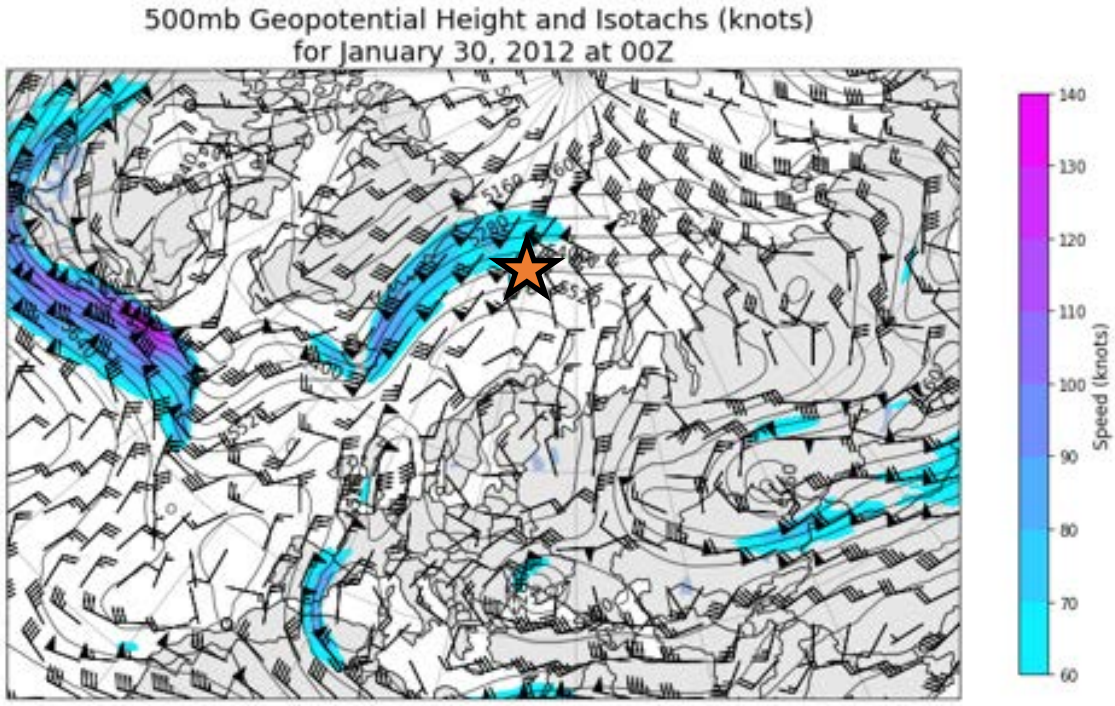

Figure 3.1.12: 2012 ROS Event Upper-Level Block and Winds (Jan 30). For the Svalbard, Norway, ROS event, ROS conditions were occurring on January 30, 2012. The 500-mb procedure shows the blocking pattern as a likely wave breaking scenario. From the black contours, lower heights are positioned across Canada and Greenland, and the other area of lower heights was located across much of Europe, while the ridge was squeezed between these two features and spread over the North Atlantic. This procedure also demonstrates one of the cases where the jet streak of stronger, southerly winds aloft was positioned either directly overhead or very near the area experiencing ROS conditions.

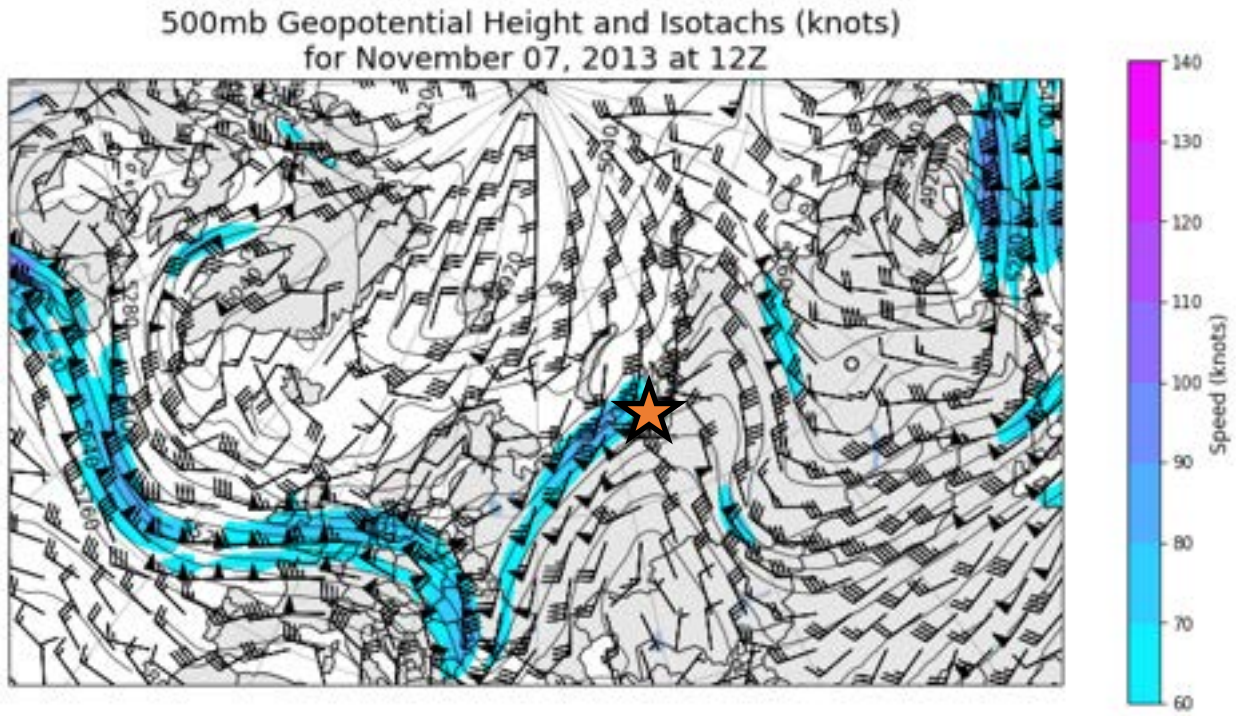

Figure 3.1.13: 2013 ROS Event Upper-Level Block and Winds (Nov 7). The Yamal Peninsula, Russia, case on November 7, 2013 (leading up to the ROS event that took place from November 8-10) appeared as another wave breaking setup, like the 2012 Svalbard event, based on the black geopotential height contours. A shortwave seen in eastern Europe with the 500-mb procedure was associated with two jet streaks, one on the upstream side and one on the downstream side. The jet streak on the downstream side was producing south, southwesterly winds in the 60-80 knot speed range above the location, which confirmed another instance of a strong southerly jet streak aloft with this ROS event.

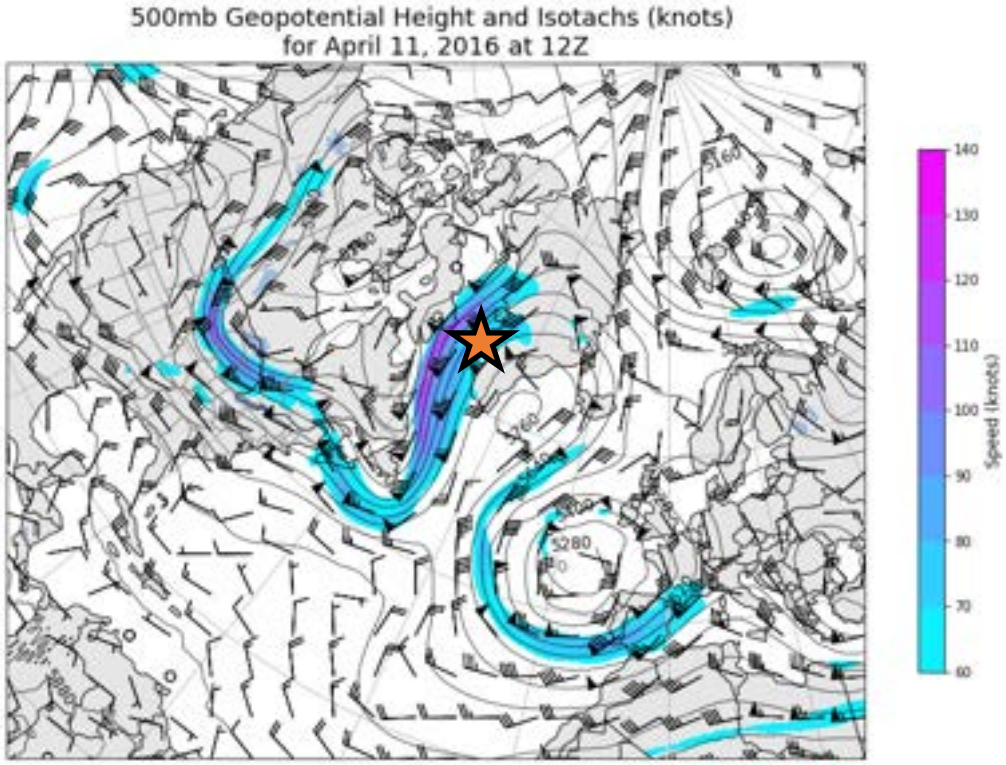

Figure 3.1.14: 2016 ROS Event Upper-Level Block and Winds (Oct 5). Heavy accumulating precipitation and ROS conditions were occurring on April 11. This case presented a textbook example of an Omega Block when looking at the 500-mb black geopotential height contours, with the ridge sandwiched between a broad trough across Canada and a cutoff low near western Europe. This was also the most pronounced example of a jet streak of southerly winds aloft, which can be seen in the filled isotach contours. Recorded winds came in greater than 100 knots through a corridor in Baffin Bay. This equated to a warmer air mass beginning to encroach on southern Greenland and additional jet dynamics for enhanced precipitation.

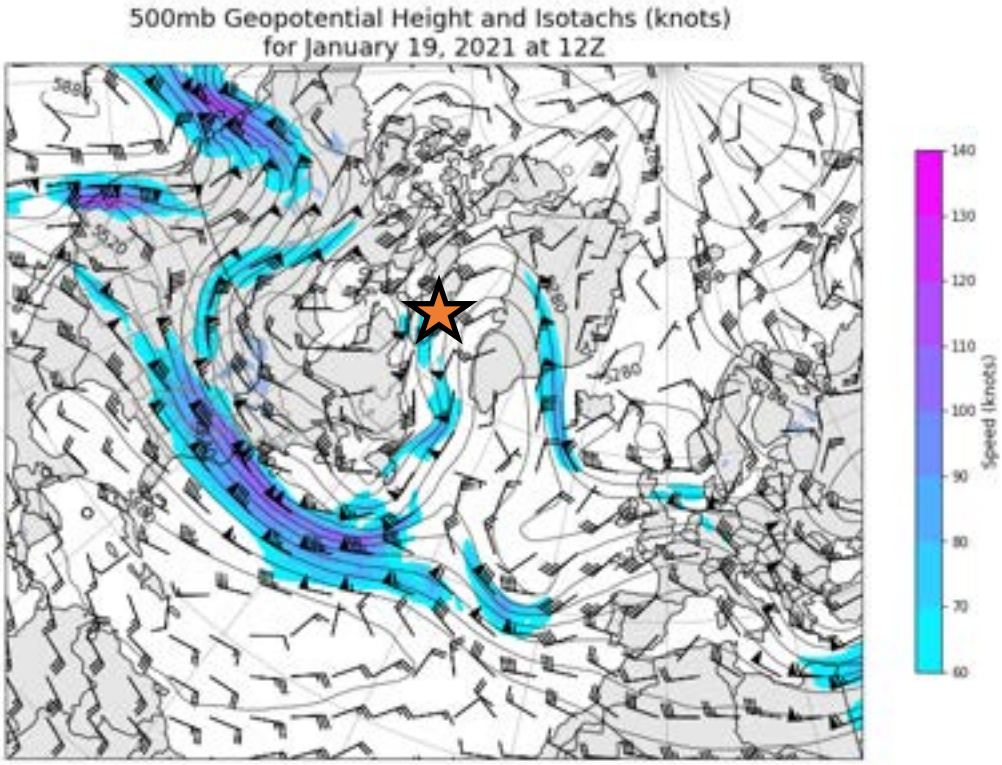

Figure 3.1.15: 2021 ROS Event Upper-Level Block and Winds (Jan 19). This figure shows the upper-level geopotential heights and winds for the Iqaluit, Canada, ROS event that occurred on January 19, 2021, when an eyewitness reported ROS conditions in the area. Like previous cases, this one also had a block at the 500-mb level, but it was likely more representative of a Rex Block or Dipole Block. A zone of stronger southerly winds aloft extended into Iqaluit and through the same upstream area of the ridge. Even though winds were not as strong as some of the previous cases, speeds were still around 50-60 knots through this area, which the lower speeds might have been a result of the weaker block here than in previous cases.

3.1.2: Cyclone-Induced Low-Level Jets, “Warm Noses,” and Plumes of Enhanced Moisture

One of the most striking features with most of these cases was the amplified corridors of strong warm air advection and moisture transport through the middle to low levels of the atmosphere. The cyclone area associated with these features fell within the location of the strongest southerly flow or flow with the strongest southerly component. The warm sector is the area that falls between the warm front and cold front of a cyclone, and it is usually where the warmest air mass may be found. This strong

southerly flow connected to the warm sector moves warmer – and often moister – air to more northern locations. For many of the more maritime influenced locations – such as the Greenland or Svalbard cases – onshore flow also contributed to the higher temperatures and moisture moving into an area. This onshore flow strengthened these warm nose features and these corridors of enhanced moisture by transporting air masses originating over oceanic bodies inland.

Blocks and blocking patterns have already been identified as a primary causal mechanism in the initiation of ROS conditions. This type of synoptic setup provided the time necessary to build these gradients of higher air temperatures, greater moisture, and stronger southerly flow required to transport this warm, moist air mass north. In addition, many cases exhibited strengthened winds out of the south throughout much of the atmosphere but uniquely in the low- to mid-levels. This current of stronger winds implies a cyclone-induced low-level jet (LLJ), usually associated with the progression of an extratropical system.

Atmospheric scientists describe LLJs as a jet typically found at a lower height in the atmosphere and usually associated with the pre-cold-frontal sector of an extratropical cyclone; the LLJ signifies an important driver in what locations may experience precipitation and how much of it (Ralph, Neiman, and Rotunno 2005). This study also adds that “the LLJ is an integral part of extratropical cyclones and is characterized by warm temperatures, weak stratification, large water vapor content, and strong low-altitude winds [Browning and Pardoe (1973), as referenced in Ralph, Neiman, and Rotunno (2005)]. Meteorologists generally agree that the LLJ is found at an altitude of about one kilometer, but the speeds in the studies range from 23.4 meters

per second (approximately 45.5 knots) to the higher end of 35 meters per second (approximately 68 knots) (Lackmann 2002; Ralph, Neiman, and Rotunno 2005). In the Arctic, it may take lower speeds for LLJs to be impactful, with one event near Barrow, Alaska, recording a LLJ of 16 meters per second (approximately 31 knots) that efficiently warmed and moistened the boundary layer (Intrieri et al. 2014).

The following figures (Figures 3.1.16-3.1.21) are designed to show the ample warm air advection and moisture transport occurring in all of these cases, in addition to enhanced movement with a LLJ. All figures contain an 850-mb (top left), a 925-mb (top right), and a mean sea level pressure (MSLP) procedure (bottom middle) with precipitable water (PWAT) overlaid. As described in the “Data and Methods” chapter, the 850-mb procedure shows heights and winds found at that level, but also plots red temperature contours – for values only above freezing (0 °C) – and mixing ratio values, which represent a more effective moisture variable. The 925-mb procedure also includes heights and winds found at that level, but it also displays temperatures at the 925-mb level in the filled blue-to-red contours and a filled, slightly transparent, green contour demonstrating where relative humidities are above 85 percent. The relative humidity contour in the 925-mb procedure is used to show moisture advection with the winds at that level. The MSLP procedure is important in this context, in that it shows the placement of surface-based low-pressure systems – associated with extratropical cyclones and crucial in demonstrating the placement of the warm sector – and the PWAT overlaid provides an idea as to how much moisture was moving with these systems.

Both the 850-mb and 925-mb procedures are meant to show the movement of warm air masses and zones of higher moisture, but they also show areas of warm air advection, moisture transport, and the important LLJ, when the winds are included at these levels. Doing this also reveals how the LLJ links to these warm noses and narrow corridors of moisture. The height equivalent of the 850-mb level ranges from 1000 to 1500 meters, and the height varies from 400 to 800 meters at the 925-mb level. Arctic locations tend to hover around the lower levels of that range because it is colder, so the pressure height is going to be found at a lower height. Subsequently, when these levels are incorporated into the analysis for these case studies, one should be able to detect the presence of a LLJ. Previous atmospheric studies mentioned the 1-kilometer (1000-meter) level used with detection of a LLJ.

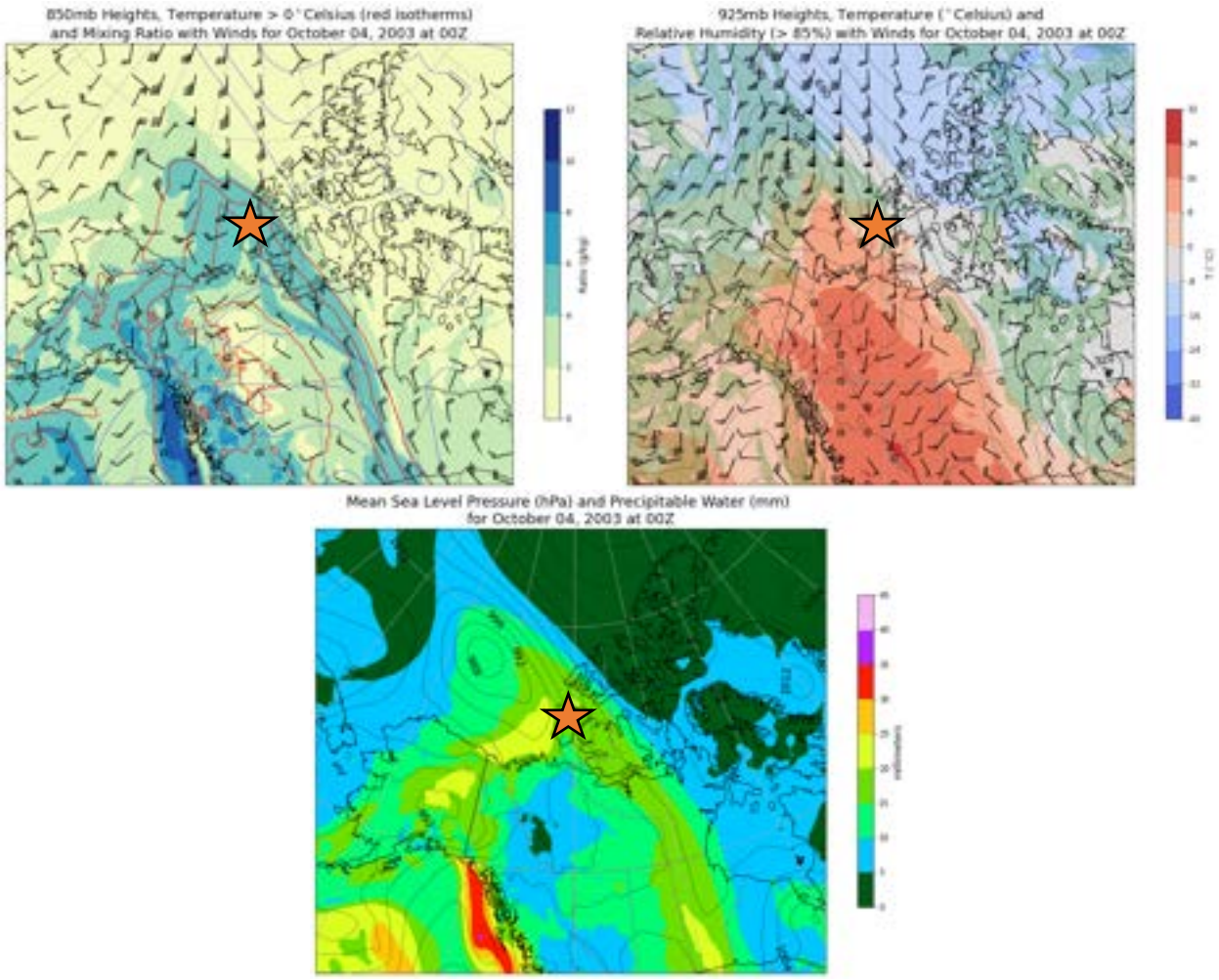

Figure 3.1.16: 850-mb, 925-mb, and MSLP (with PWAT) Analysis for October 4, 2003. This is the lead up to the first reported day of liquid precipitation for the Banks Island ROS event, which occurred on October 5. 850-mb analysis for this day showed elevated mixing ratio values across much of the island and 5-10 °C above freezing at the mid-levels of the atmosphere. 925-mb analysis showed something similar, with air temperatures above 0 °C across most of the island. The 925-mb procedure also showed strong wind speeds, indicative of a low-level jet, ranging from 40-45 knots a few hundred meters above the surface. Multiple atmospheric reanalysis datasets provided a climatology PWAT range of about 6-8 millimeters across Banks Island for this time of year. The MSLP procedure for October 4, 2003, demonstrated PWAT values in the range of 10-20 millimeters across the island, which was well above these climatology values. From the contours in all procedures, a surface low-pressure system was transporting in the higher moisture and warmer temperatures across the western portion of the Canadian Arctic Archipelago, where Banks Island appeared to be in the warm sector of a passing warm front.

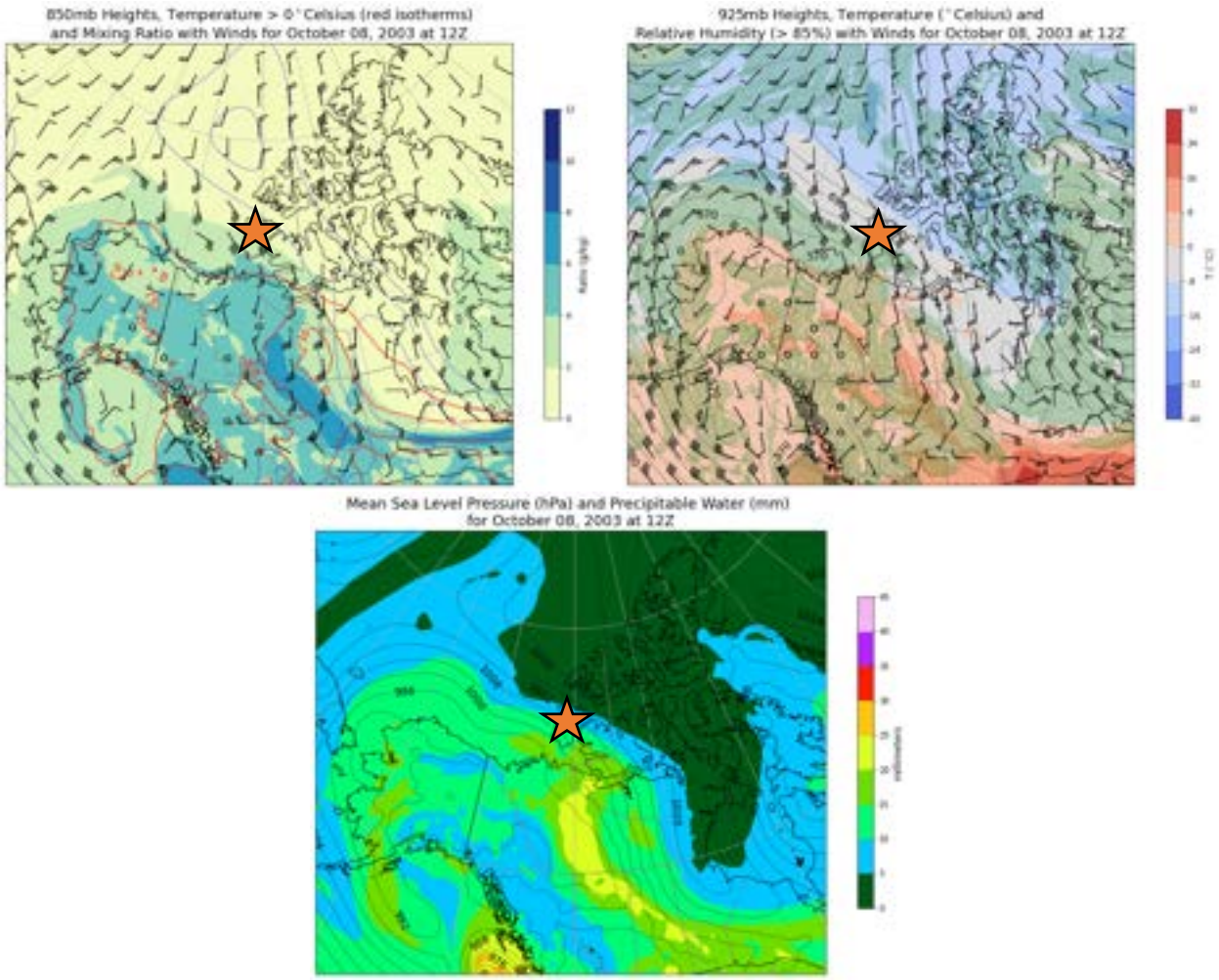

Figure 3.1.17: 850-mb, 925-mb, and MSLP (with PWAT) Analysis for October 8, 2003.This day represents the second half of the Banks Island ROS event case from October 2003 and the second day of ROS conditions. Like what appeared on October 4 in the lead up to ROS conditions, another low-level jet was noticeable in the 925-mb procedure, and higher moisture was present from a corridor extending from the western Canadian interior towards the southwestern portion of the archipelago. In this case, the moisture appeared to be riding up over the ridge, directed by a broad low-pressure system centered over south-central Alaska and the North Pacific. This indicated a drizzle scenario. Air temperatures were not as warm throughout the mid- and low levels, but they still hovered around the freezing mark of 0° C in both the 850- and 925-mb levels. PWAT values were closer to average (climatology values are 5-7 millimeters for October 8) on the north end of the island but remained above average across the southern portion of the island, with 15 millimeters being the higher end of the light green contour.

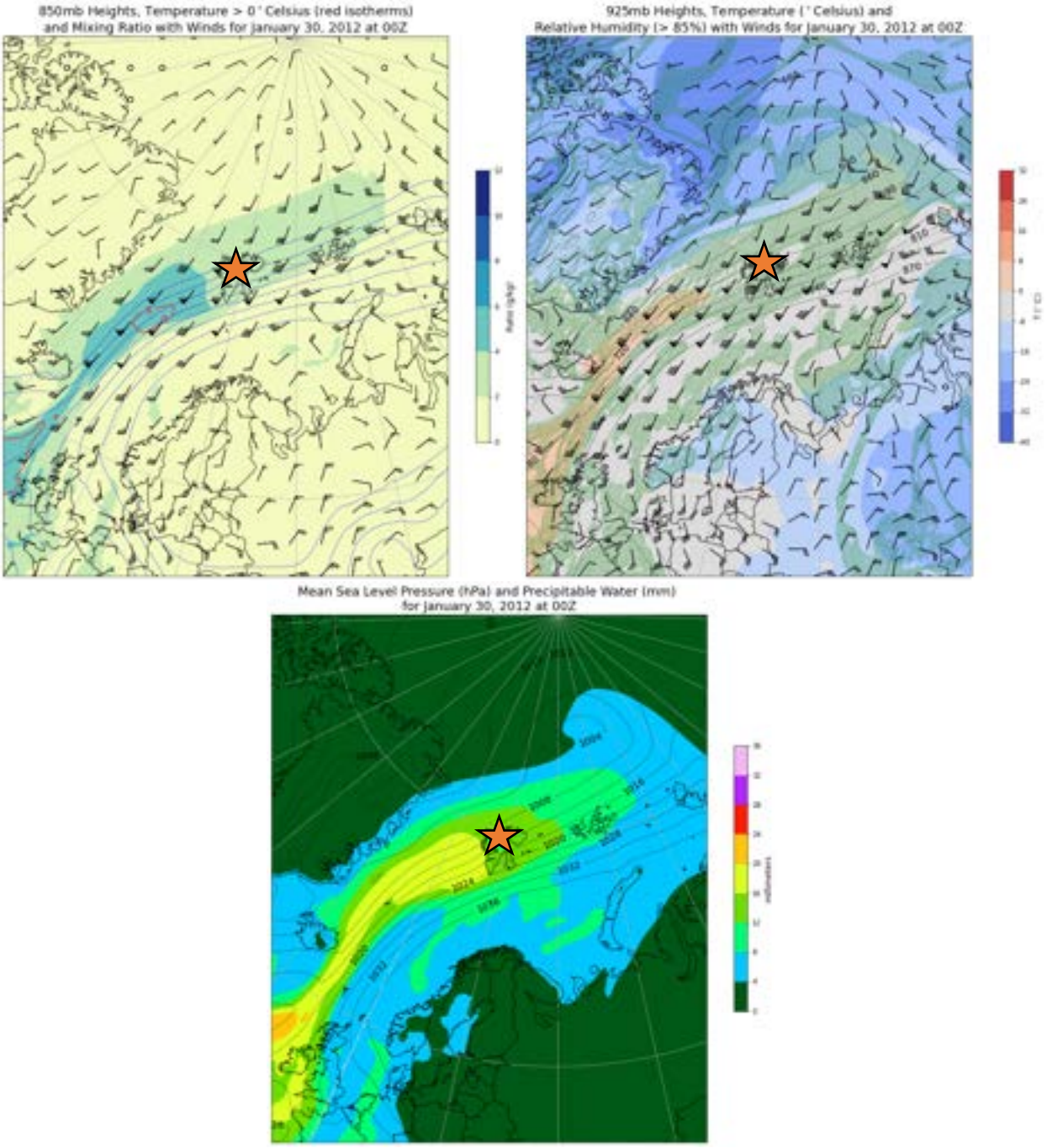

Figure 3.1.18: 850-mb, 925-mb, and MSLP (with PWAT) Analysis for January 30, 2012. There was a well-defined plume of moisture with the Svalbard, Norway, ROS case (from the MSLP with PWAT analysis), carried by over 50 knots of wind through the low- to mid-levels, which can be seen in all procedures. At the 925-mb level, air temperatures were in the (-8)-0 °C range, so they were close to freezing across Svalbard, but higher temperatures were found in a corridor to the southwest. However, referring to the later analysis in subsection 3.2.2 – which consists of additional background and differences regarding the Svalbard case – ROS conditions were occurring. Climatology for January 30 revealed that the normal PWAT range for Svalbard is approximately 2-5 millimeters, and PWAT values were in the range of 8-16 millimeters across Svalbard.

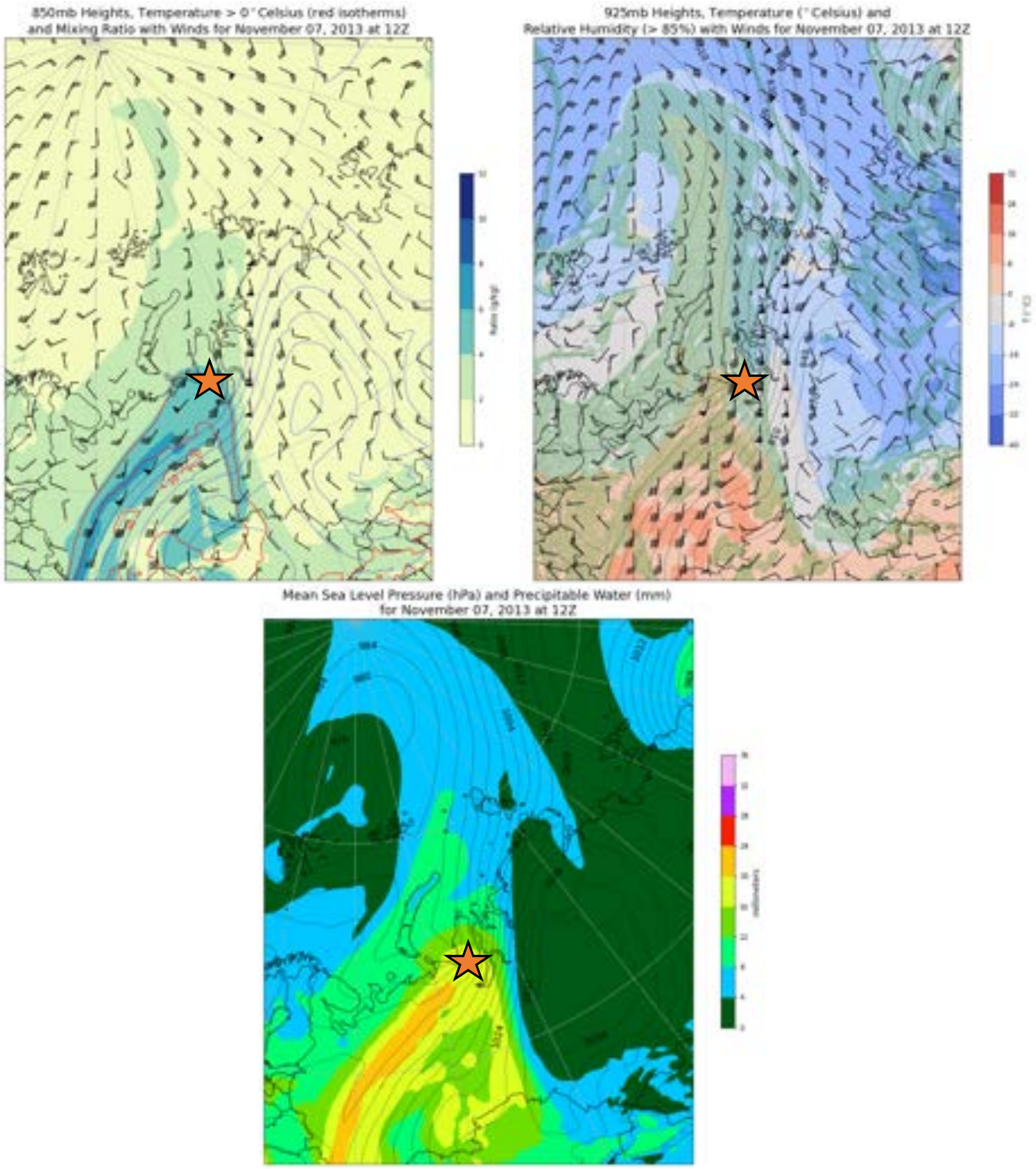

Figure 3.1.19: 850-mb, 925-mb, and MSLP (with PWAT) Analysis for November 7, 2013. In the lead up to the ROS event on the Yamal Peninsula in November 2013, a clear warm nose and concurrent moisture plume formed along the gradient between a high-pressure system across the continental interior of Russia and two cyclonic features, one over the peninsula and another progressing north into the Arctic Ocean. Wind speeds ranged from 40-50 knots in the 850-mb and 925-mb procedures, indicative of a LLJ. Geographically, air temperatures above the 0 °C mark were found near the northern edge of the Ural Mountains and the southern tip of the Yamal Peninsula. PWAT values were above average at 8-20 millimeters, with the higher values located along the southern portion of the peninsula and coinciding with the higher air temperatures. Average PWAT for November 7 equates to 5-7 millimeters.

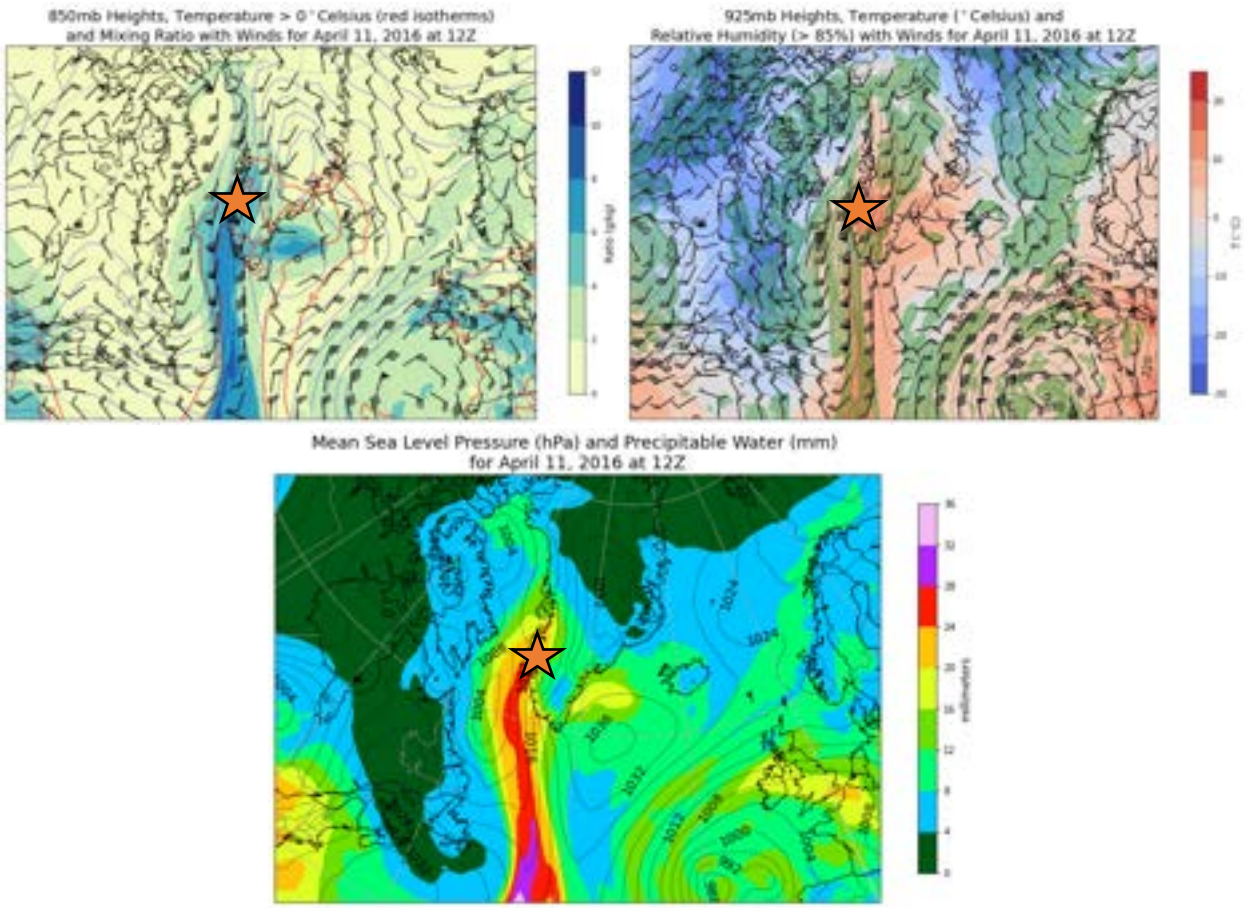

Figure 3.1.20: 850-mb, 925-mb, and MSLP (with PWAT) Analysis for April 11, 2016.This ROS case from Western Greenland presented the most impressive example of a warm nose of higher temperatures and a narrow area of higher moisture. The reanalysis on April 11 showed air temperatures 5-10 °C above freezing from the 925-mb and 850-mb level procedures. Much of the southwest coast of Greenland saw PWAT values around 12-16 millimeters, but some locations peaked around 20-24 millimeters. Climatology values of PWAT on April 11 average between 2-7 millimeters from the southwest coastline and extending inland. The wind speeds were also striking with this case, reaching 75 knots at some locations along the southwest coastline from the low- to mid-levels. The strong LLJ for this ROS event – in addition to the position of moisture sources (North Atlantic) and the overall blocking setup – made the air temperature and moisture transport higher than in all other cases.

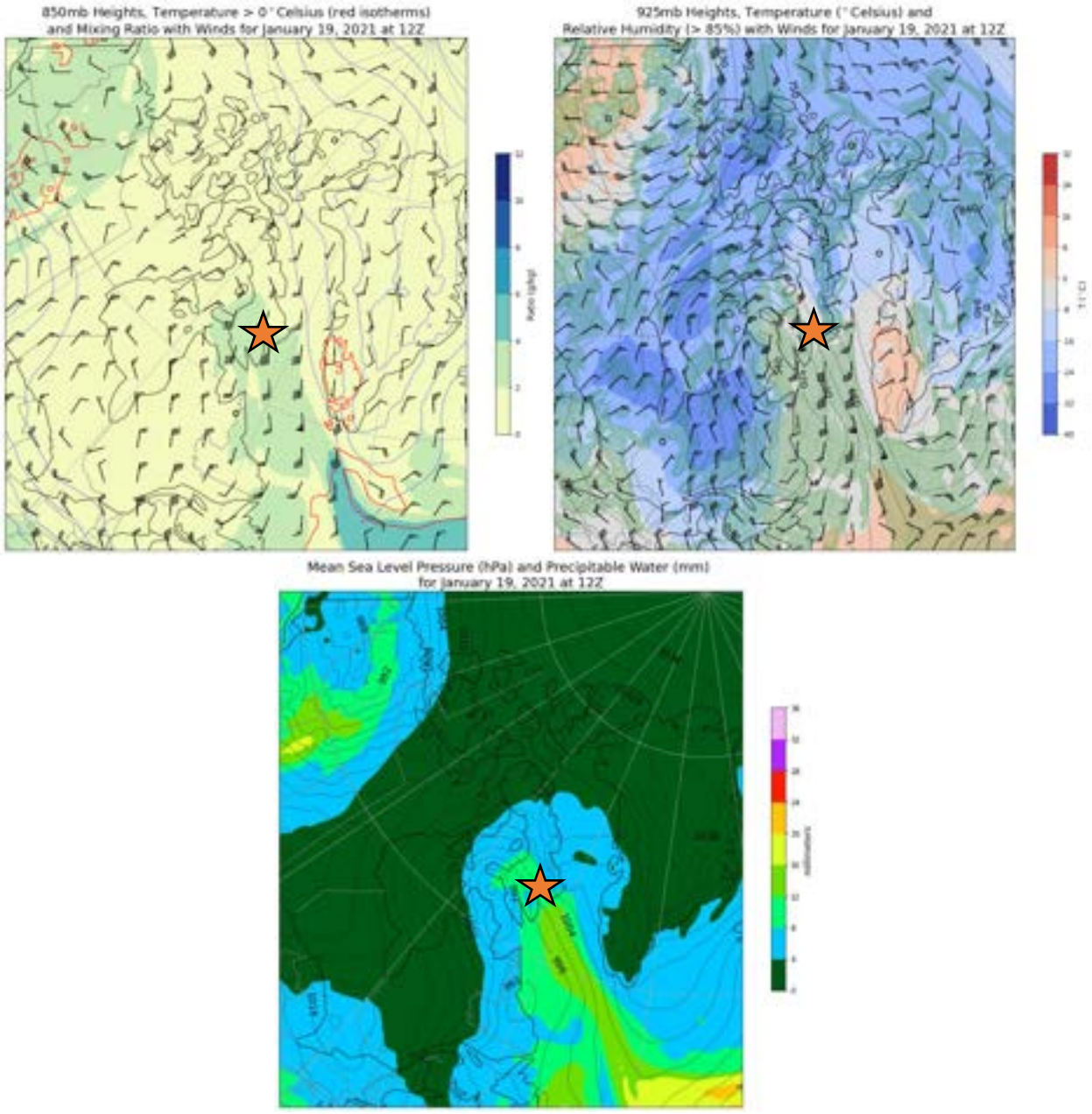

Figure 3.1.21: 850-mb, 925-mb, and MSLP (with PWAT) Analysis for January 19, 2021. Like previous ROS cases, the ROS event that occurs in Iqaluit, Canada, on January 19, 2021, presented similar narrow zones of higher air temperatures and moisture variables. Above freezing air temperatures did not appear present over Iqaluit in the 850-mb procedure, unlike other cases. However, the 925-mb procedure showed temperatures in the (-8)-0 °C range just a few hundred meters above the surface. Comparatively, a LLJ was also present with this case, like other previous cases. Wind speeds recorded at the 850-mb level reached 40-45 knots just offshore of Iqaluit, and wind speeds reached 40-50 knots just below it at the 925-mb level. PWAT values represented above average conditions in the range of 8-12 millimeters across the southern tip of Baffin Island. These PWAT values demonstrated a higher range than climatology values, which approximate to 1-4 millimeters for this day.

All cases showed similar narrow streams of intensified higher air temperatures – in combination with enhanced warm air advection – and increased moisture transport. They also generally fell within the same location in the synoptic setup, within the gradient of the western-most trough and the anticyclonic ridge of the overall blocking pattern. The presence of a LLJ was also detected (in some form or another) among all cases. The combination of these features among the ROS events documented a crucial process for moving both the additional moisture for precipitation and the increased temperatures needed for liquid precipitation (or freezing rain) from lower latitudes to the Arctic.

This production of largely rain or freezing rain overcame the lack of solar heating during the late autumn through winter months at these locations to initiate the liquid precipitation necessary for ROS events. The LLJ connected with the warm sector of the cyclone moving through these locations, so temperatures increased ahead of the inevitable cold frontal passage. Once the cold front progressed through the area, with the cyclone then moving on, temperatures decreased, allowing the liquid overtop of the snowpack to freeze and form a layer of ice. This was consistent with the previous discussion on conditions leading to ROS events (see Section 1.3, Figure 1.5) and was represented at certain observation sites in individual case examinations discussed later. These “warm nose” features, LLJs, and increased moisture transport were well represented among the upper air sounding data, which will also be discussed, including the differing strength of these features and their varying heights found within the atmosphere among the cases.

3.1.3: Indirect and Direct Effects from Atmospheric Rivers

The previous subsection underscored the importance of cyclone-induced LLJs associated with the increased warm air advection and moisture transport that occurred in varying strength for all ROS case studies. In this subsection, it is shown that LLJs also have a connection to the formation of atmospheric rivers (ARs). Other researchers examining ARs have emphasized the importance of LLJs in ARs, in that ARs typically cannot be found without this feature (Martin Ralph, Neiman, and Rotunno 2005; Guan and Waliser 2015). In the context of the ROS cases examined here, ARs were found to play direct and indirect roles in the impacts with these ROS events. A direct effect – demonstrated in this thesis – indicates that an AR physically made landfall at the location that experienced ROS conditions. Indirect effects mean that an AR may have been present in another area and that a cyclone or multiple cyclones stripped off and transported moisture from the AR northward to the ROS event location.

Recall that ARs represent long, narrow streams of moisture, with a structure that carries moisture poleward out of the tropics, and they play a notable role in global hydrological processes (Zhou et al. 2021). Researchers have acknowledged that ARs can influence ROS events. When ARs occur during the winter months, they cause the atmosphere to warm, and consequently, the freezing level also rises (Guan et al. 2016). These higher freezing levels lead to rain as the dominant precipitation type for higher elevations, which results in increased runoff over a greater catchment area (Guan et al. 2016). Guan et al. (2016) also mention that rain accumulating overtop of an existing snowpack can produce additional runoff because of melting snow.

Many studies have attempted to identify ARs in a quantitative sense using climate datasets. Uncertainty around this methodology remains, but some studies have sought agreement regarding some of their traits. Zhou et al. (2021) attempted to compile all the various detection methods used in research over the years:

> "There are two major kinds of thresholds: absolute thresholds specified by spatially and temporally invariant values of IVT [integrated water vapor transport] or IWV [integrated water vapor], and relative thresholds specified by fixed percentiles of spatiotemporally varying IVT or IWV. Additional thresholds include geometric constraints, such as the length-width ratio of an AR object," (Zhou et al. 2021).

Additionally, AR lifecycle characteristics fall into categories of lifetime, propagation speed, and intensity. Landfalling ARs in North America, for example, may be categorically ranked, based on maximum IVT values in the range of 250-1250 kg m^{-1} s^{-1} and IVT thresholds exceeding 250 kg m^{-1} s^{-1} for a 24-72-hour period (Zhou et al. 2021).

For the present research, a similar approach was used to identify ARs from a forecasting perspective. Specifically, a comparable methodology was utilized where ARs were defined "as a continuous region $\geq$ 2000 km [kilometers] in length with IVT $\geq$ 250 kg m^{-1} s^{-1}," (Rutz, Steenburgh, and Ralph 2014). This IVT threshold was notably used in a study on forecasting ARs for a multiyear field campaign that analyzed which features influenced water supply and applicable extreme events across the western United States (Cordeira et al. 2017). In addition, ROS locations needed to exhibit air masses originating from within the tropics or subtropics (near and south of 30 °N) to qualify as a direct impact from an AR; if this requirement was not met, the event was

classified as an indirect impact from an AR, if an AR was present. Despite ARs in the Arctic likely requiring lower thresholds, it is of value to see if this threshold is reached in any of the ROS events. In later sections, the HYSPLIT results assisted in quantifying if an AR led to direct or indirect impacts, and the supplemental MSLP procedure (with overlaid PWAT values) helped in gaining an understanding of where the water vapor may have originated.

As evidenced in Figures 3.1.22-3.1.27, ARs represented another common feature among all of these ROS cases. In some instances, they varied in strength when examining the IVT values associated with each event. However, they all met the 250 kg m^{-1} s^{-1} IVT criterion. In addition, these ARs played different roles among the cases. Some cases – like the ROS events from Svalbard and Western Greenland – indicated direct landfall of an AR, likely leading to enhanced warming and moisture transport necessary for ROS conditions in the Arctic. Other cases – like the ROS events from Banks Island, the Yamal Peninsula, and Iqaluit – represented instances where ARs played more of an indirect role. This is discussed further within the figure descriptions.

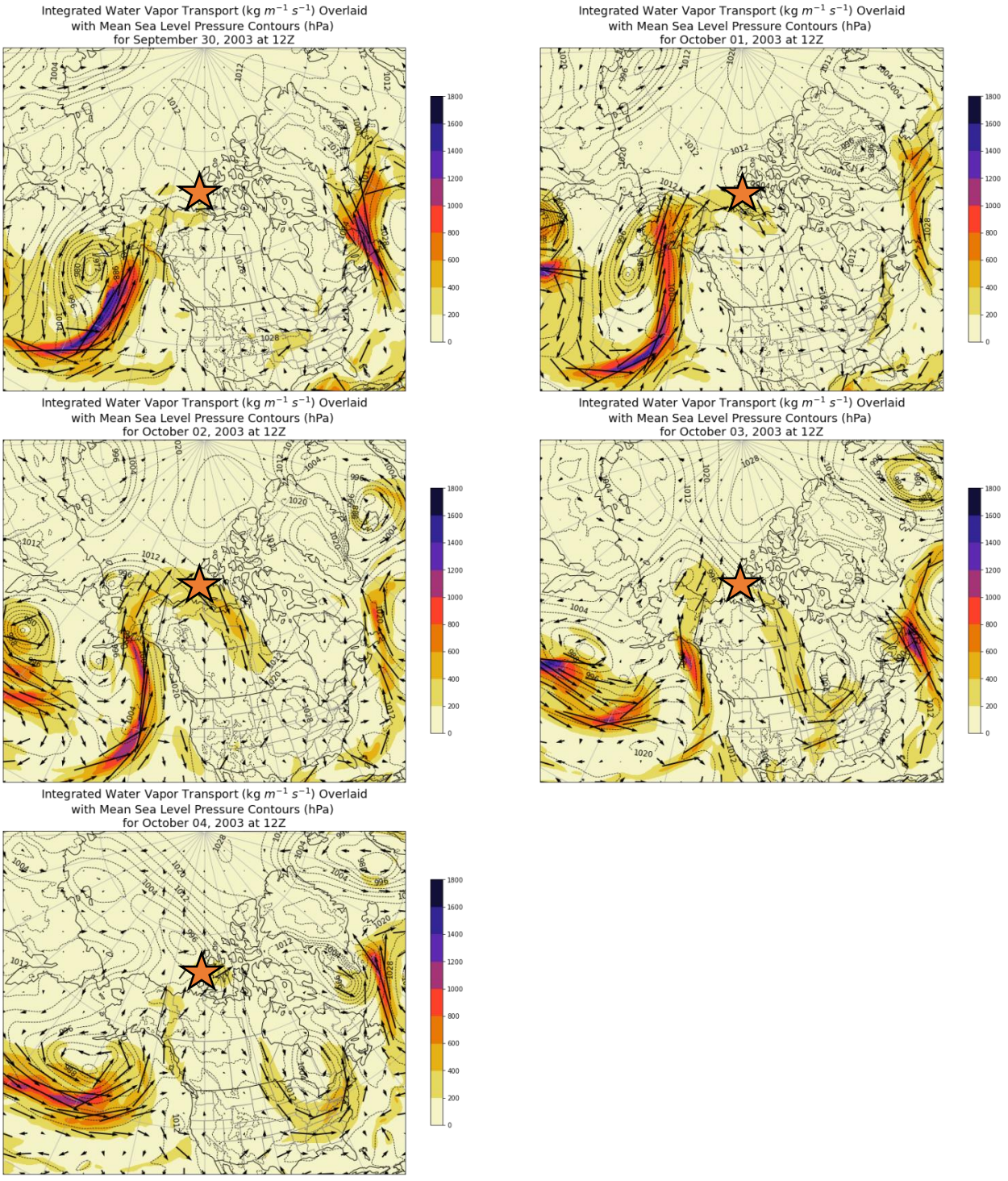

Figure 3.1.22: 2003 ROS Event IVT (Part 1). This sequence is during the early part of the Banks Island ROS event from early October 2003. A probable AR was positioned over the Pacific with high IVT and maximum values greater than 1,000 kg m^{-1} s^{-1}. This leads up to the initial precipitation event beginning on October 5. Moisture from the AR was forced up and over the ridge by a strong cyclone in the North Pacific, combined with a secondary cyclone north of Alaska that was apparent in the October 2 and 3 images. For both the first and second halves of this ROS event, ARs led to indirect impacts on ROS conditions at Banks Island, since it was not a direct landfall, but through moisture provided by the AR.

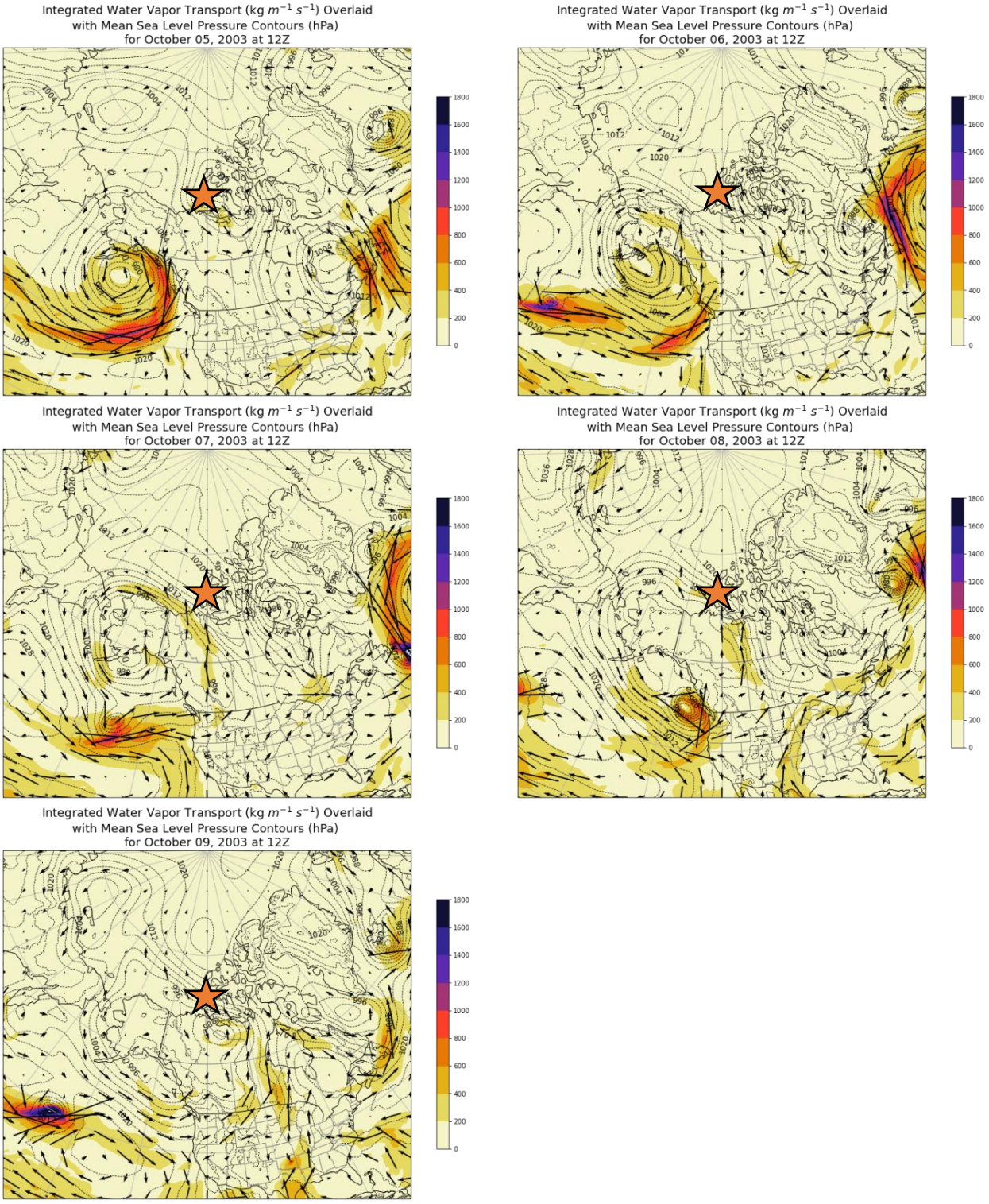

Figure 3.1.23: 2003 ROS Event IVT (Part 2). This sequence is during the second part of the Banks Island ROS event from early October 2003. Here, there was likely another – albeit weaker – AR making landfall in South-Central Alaska on October 5. Maximum IVT values ranged from 600-800 kg m^{-1} s^{-1}. This sequence indicated another instance of a deep extratropical cyclone over the North Pacific guiding moisture north, which then rides up and over the deep ridge across continental western Canada. This produced additional freezing drizzle through the October 8 period for Banks Island.

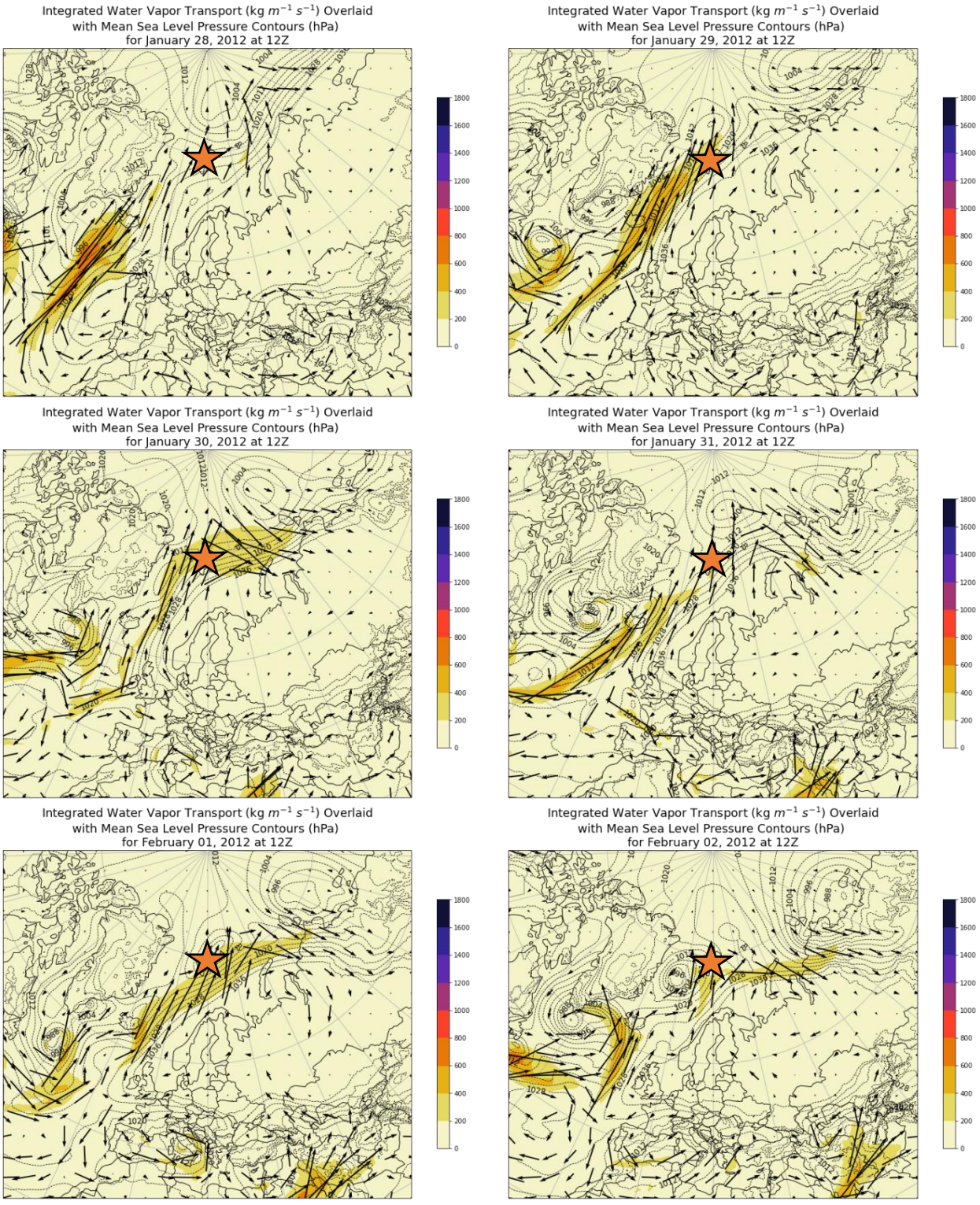

Figure 3.1.24: 2012 ROS Event IVT. This sequence is during the Svalbard ROS event beginning in late January of 2012. On January 28, an AR with maximum IVT values of 600-800 kg m^{-1} s^{-1} streamed into the North Atlantic, making landfall with Iceland. It traveled north, making landfall with Svalbard by January 29 and retaining IVT values of 400-600 kg m^{-1} s^{-1}. This was impressive since this location was well north of the Arctic circle and during the winter months of January and February.

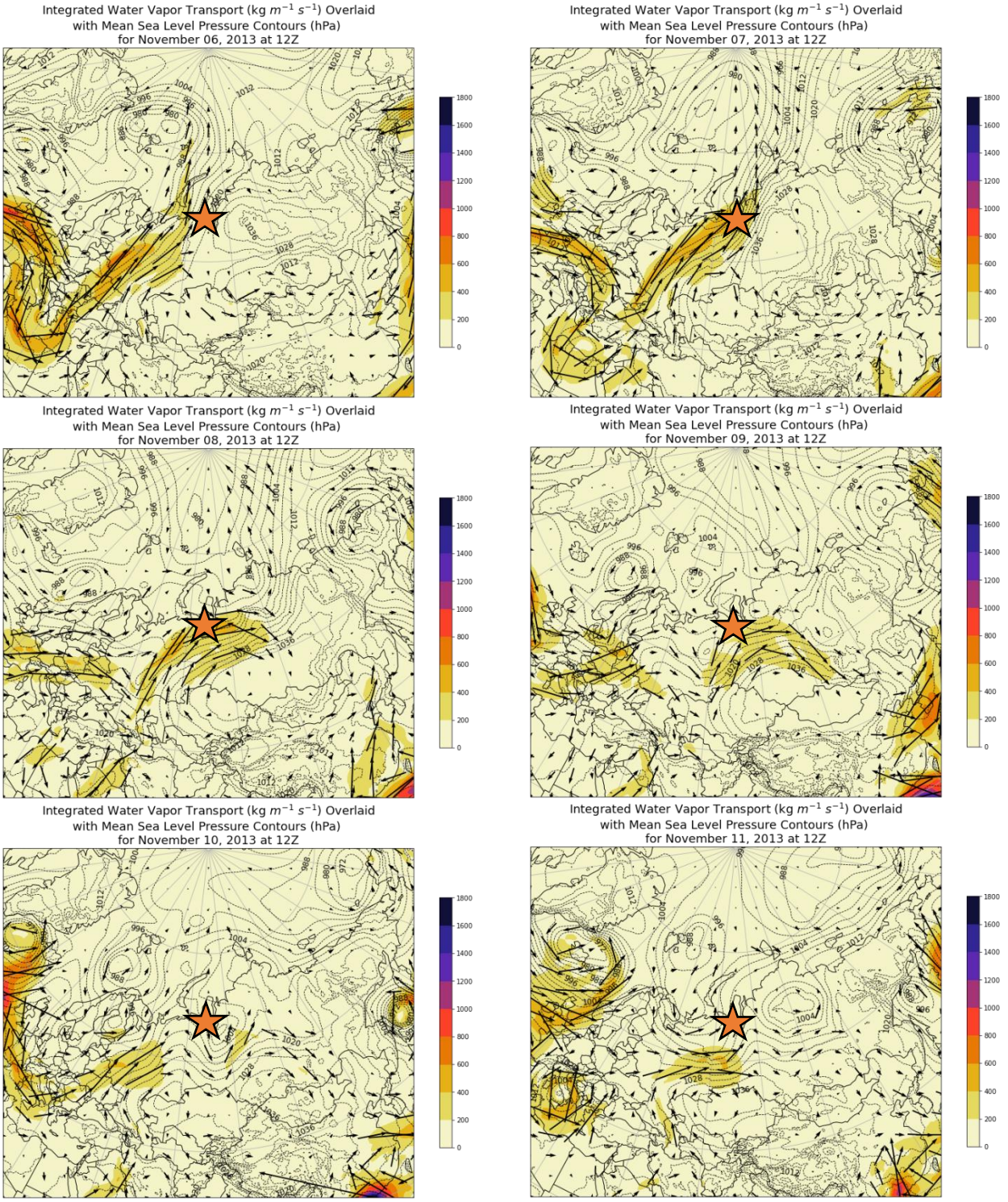

Figure 3.1.25: 2013 ROS Event IVT. This sequence is during the Yamal Peninsula case in November of 2013. An AR appeared to be making landfall in northern Europe on November 6, with maximum IVT values of 800-1,000 kg m^{-1} s^{-1}. Moisture from this feature followed a shortwave into eastern Europe, and another deeper cyclone moving into the Arctic Ocean supported additional moisture movement. This allowed IVT values of 400-600 kg m^{-1} s^{-1} to push along the ridge gradient and across the peninsula by November 7. This implied an indirect impact with an AR providing the moisture for a ROS event well away from the location.

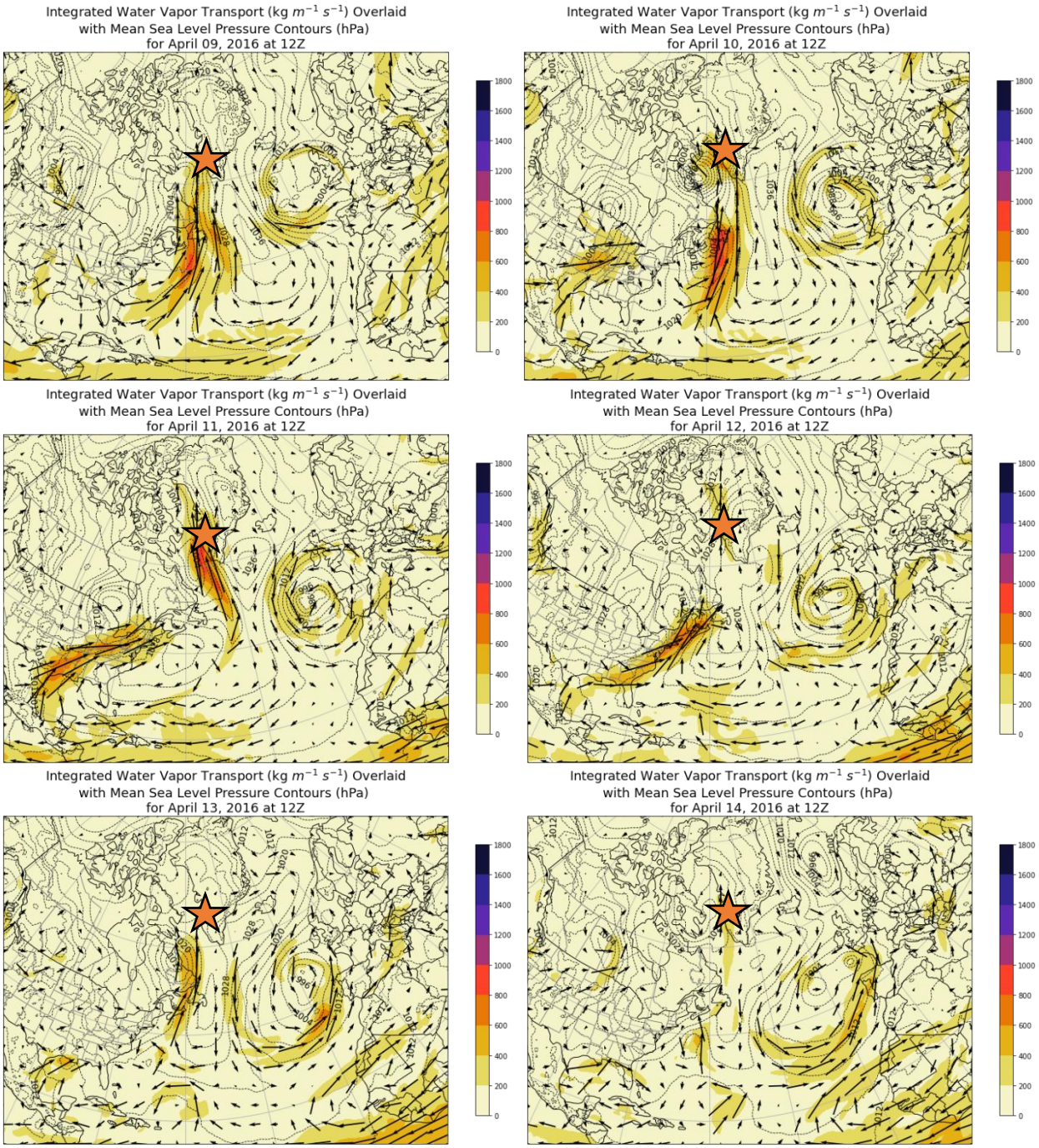

Figure 3.1.26: 2016 ROS Event IVT. This sequence is during the western Greenland ROS event from April 2016. The ridge across the North Atlantic likely assisted in pulling moisture from the tropics to form an AR just off the east coast of Canada beginning on April 9. Maximum IVT values ranged between 800-1,000 kg m^{-1} s^{-1}. Successive shortwaves proceeded in moving the enhanced moisture north. This was another case – like the one from Svalbard in 2012 – of an AR directly making landfall with the location of interest and likely influencing the occurrence of ROS conditions. IVT values even remain at the 800-1,000 kg m^{-1} s^{-1} range as the moisture impacts the southwest coastline of Greenland on April 11. ROS conditions were also confirmed on April 11.

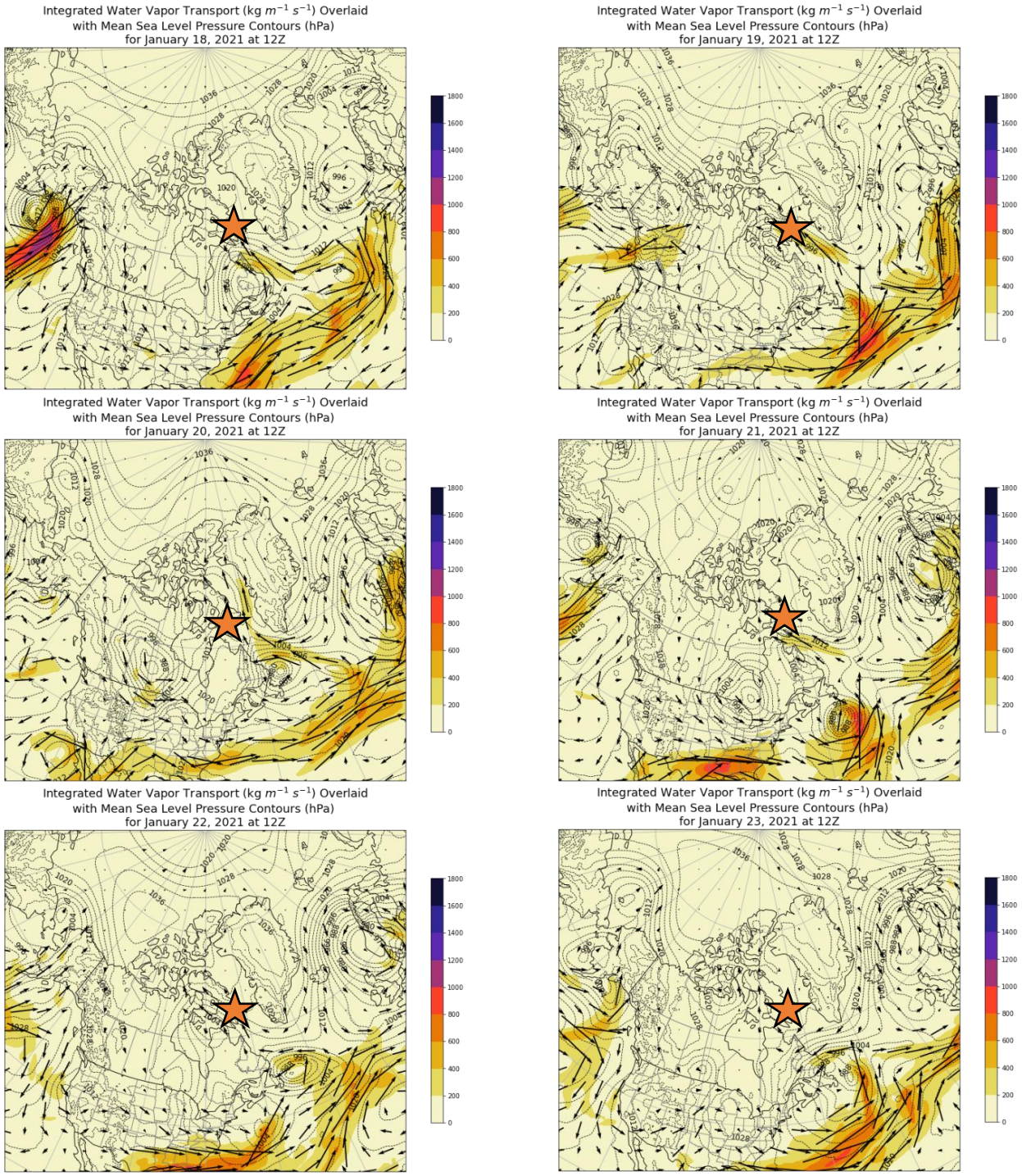

Figure 3.1.27: 2021 ROS Event IVT. This sequence is during the Iqaluit, Canada, ROS event in January 2021. What appeared to be an AR – parallel to the eastern coastline of the US and extending east, northeast into the North Atlantic – exhibited maximum IVT values between 800-1,000 kg m^{-1} s^{-1} along the southeast coast of the US on January 18. For this case, a somewhat strong shortwave carried moisture from this AR corridor north into the southern tip of Baffin Island, enough warm air and moisture transport to produce ROS conditions in Iqaluit on January 19. This ROS event represented another instance of an AR contributing indirectly to this case, not making landfall. However, IVT still reached decent values of 200-400 kg m^{-1} s^{-1} across southern Baffin Island with the associated shortwave on January 19.

Additionally, the moisture for the ARs in these cases could be tracked to sources within the subtropics and even further south to tropical locations. The zoomed-out images of the MSLP procedure (Figures 3.1.28-3.1.33) – with PWAT overlaid – provide an understanding of both where the moisture was originating from with these ARs and if these AR-like objects met the threshold of a length of 2000 kilometers. In all cases, whether ARs led to direct or indirect impacts, this threshold was met with all potential AR features, meaning that these enhanced corridors of moisture transport in these cases were all ARs. Potential moisture sources in these cases included slightly north of the latitude for the Hawaiian Islands in the Pacific and locations in the Caribbean and just around 30° N latitude, northwest of Africa in the Atlantic.

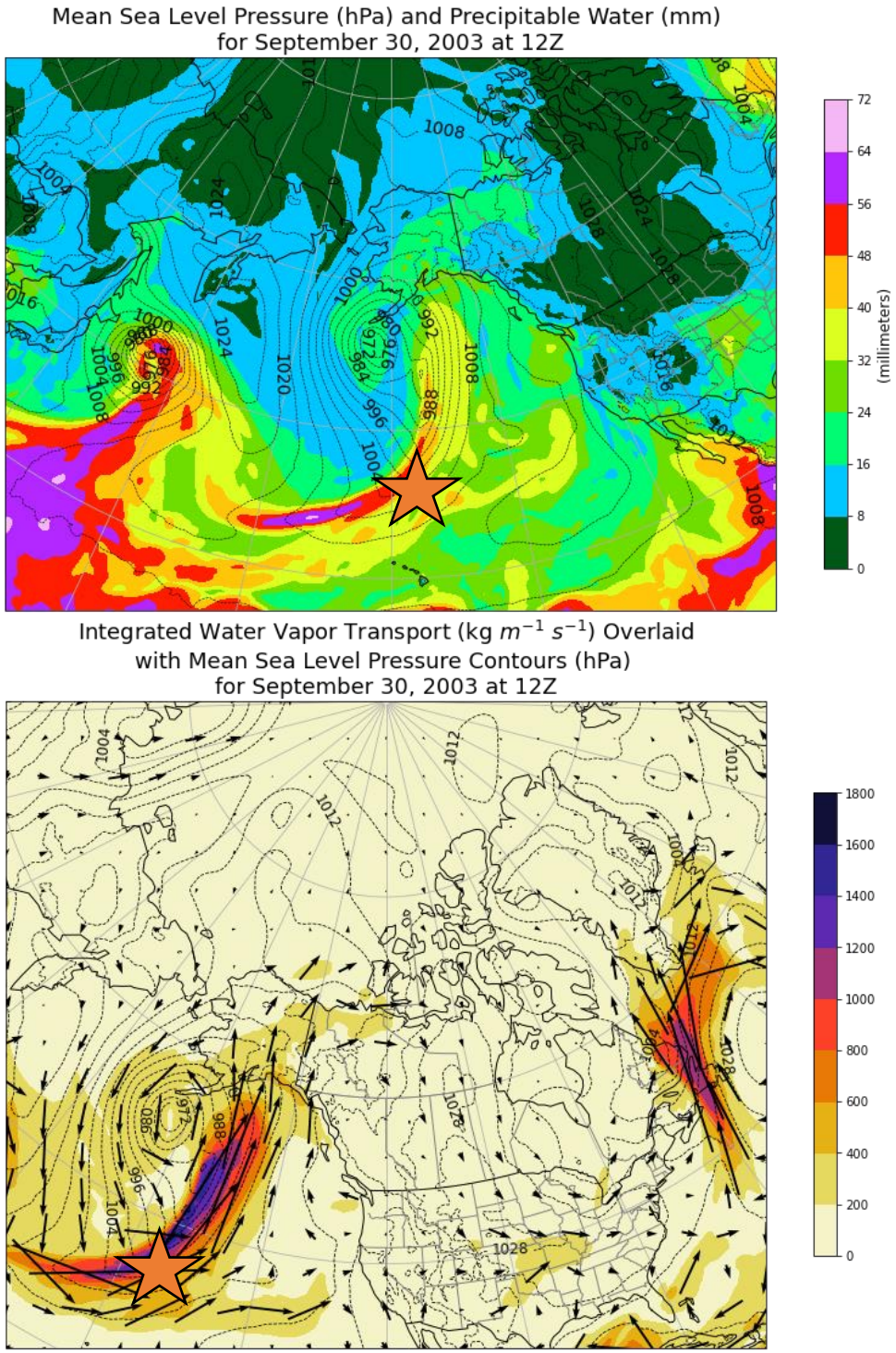

Figure 3.1.28: Tracking ARs for the 2003 ROS Event (Sept 30). This figure shows the MSLP procedure, with overlaid PWAT (top image), and corresponding IVT procedure (bottom image) for Banks Island ROS event on September 30, 2003, at 12Z. The star indicates the same positional reference in each image, denoting the same AR-like feature. This plume of moisture extended from just south of South-Central Alaska to an area just over 1,000 kilometers west, northwest of Hawaii. Based on the distance criteria for ARs, this AR extended well over 2,000 kilometers, and from the IVT, it also broke the threshold of just 250 kg m^{-1} s^{-1} with maximum values well above 1200.

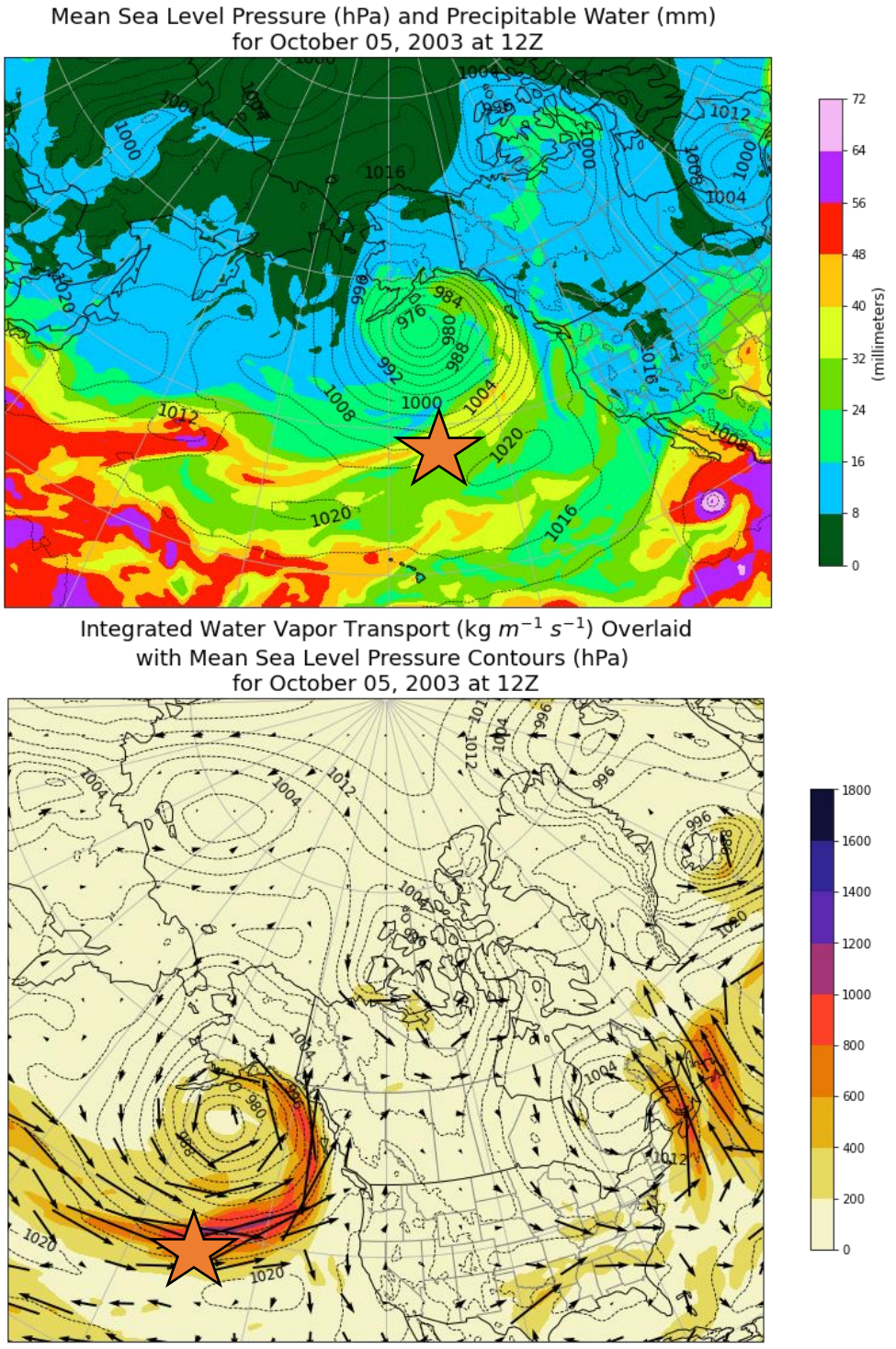

Figure 3.1.29: Tracking ARs for the 2003 ROS Event (Oct 5). This figure shows the MSLP procedure, with overlaid PWAT (top image), and corresponding IVT procedure (bottom image) for Banks Island ROS event on October 5, 2003, at 12Z. For the second part of this ROS event, another round of drizzle occurred on October 8. The setup for this second round of precipitation began with another AR-like feature over the Pacific Ocean. It was slightly weaker than the AR from September 30 but still yielded a long fetch of IVT values of 800-1,000 kg m^{-1} s^{-1}. This AR also extended greater than 2,000 kilometers from southern Alaska to well west of 170° W longitude.

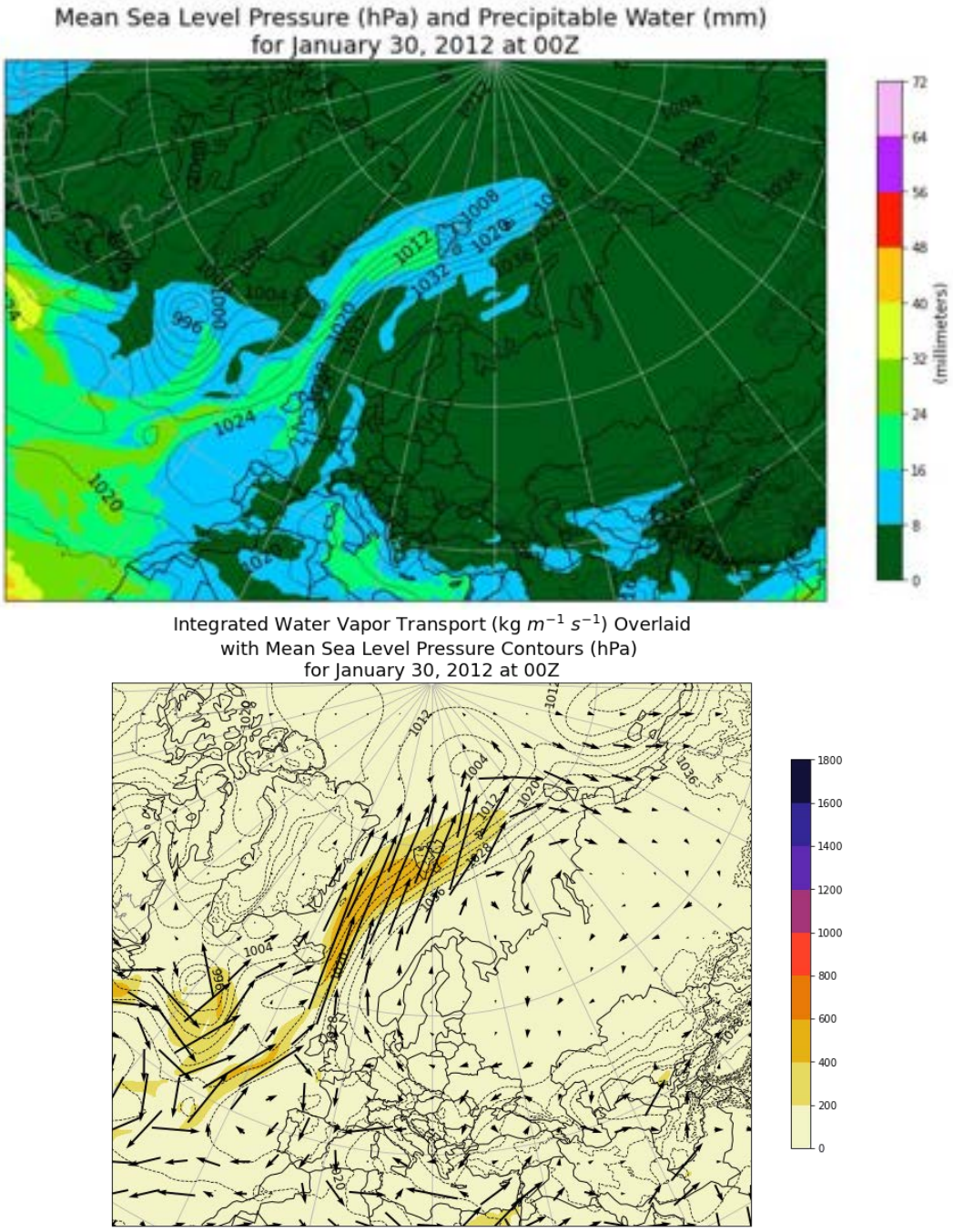

Figure 3.1.30: Tracking ARs for the 2012 ROS Event (Jan 30). This figure shows the MSLP procedure, with overlaid PWAT (top image), and corresponding IVT procedure (bottom image) for the Svalbard ROS event on January 30, 2012, at 00Z. An AR forming through the North Atlantic contributed to this ROS event directly. As the AR made landfall in Svalbard between January 29-30, IVT values in the range of 400-600 kg m^{-1} s^{-1} could be seen overhead of the archipelago. A long corridor of relatively high PWAT values began in an area west of northwestern Africa and extended directly north, well into the Arctic Ocean. This distance was greater than the 2,000 kilometers threshold identified in the literature.

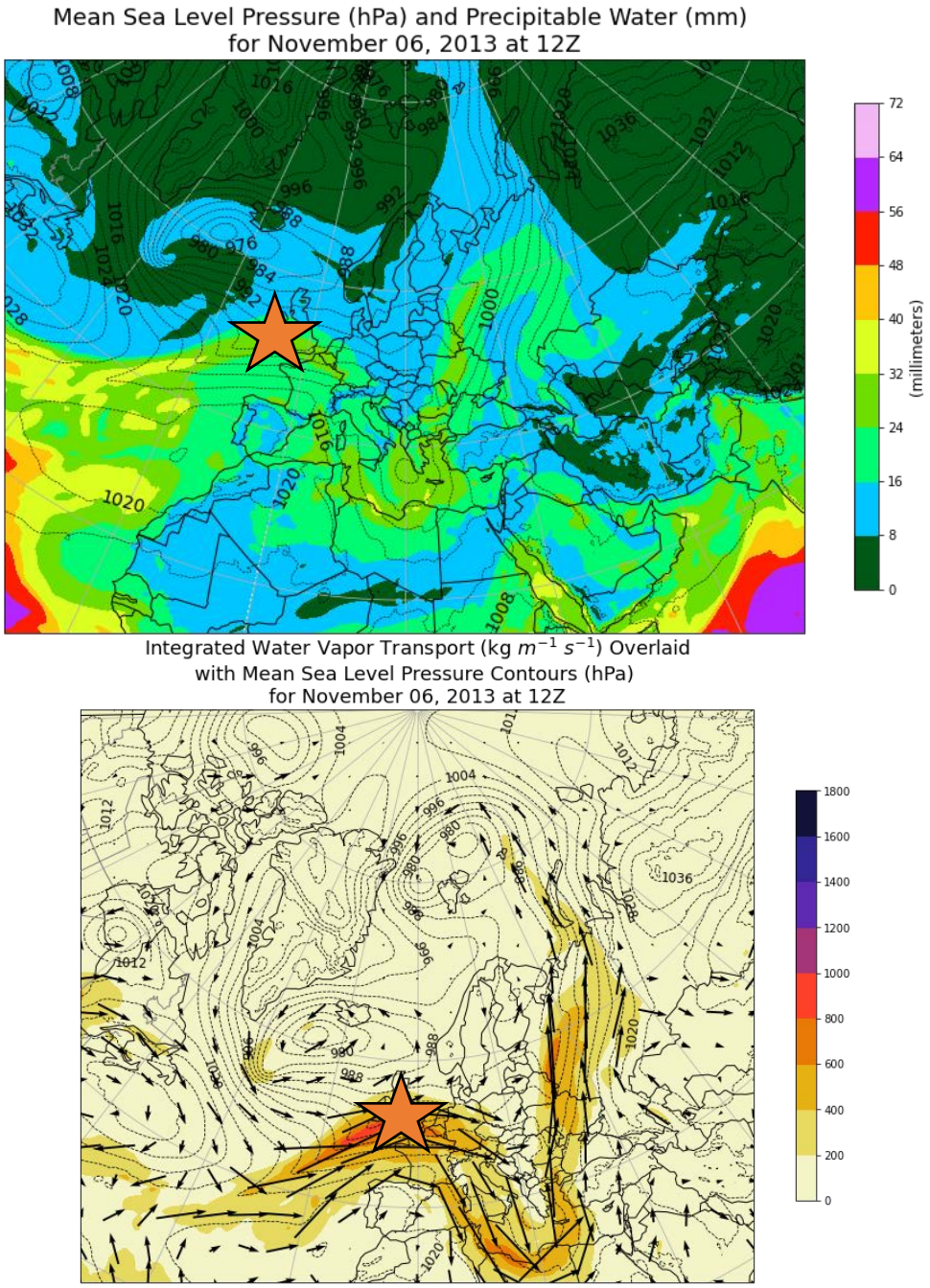

Figure 3.1.31: Tracking ARs for the 2013 ROS Event (Nov 6). This figure shows the MSLP procedure, with overlaid PWAT (top image), and corresponding IVT procedure (bottom image) for the Yamal Peninsula ROS event on November 6, 2013, at 12Z. The location lies away from the North Atlantic maritime influence, which was the source of a likely AR making landfall in western Europe (orange star). However, moisture from this feature managed to traverse much of Europe and add moisture to this ROS case with the help of a shortwave over eastern Europe and a deeper cyclone moving north of Svalbard. The AR over the North Atlantic led to indirect impacts over the Yamal Peninsula during the ROS event from November 8-10. Figure 3.1.25 shows that IVT values were in the range of 400-600 kg m^{-1} s^{-1} this far into northern Siberia, but the long fetch of high IVT seen in this image was not as solid by November 7. The 2,000 kilometers threshold was met with the AR in the Atlantic, if the distance from the star is measured and followed from the moisture plume west, southwest into the central Atlantic Ocean.

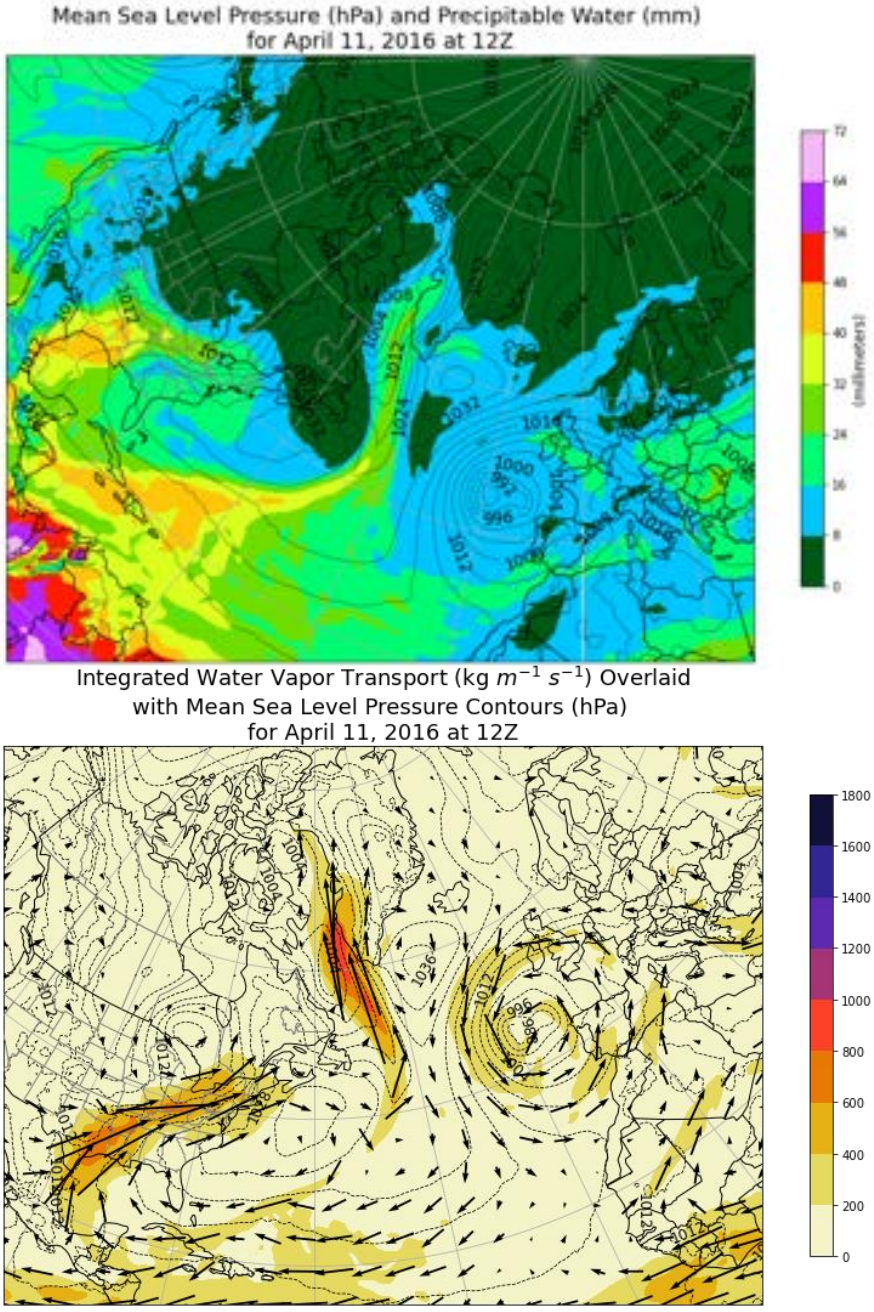

Figure 3.1.32: Tracking ARs for the 2016 ROS Event (April 11). This figure shows the MSLP procedure, with overlaid PWAT (top image), and corresponding IVT procedure (bottom image) for the Western Greenland ROS event on April 11, 2016, at 12Z. As seen previously with this case, the moisture and temperature variables were significantly higher for this ROS event. An AR from Baffin Bay extended south into the central Atlantic and picked up moisture from the Caribbean (a subtropical location), as evidenced by the PWAT chart at the top. Maximum IVT values between 800 and 1,000 kg m^{-1} s^{-1} even skirted the southwest coastline of Greenland. The 2,000-kilometer threshold was also met (with over 400 kg m^{-1} s^{-1} IVT extending from the Arctic Circle south to near 47 °N), and it was another case of an AR directly influencing this ROS event that occurred in Western Greenland.

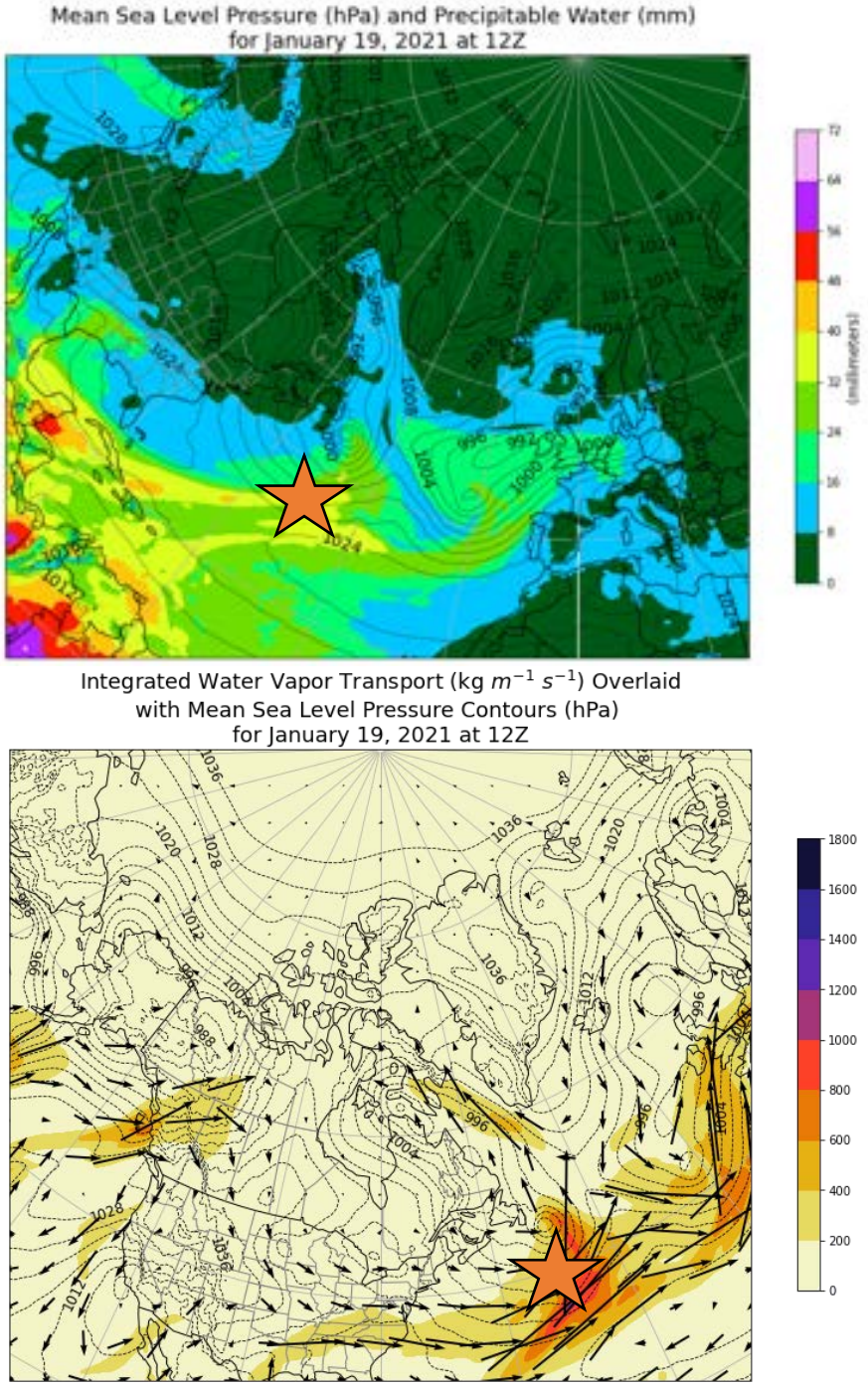

Figure 3.1.33: Tracking ARs for the 2021 ROS Event (Jan 19). This figure shows the MSLP procedure, with overlaid PWAT (top image), and corresponding IVT procedure (bottom image) for the Iqaluit, Canada, ROS event on January 19, 2021, at 12Z. This case represented the third incidence of an AR leading to indirect impacts on a ROS event. With the two images here, there was an AR-like feature east of the US eastern seaboard, traveling east, northeast into the North Atlantic. Maximum IVT values between 800 and 1,000 kg m^{-1} s^{-1} were in this corridor. A shortwave centered near Hudson Bay traveled north in the previous day, bringing with it a piece of this enhanced moisture. In the PWAT procedure, the main moisture column was being pulled from the Caribbean in this case as well. If the distance is measured from this moisture plume around 40° N and 40° W, this meets the 2,000-kilometer threshold.

As seen from the figures, ARs contributed to all of the studied ROS events. However, some cases exhibited indirect impacts through AR driven moisture being stripped off and moving with progressive shortwave troughs to the ROS locations. Section 1.3 discussed the ability for blocking patterns to act as precursors to ARs, which was referenced in the study from Benedict, Clement, and Medeiros (2019). This was the situation in potentially three of the five cases, with the blocking pattern playing an active role in the formation or strengthening of ARs. The cases from Banks Island, Canada (which displayed a wavy pattern overall across the Northern Hemisphere); Svalbard, Norway; and Western Greenland exemplify this coordination. However, in the cases for the Yamal Peninsula in Russia and Iqaluit, Canada, the ARs formed from other synoptic features driving the enhanced moisture transport, and shortwaves carried a pocket of this increased moisture to the locations of interest. In answering the second research question posed in this study, it appears that blocking patterns directly lead to AR formation but only in specific circumstances.

3.2: Important Differences Between ROS Events

Although similarities in the meteorology among ROS events have been established, there are also important differences. While blocks and blocking patterns represent a key causal mechanism in all cases, the blocks display a variety of synoptic setups – like Omega vs. Rex Blocks – and transitional phases. Similarly, the strength of the subsequent warm nose and moisture plume, relating to the depth and height of these phenomena, may range from smaller to larger effects and areas. ARs were discussed as having both direct and indirect impacts, so that is now analyzed further, in addition to other noted differences.

3.2.1: Case Study 1 – Banks Island, Canada (October 2003)

3.2.1.1: Case Background

The oldest case study with this research is the ROS event that occurred on Banks Island, Canada, in early October of 2003. Banks Island is part of the Canadian Arctic Archipelago, and its climate is shaped by both cryospheric and oceanic influences. Sea ice remains (in some form or another) year-round across much of the Canadian Arctic Archipelago, and the Arctic and Atlantic Oceans affect overall atmospheric circulations and consequent periods of precipitation (Melling 2002). The Canadian Arctic Archipelago, especially locations lying in the far north, fits the description of a “polar desert” and receives some of the lowest precipitation amounts for the Arctic (Serreze and Hurst 2000; Serreze and Barry 2014). Annual precipitation in this region usually falls within the range of 100-300 millimeters (approximately 4-12 inches), and cyclone activity typically peaks during the summer months (Serreze and Hurst 2000; Serreze and Barry 2014). Additionally, ROS events that happen over parts of the Canadian Arctic Archipelago typically emerge in the early part of autumn, since temperatures remain above freezing (Serreze et al. 2021).

The Banks Island ROS event was originally identified through observations and eyewitness accounts, the use of remote sensing methodologies, and documented impacts. This event led to the death of approximately 20,000 musk oxen (Grenfell and Putkonen 2008; Rennert et al. 2009). The rain resulting from the complex atmospheric conditions breached the underlying snowpack and froze at its base, forming a glaze of ice that made foraging for food difficult for these animals (Grenfell and Putkonen 2008). In addition, hunters reported that musk oxen were wandering out onto the pack ice in

search of other food sources and, consequently, drifted out to sea (Rennert et al. 2009). A survey in the following summer supported the conclusion that a large die-off event occurred among the musk oxen (Rennert et al. 2009).

Grenfell and Putkonen (2008) also describe their methodology in using passive microwave satellite sensors to examine alterations in the snowpack. Since these sensors are designed to detect emitted microwave radiation, they are helpful in gathering data, despite cloud cover and polar darkness. The study from Grenfell and Putkonen (2008) utilized these sensors to detect changes in brightness temperature at the surface, which alters when liquid water is present on the snow layer. Another study reinforced the value of this methodology in detecting ROS events (across Alaska in this case) when compared against station observations (Pan et al. 2018).

Researchers have also utilized station observations with this ROS event. Grenfell and Putkonen (2008) employed the Atmospheric Environment Service of Canada's station at Sachs Harbor, which lies on the southwest end of the island, 30-40 kilometers away from the ROS location. Only a trace of rain was reported there, but the air temperature recorded at the station provided a representative look at seasonal changes that led up to, and included, the ROS event (Grenfell and Putkonen 2008). They were also able to compare the meteorological data from the Sachs Harbor station to the satellite observations that detected a liquid layer coinciding with the timing of the ROS event in October 2003.

Rennert et al. (2009) examined some of the meteorological aspects of this event using a much older atmospheric reanalysis dataset – the National Centers for Environmental Prediction's (NCEP's) North American Regional Reanalysis (NARR).

They note that six inches of new snow had accumulated by early October, which preceded a period of on-again-off-again liquid precipitation. After the precipitation rounds subsided, temperatures fell, allowing a thick layer of ice to grow across 60 percent of the islands surface (Rennert et al. 2009). The ROS event followed a period of robust southwesterly flow caused by a ridge of high pressure that could be deduced from the 500-mb level (Rennert et al. 2009). Warmer, moister air was brought in with this flow, and this moisture was then lifted by a passing shortwave through “positive vorticity advection increasing with height” and the additional warm air advection (Rennert et al. 2009). The study also supplements additional details regarding the total precipitation accumulation experienced during the period of ROS:

> “For the 5-day period of 3-8 October during which the [ROS] events are estimated to have occurred, the amount of total precipitation (all forms) for Banks Island in the NARR is only 4 [millimeters],” (Rennert et al. 2009).

They also add that the Sachs Harbor station recorded 5 millimeters of precipitation during this same period. Based on these observations and climatological analysis conducted on ROS events, they concluded that ROS events occurring over Banks Island, including this event in October 2003, experience drizzle conditions, as opposed to accumulating liquid precipitation.

3.2.1.2: Differences in the Block and Upper-Level Wind Behavior

This case presented the most pronounced differences in the atmospheric setup compared to the other cases. One can already discern an Omega Block developing on September 30 that spanned all the way from Alaska to the eastern periphery of Canada. The axis of the anticyclonic ridge of the block extended south through western Canada,

across the Yukon Territory, and into the Alaskan panhandle. The ridge component in this case also covered a comparatively larger area than other cases. The overall block maintained the Omega setup through much of the first week of October. It then began to transition to a Rex Block, or Dipole Block, by October 5. Where an Omega Block looks like a capital Greek Omega symbol, the Rex Block is where either a trough strengthens or ridge weakens, allowing the trough to undercut the ridge. This leaves a pattern where the high-pressure (ridge) component positions over the low-pressure (trough) component. This is well represented by the 250-mb contours on October 6-7 in Figure 3.1.1 of subsection 3.1.1.

The Banks Island ROS case displayed a more prolonged period of ROS conditions. The position of the block in relation to the physical location of interest does not change much throughout the duration of the synoptic setup, leading to these persistent conditions. Southerly-component winds developed overhead of the Banks Island area during the period of ROS conditions identified by Rennert et al. (2009) from October 5 through October 8. However, the wind speeds were not as strong in the upper levels as in other ROS cases. Winds approached the 30-35 knot range out of the southwest at the 500-mb level leading up to the first reported ROS conditions on October 5 (Figure 3.2.1).

It can also be seen from Figure 3.2.1 that there was no strong jet streak, despite the southerly flow requirement being met. Consequently, jet dynamics (and subsequent lifting mechanisms) occurring with this case were different than what was seen in other cases. This strengthened the connection with the observations that showed that drizzle

occurred, as opposed to heavier, accumulating rain, that Rennert et al. (2009) allude to in their paper.

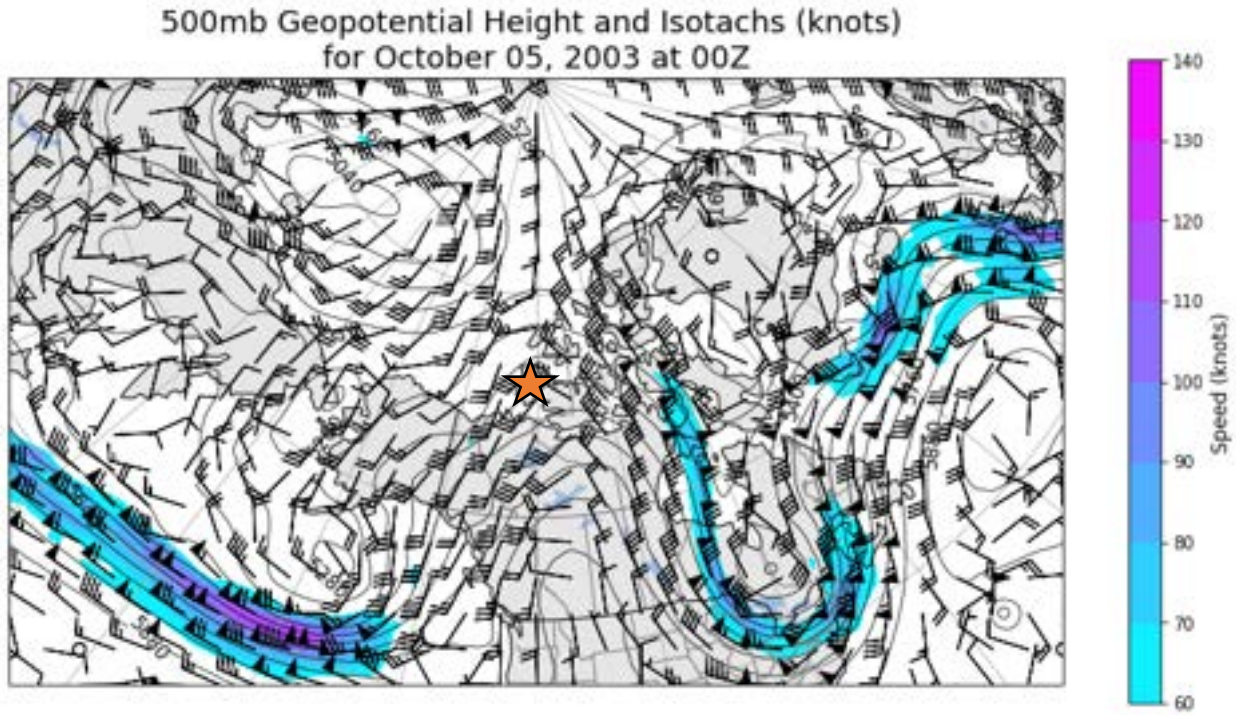

Figure 3.2.1: 500-mb Procedure (10/05/2003). The image includes 500-mb heights and winds, with wind speed realized as filled contours. Data are for October 5, 2003, at 00Z.

Additionally, a weak shortwave trough assisting in the initial round of drizzle conditions passed on October 5 and initiated strong northwesterly winds in its wake – generally around 50 knots – in the upper-levels above Banks Island. Figure 3.2.2 shows this action heading into October 6, 2003, at 00Z.

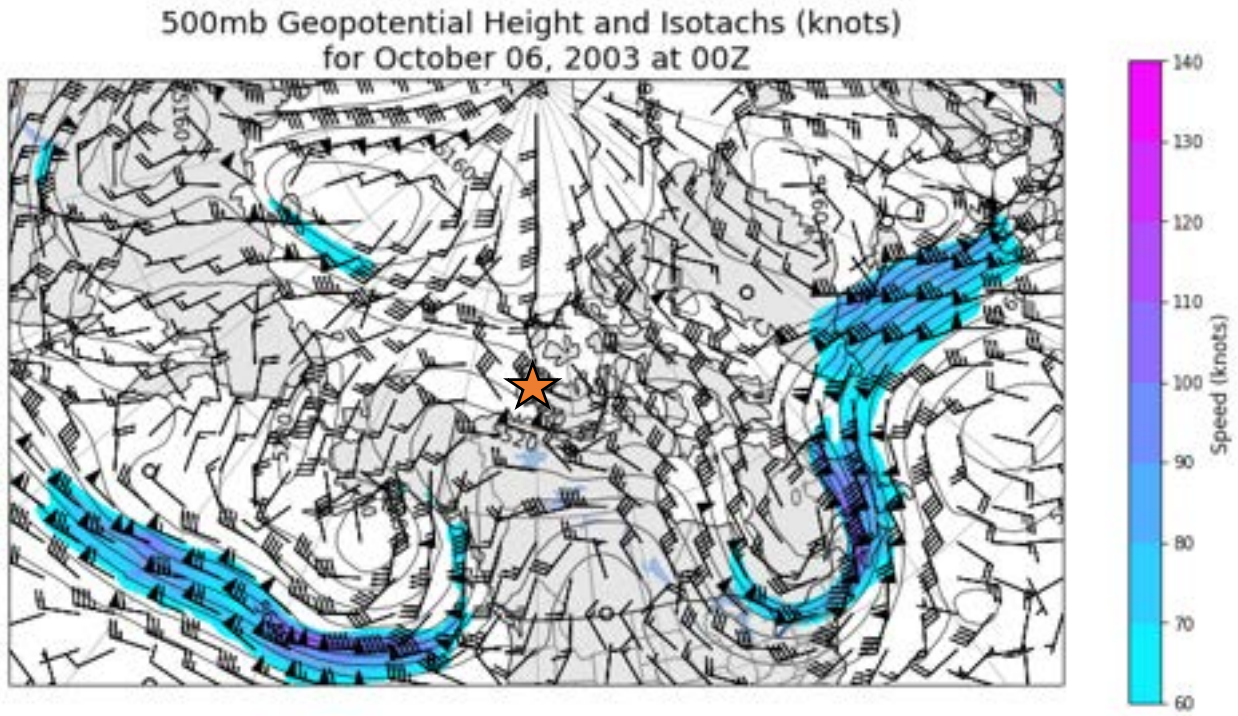

Figure 3.2.2: 500-mb Procedure (10/06/2003). The image includes 500-mb heights and winds, with wind speed realized as filled contours. Data are for October 6, 2003, at 00Z.

This shortwave system brought cooler, drier air briefly aloft across the area before southwesterlies resumed as the ridge built slowly east again. One sees this progression back to southwesterly winds aloft in Figure 3.2.3. Figure 3.2.3 also shows the setup leading up to the second round of drizzle conditions. For this date at the 500-mb level, the ridge axis was very nearly centered over Banks Island, but again, this was another setup lacking a jet streak aloft. Like the 500-mb procedure from October 5, the October 8 image instead displays a very strong jet streak over the Pacific Ocean, associated with a likely AR over this region.

Like the setup on October 5, this setup probably led to increased moisture riding up and over the ridge, known as a “dirty ridge” scenario. The National Weather Service describes a “dirty ridge” as a high pressure associated with a canopy of clouds that may form as a result of orography, a saturated boundary layer, or other lifting mechanisms –

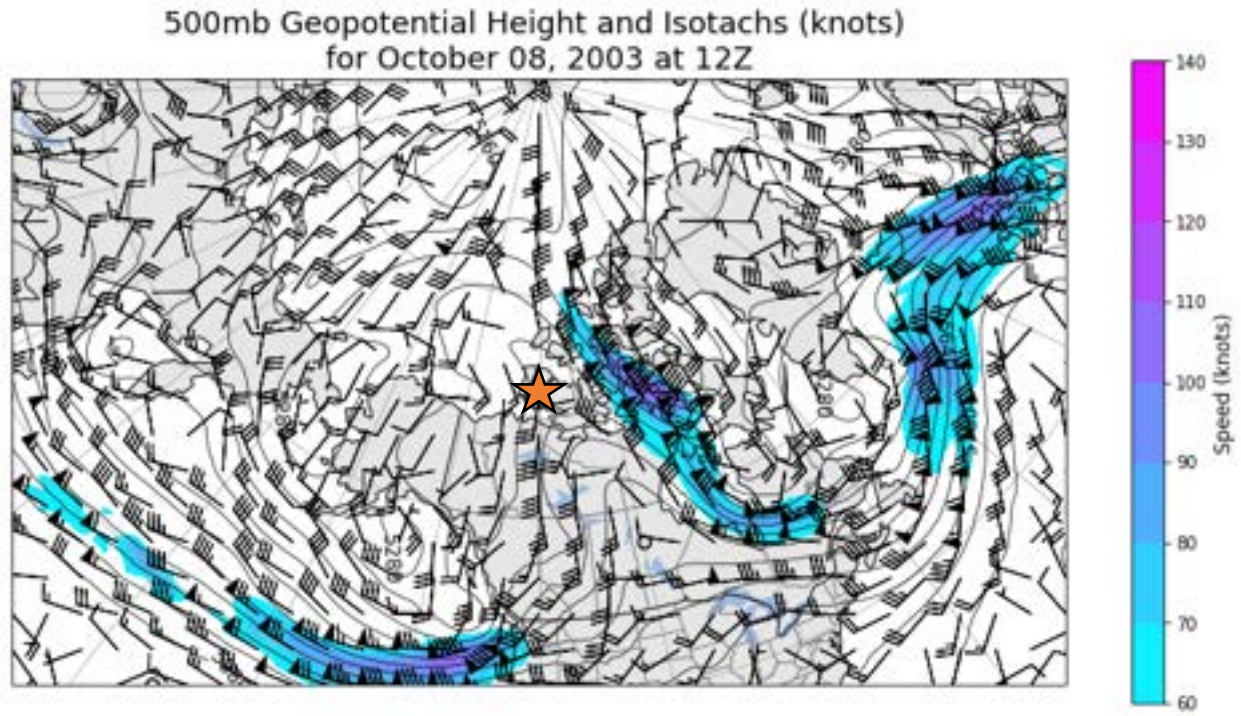

Figure 3.2.3: 500-mb Procedure (10/08/2003). The image includes 500-mb heights and winds, with wind speed realized as filled contours. Data are for October 8, 2003, at 12Z.

like warm air advection or moisture advection – which is the situation in this case (US Department of Commerce n.d.). One study documenting influences on freezing drizzle and rain noted that these precipitation conditions occur to the northeast of the cyclone, usually in the cold sector of stationary and warm fronts, when dealing with an Arctic high pressure scenario (Bernstein 2000). Another paper examining synoptic climatology associated with freezing precipitation noted that one of the patterns associated with freezing drizzle is the western quadrant of an Arctic high pressure system (Rauber et al. 2001). The authors describe the increasing gradient between a developing trough west of an Arctic high leading to strengthening southerly flow; this flow occurring in the upper levels indicates warm air advection through this zone that leads to a wide swath of cloud cover and precipitation (Rauber et al. 2001). Consequently, freezing precipitation initiates from this type of weather pattern and coincides with the area experiencing the

stronger southerly flow (Rauber et al. 2001).This appears to be the case here and also lends credibility to the report of drizzle conditions continuing.

3.2.1.3: Differences Among Other Key Atmospheric Components

While blocking patterns play the primary role in setting up ROS conditions over a particular area, it is important to understand the importance of smaller scale “warm noses” of higher temperatures, enhanced corridors of moisture transport, and the presence of LLJs. In the case of the Banks Island ROS event, these features diverged in strength and relative height in the atmosphere, when compared to other cases. While this was also noted in the atmospheric reanalysis data previously, one can also gain a further perspective from sounding data. The sounding data also provides a look at how the atmospheric column appeared at the time and evolved in terms of temperatures, moisture variables, and wind behavior alterations following the ROS event.

The soundings presented for this case were from Inuvik, which lies just south of Banks Island and is still located within the Northwest Territories of Canada but inland. The first sounding listed was taken on October 5 at 00Z (Figure 3.2.4). This sounding revealed a pronounced region of above freezing air temperatures that extended from the surface up to 800-mb, as previously seen in the ERA5 reanalysis. Winds were fairly

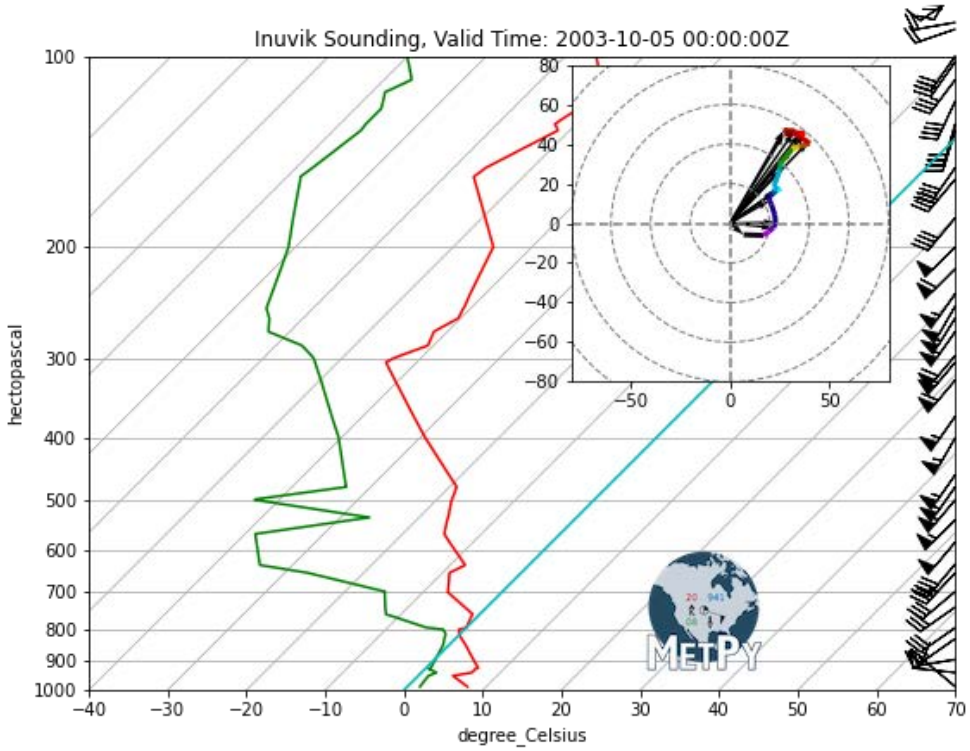

Figure 3.2.4: Inuvik Sounding for October 5, 2003, at 00Z. The red and green lines represent the temperature and dewpoint temperature, respectively, recorded with height.

brisk at 30-40 knots through the mid-levels, as is evident from the wind barbs on the right side and from the hodograph inset in Figure 3.2.4. The winds were also largely out of the southwest when rising above the surface. Additionally, PWAT calculated from the sounding resulted in a value of 12.28 millimeters. Compared to other cases in this study, this event provided slightly weaker winds with the LLJ, and despite moisture variables being high, they yielded lower values than other cases.

Figure 3.2.5 shows the atmospheric profile from the sounding taken 12 hours later. The shortwave has just passed near Banks Island, so the profile is different than the one taken 12 hours prior. The surface is now the only region sitting at freezing, with

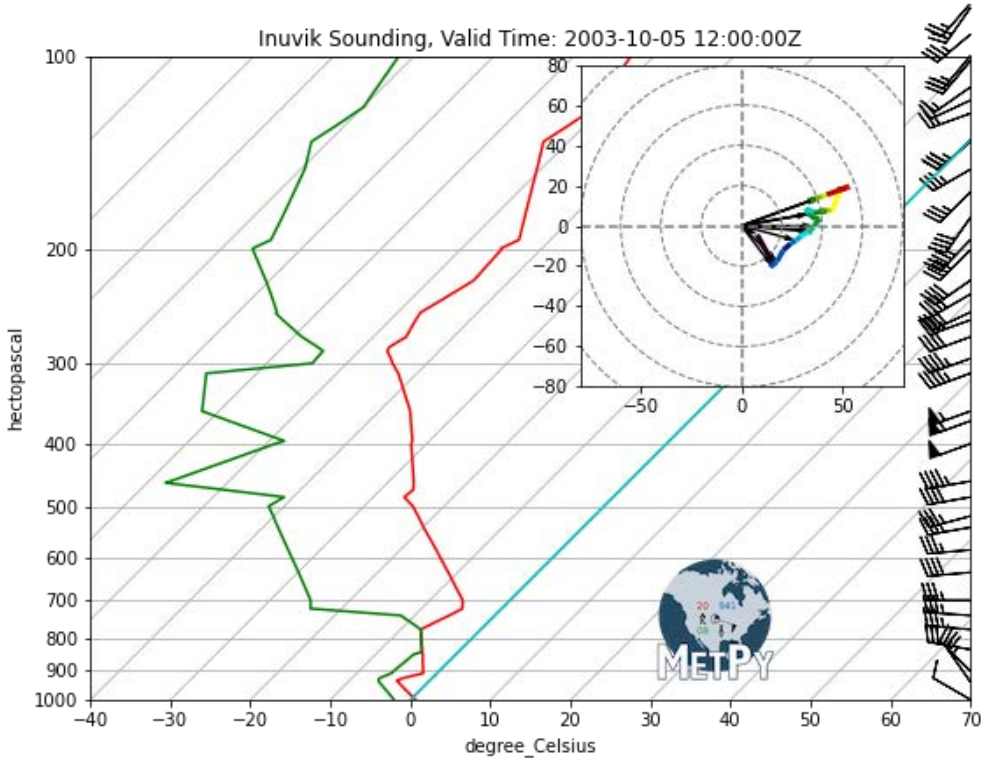

Figure 3.2.5: Inuvik Sounding for October 5, 2003, at 12Z. The red and green lines represent the temperature and dewpoint temperature, respectively, recorded with height.

the rest of the column temperatures now below freezing. Winds turned westerly, northwesterly near the surface, and there is some slight backing (winds turning counterclockwise with height), implying cold air advection occurring with the low-level winds. This sounding is also indicative of a freezing drizzle situation, where the moisture is confined to the lower levels, and mid-level dry air is present, with the surface just at freezing. This is yet another difference from the other cases.

Turning to the second round of ROS conditions on October 8, Figure 3.2.6 shows the sounding taken the late afternoon of that day for Inuvik. There was a weaker warm nose of above freezing or near freezing temperatures, extending from the surface to near 800-mb. Moisture amounts were like the October 5 data, yielding a PWAT of 12.63 millimeters. Winds were generally veering with height, so warm air advection was continuing. The winds were slightly different at this location (Inuvik), compared to the winds over Banks Island and assessed from the reanalysis. Similar characteristics to the previous sounding from the morning of October 5 implied further freezing drizzle conditions.

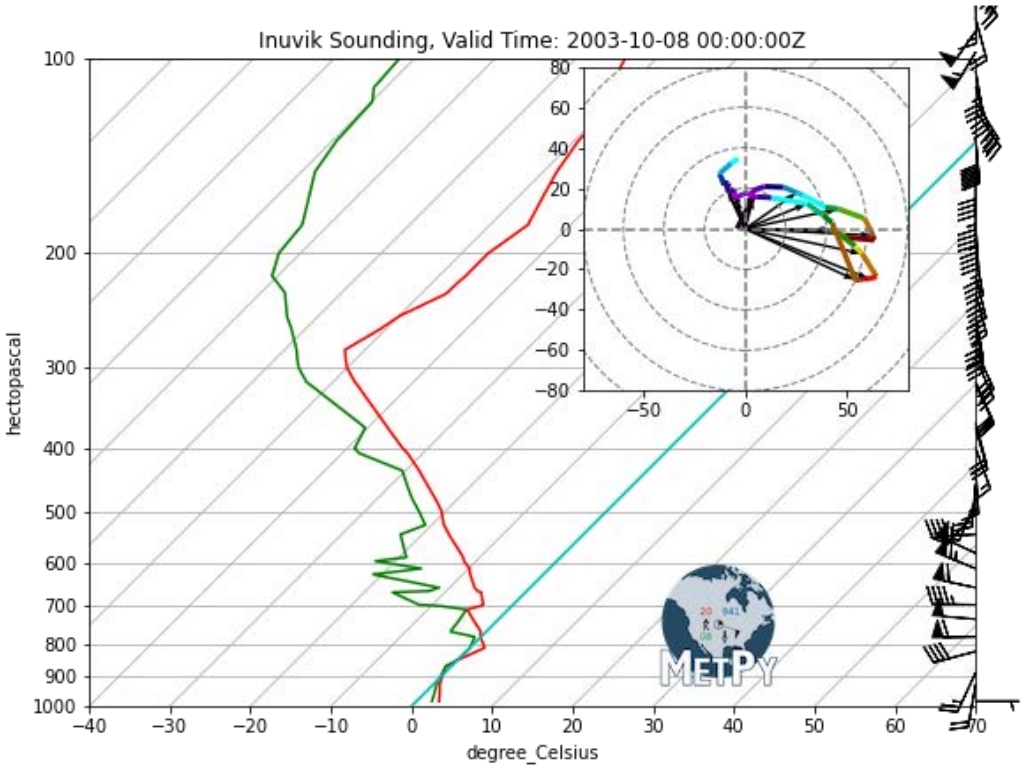

Figure 3.2.6: Inuvik Sounding for October 8, 2003, at 00Z. The red and green lines represent the temperature and dewpoint temperature, respectively, recorded with height.

The final sounding presented for this case was from October 10 at 12Z (Figure 3.2.7). A drier and colder air mass had overtaken the previous warm and moist air mass, as the ridge retrograded. This sounding yielded a PWAT value of 9.49 millimeters, still relatively high for this far north, but less than in the previous soundings. Additionally, the surface air temperature appeared to be below freezing, but a slight warm nose at the 900-mb level remained, with above-freezing conditions extending to

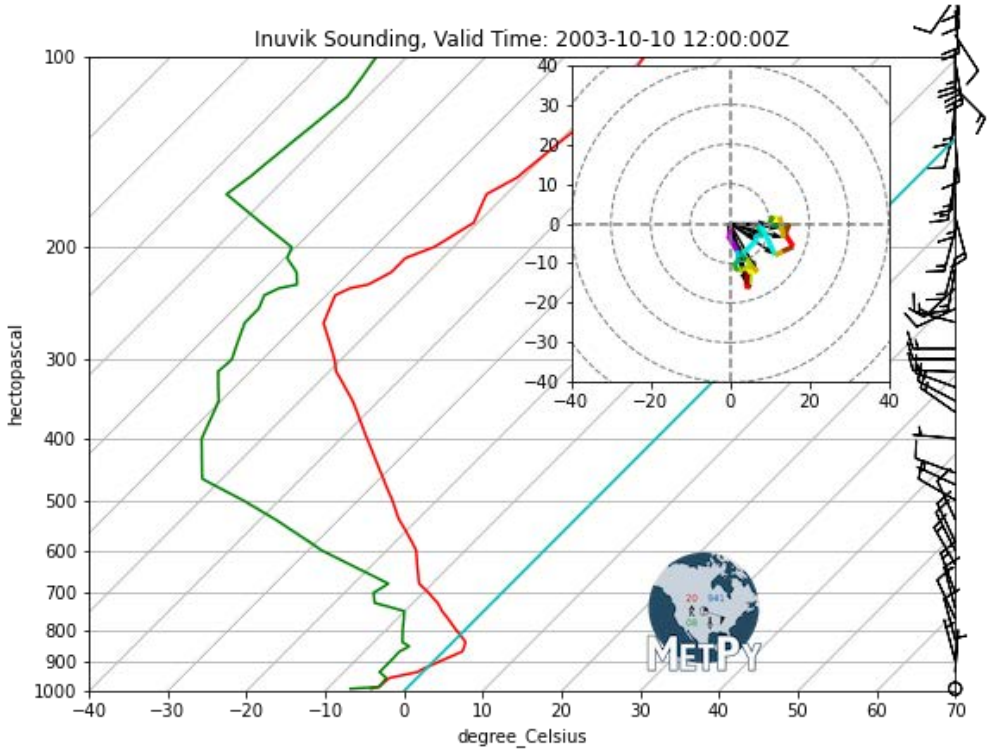

Figure 3.2.7: Inuvik Sounding for October 10, 2003, at 12Z. The red and green lines represent the temperature and dewpoint temperature, respectively, recorded with height.

around the 800-mb level, a large inversion. The wind behavior markedly changed as well throughout all levels of the atmosphere, with much lighter speeds and directions primarily out of the north, northwest that contributed to the changed air mass.

3.2.1.4: Level of Contribution from Atmospheric Rivers

Because of the multiple rounds of ROS conditions associated with this event, two time periods were chosen to conduct HYSPLIT analysis. Recall that these models all

deploy backward trajectories, using 96-hour timeframes, to gain an understanding of where the air mass may have originated. It also helps in confirming whether an AR directly or indirectly influenced a ROS event, which was mentioned briefly in Subsection 3.1.3. The first bout of precipitation for Banks Island began on October 5 due to moisture being pulled northeasterly across western Canada from an AR in the North Pacific (Subsection 3.1.3, Figure 3.1.22). This moisture transport stemmed from a deep cyclone over the North Pacific and a secondary cyclone over the Arctic Ocean.

From the HYSPLIT results presented in Figure 3.2.8, the air mass over Banks Island on October 5 came from the North Pacific, very near the Alaskan panhandle. The model was likely following the weak shortwave feature that led to precipitation on Banks

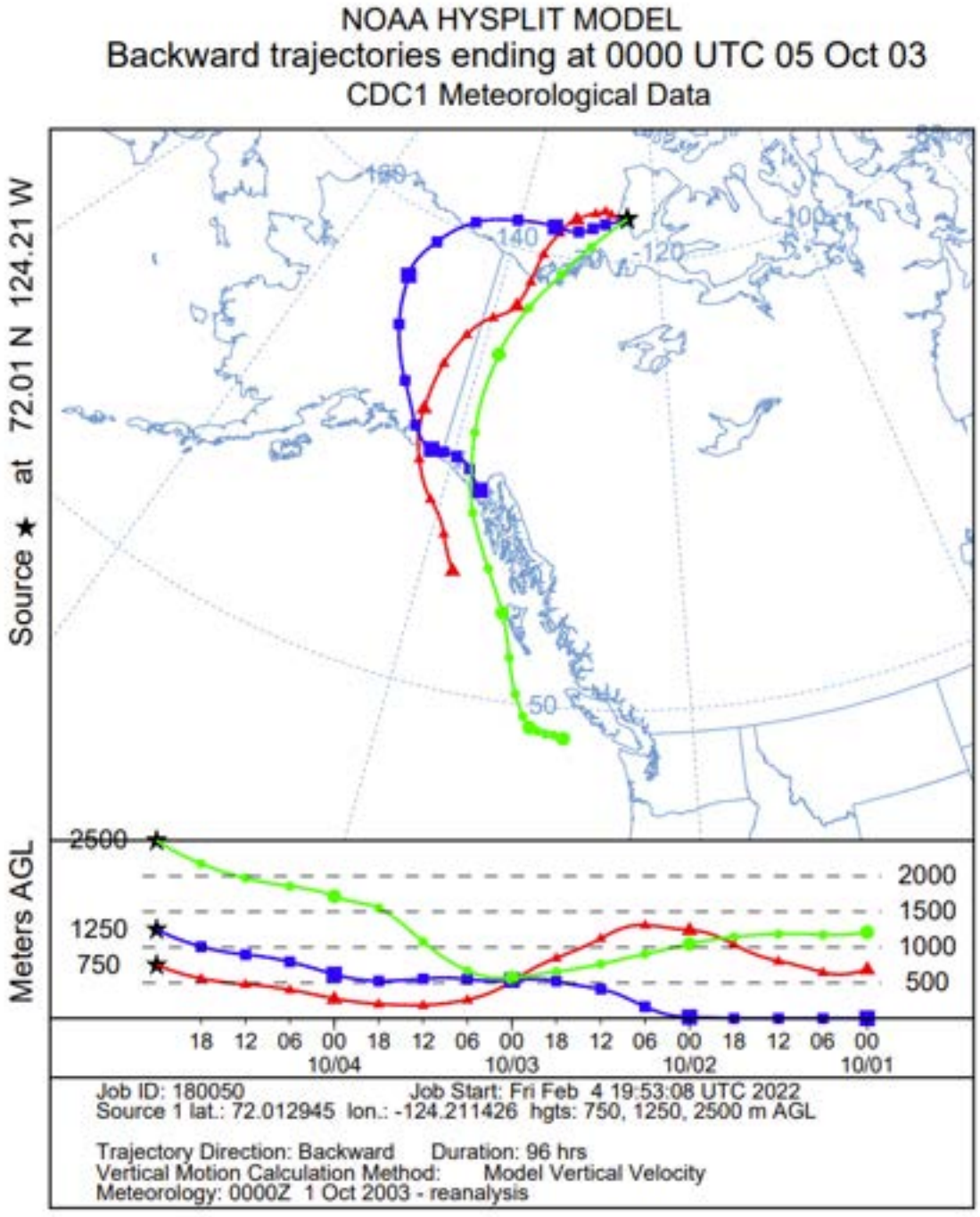

Figure 3.2.8: 2003 ROS Event HYSPLIT Results (Oct 5). This is the first HYSPLIT run for the Banks Island, Canada, ROS event from October 2003.

Island beginning on October 5. This also confirms that this was not a direct impact from an AR; moisture from this feature was likely transported north with this air mass, which is what the reanalysis demonstrated previously. Additional HYSPLIT results from October 8 (Figure 3.2.9) showed an even more unusual track, with the lower and middle heights (representing the 925-mb and 850-mb pressure levels, respectively) originating over the Arctic and taking unorthodox directions. This might be due to the influence of the overall ridge that drove much of this case. The higher height with this model run – equating to the 700-mb pressure level – was another instance of the air mass originating from the same location as the previous results from October 5. It is known that there was another AR present through the North Pacific at that time as well.

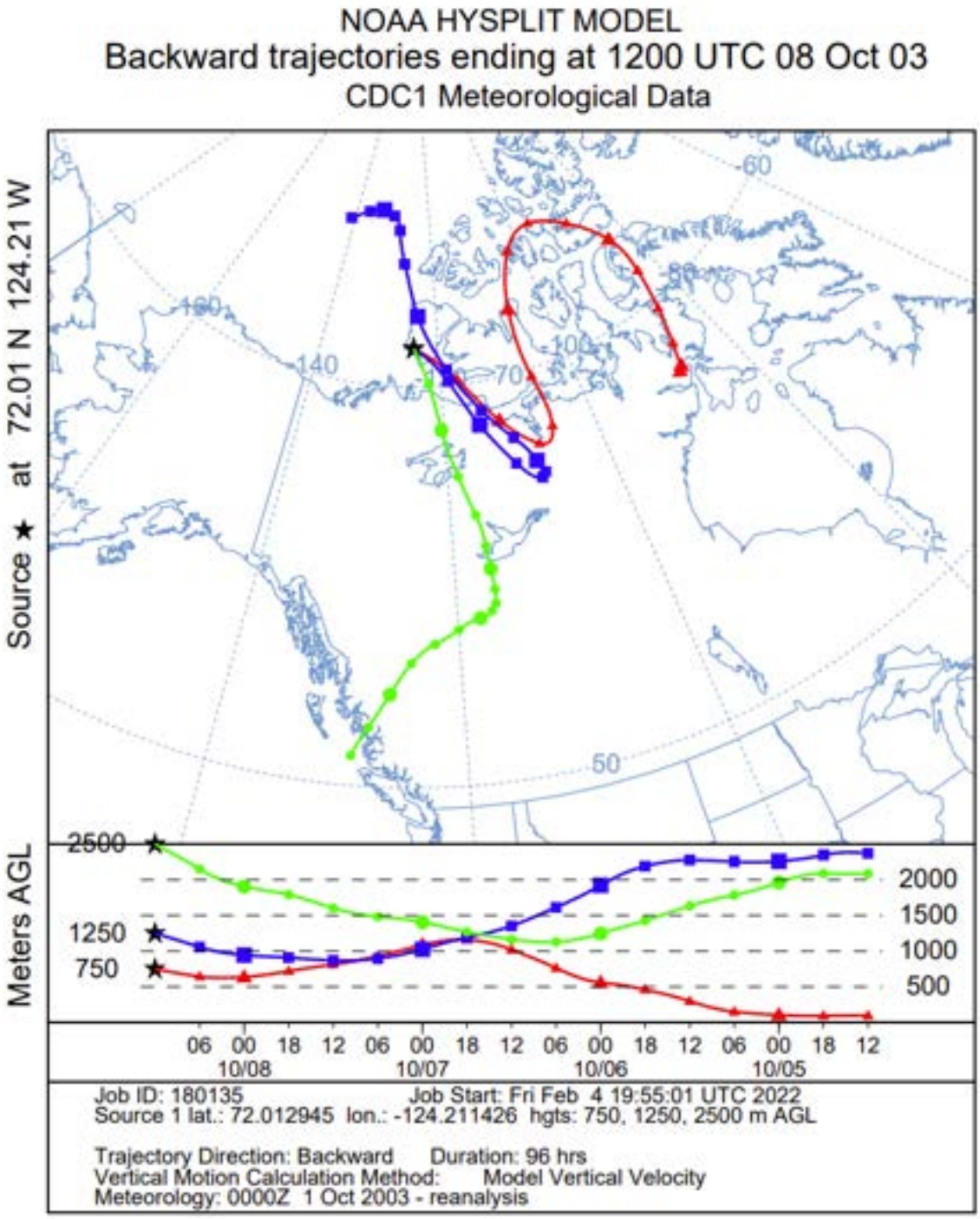

Figure 3.2.9: 2003 ROS Event HYSPLIT Results (Oct 8). This is the second HYSPLIT run for the Banks Island, Canada, ROS event from October 2003.

3.2.2: Case Study 2 – Svalbard, Norway (January 2012)

3.2.2.1: Case Background

Svalbard is an archipelago located north of Scandinavia and bordered by the Barents and Greenland Seas, between the North Atlantic Ocean to the south and the Arctic Ocean to the north. Svalbard has a maritime Arctic climate and is located in a part of the North Atlantic that witnesses strong, extratropical cyclone activity year-round but especially in winter (Serreze, Crawford, and Barrett 2015). During the winter months, air temperature gradients are at their strongest due to the contrast between the warm ocean water brought north due to ocean currents and the much colder air masses present over North America and the ice-covered Arctic Ocean (Serreze, Crawford, and Barrett 2015). This maintains a robust baroclinic zone, where consequent cyclones moving off the eastern seaboard of North America experience cyclogenesis and subsequent strengthening (Serreze, Crawford, and Barrett 2015).

Despite its maritime climate in terms of temperature, annual precipitation for the Svalbard Archipelago compares to totals found across the Canadian Arctic Archipelago, which were previously described as a “polar desert,” (Serreze, Crawford, and Barrett 2015). According to Serreze and Hurst (2000), much of the annual precipitation for the Svalbard Archipelago lies within the 300- and 400-millimeter range. Serreze, Crawford, and Barrett (2015) determined that station records for Ny Ålesund recorded an annual average precipitation of 423 mm (about 17 inches) for the 1979-2014 period of record. Interestingly, the Serreze et al. (2015) examination of extreme precipitation events for the Svalbard Archipelago argued that the largest precipitation event recorded for the

1979-2014 period for Ny Ålesund – 98 mm on January 30, 2012 – coincided with a major ROS event.

ROS conditions took place in Svalbard from January 30-31, 2012, and the impacts from this event ranged from a significantly warmed permafrost layer, a massive starvation event among the local reindeer population, and slush avalanches, which damaged infrastructure in the community of Longyearbyen (Hansen et al. 2014; Serreze, Crawford, and Barrett 2015; Serreze et al. 2021). Hansen et al. (2014) described the overall meteorological pattern consisting of a persistent ridge of high pressure over northern Scandinavia, which guided low pressure systems across the region of interest and included the increased transport north of warm, moist air. This aligns with the earlier conclusion that blocking patterns are key drivers of ROS events, with one of the important factors being their ability to direct multiple shortwaves to target a region. This overall synoptic pattern for the Svalbard ROS event led to a two week period – from January 26 to February 9 – of significantly higher temperatures than expected for this time of the year (Hansen et al. 2014; Serreze et al. 2021).

On the date of the highest recorded precipitation event (January 30), the progressive low-pressure systems that impacted Svalbard brought multiple rounds of precipitation. These systems combined with high PWAT anomalies and the anomalously high temperatures to produce this large rain event for the archipelago (Serreze et al. 2021). Additionally, Serreze, Crawford, and Barrett (2015) made the case that these characteristics exemplified an AR structure. Temperatures then began to fall after this warm spell, allowing the ice to accrete to the surface, with mostly all sampling sites documented in other research reporting 10-20 cm of ice (Hansen et al. 2014).

3.2.2.2: Differences in the Block and Upper-Level Wind Behaviors

Synoptically, this case presents a general wavy pattern overall across a quarter of the high latitude Northern Hemisphere when viewing the 250-mb procedure. The ROS event was led by the formation of a Wave Breaking blocking pattern (subsection 3.1.1, Figure 3.1.2), where the North Atlantic ridge begins to elongate between a broad trough over eastern Canada and Greenland and breaks over another through across much of Europe. These Wave Breaking Blocks are characterized by their direction of breaking and "the relative intensity of the air mass excursions," defined as usually cold or warm air masses (Masato, Hoskins, and Woollings 2013). Based on the authors' descriptions of these events, this Wave Breaking Block for the Svalbard ROS event would be classified as a cold anticyclonic type.

The top of the ridge neared Iceland by January 28, but the ridge then continued to push north between January 28-29. Iceland became favorable for ROS conditions during this period. At this point, Iceland fell into the gradient zone between the western-most trough and the overall ridge. Despite this case being an examination of Svalbard, further investigation of Reykjavik, Iceland, observations, lying well to the south, also reported ROS conditions (as seen in Figure 3.2.16 below).

The ridge continued its extension to the Svalbard archipelago between January 29 and 30. By January 30, the ridge stretched further over the North Atlantic, with Svalbard now in the ideal location for ROS conditions. An area of closed higher heights breaks off from the ridge's highest point and drifts over the Yamal Peninsula, forming a separate Rex Block over northern Russia. The Wave Breaking Block over the North Atlantic persists before the ridge appears to retrograde through the first week of

February. At this point, upper-level geopotential heights lower over the Svalbard archipelago, indicating a cooler, drier air mass beginning to encroach on this area.

Regarding the upper-level wind behavior, this case's location is the first one of four coinciding with a strong jet streak aloft (Figures 3.2.10 and 3.2.11). The previous Banks Island ROS event was the only one without a jet streak. Not only are there increased wind speeds with this jet streak, but the wind direction is also primarily from

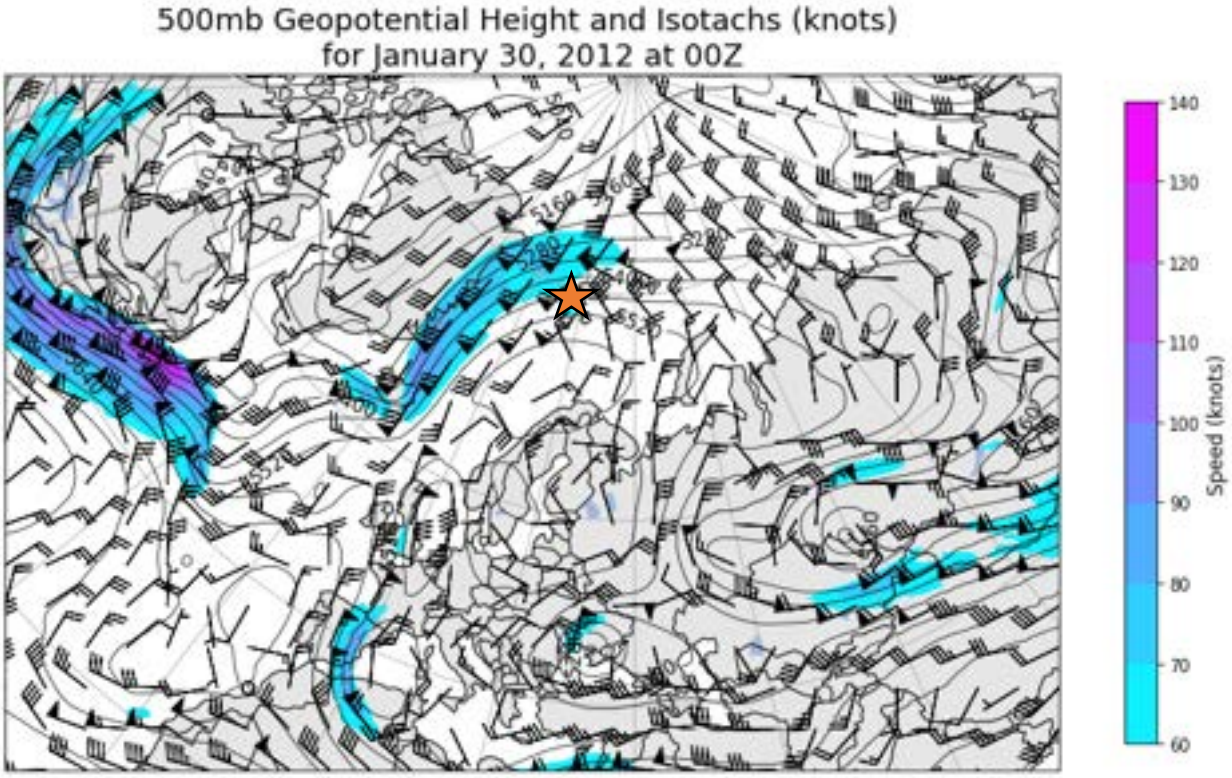

Figure 3.2.10: 500-mb Procedure (01/30/2012). The image includes 500-mb heights and winds, with wind speed realized as filled contours. Data are for January 30, 2012, at 00Z.

the south, southwest, maintaining the meridional flow. The 500-mb wind speeds in this area range from 50 to 80 knots, robust in the upper levels, and in line with the change in gradient between the ridge of the block and the western-most trough. Svalbard falls under the right entrance region of the jet streak on January 30 at 00Z (Figure 3.2.10). This implies convergence aloft and decreased lift available for precipitation.

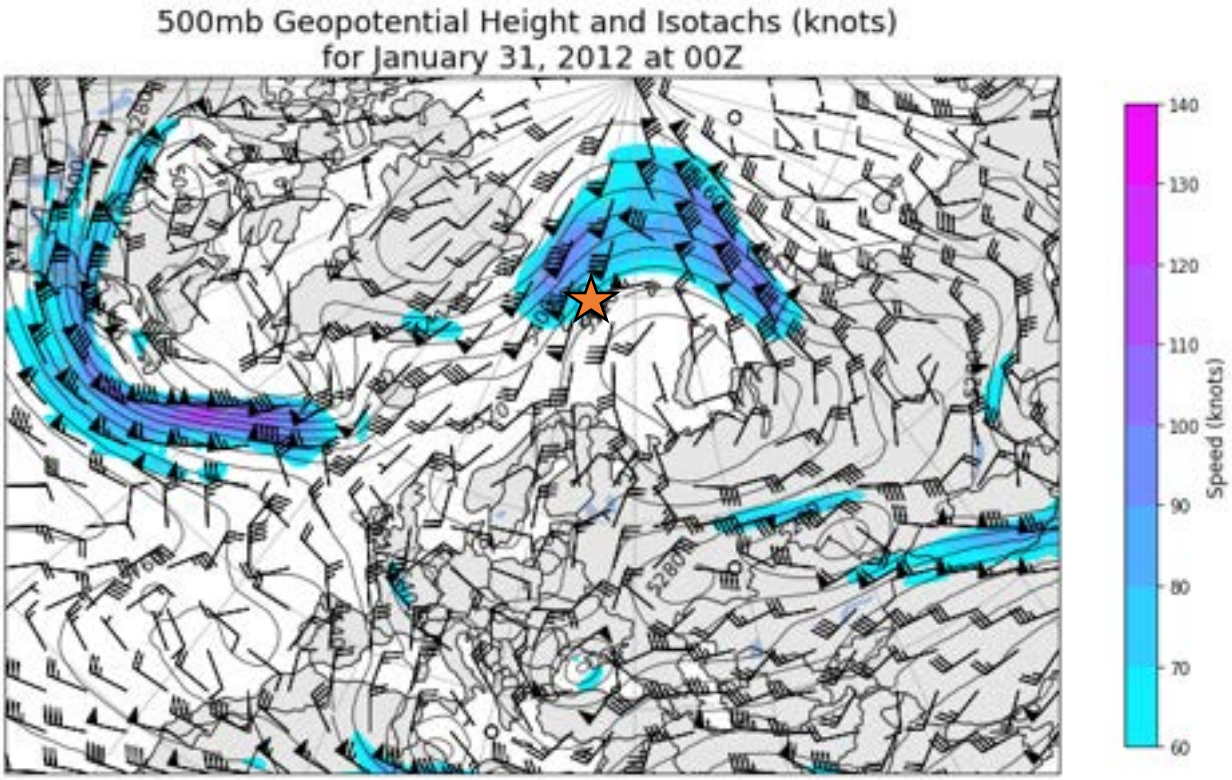

Figure 3.2.11: 500-mb Procedure (01/31/2012). The image includes 500-mb heights and winds, with wind speed realized as filled contours. Data are for January 31, 2012, at 00Z.

However, the jet streak became anticyclonically curved through the January 31 00Z time block (Figure 3.2.11). This then placed Svalbard in a position to experience divergence aloft. With this setup, divergence was favored with the left side of the ridge, west of the axis. Consequently, this favored more lift for greater precipitation. As the ridge weakened progressing into February, winds markedly lightened for all features at the 500-mb level (Figure 3.2.12).

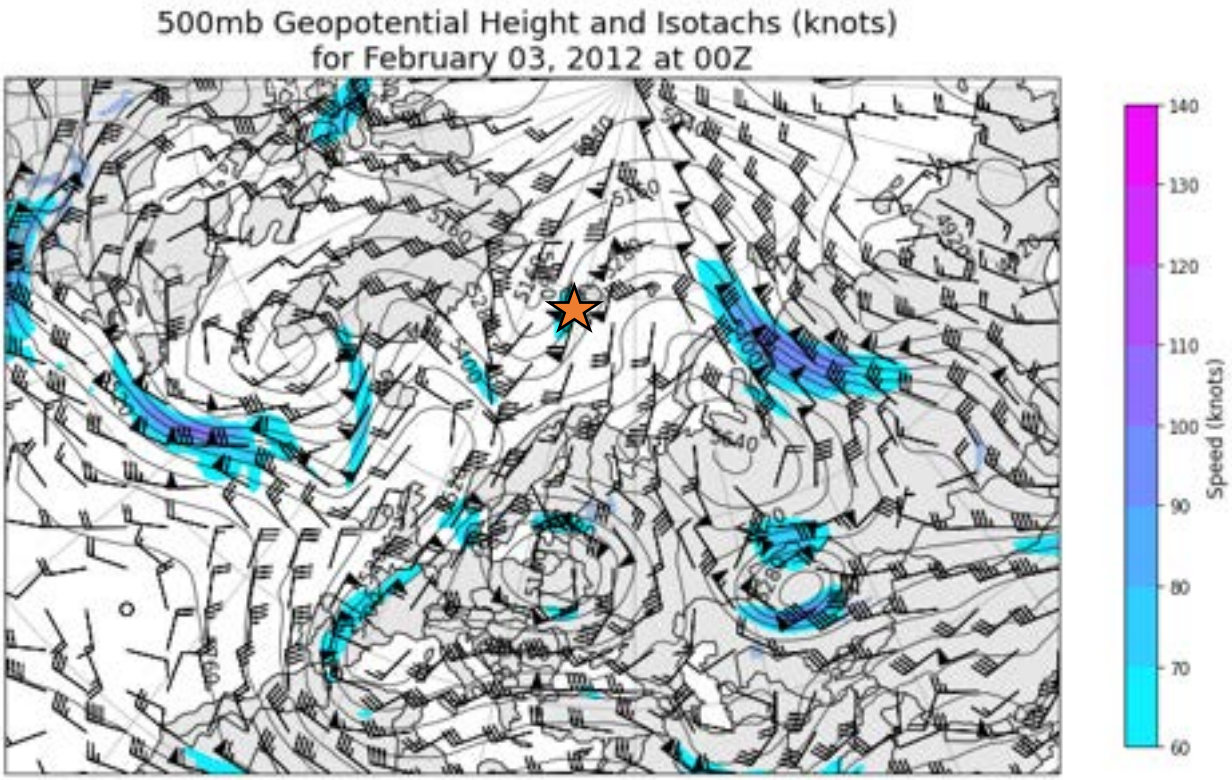

Figure 3.2.12: 500-mb Procedure (02/03/2012). The image includes 500-mb heights and winds, with wind speed realized as filled contours. Data are for February 3, 2012, at 00Z.

3.2.2.3: Differences Among Other Key Atmospheric Components

This case exhibited one of the shallower warm noses (Figure 3.2.13). The surface was above freezing by a few degrees. An inversion in place at about the 950-mb level separated the warm surface and the below freezing air above the 950-mb level. A relatively moist atmosphere produced a PWAT value of 13.57 millimeters, very significant at 78° N latitude and for January. A LLJ dominated from the 900-mb to the 700-mb level, with speeds of 40 to 60 knots. Winds were also out of the southwest, indicating warm, onshore flow. The hodograph displays additional evidence of warm air

advection with the veering (turning clockwise with height) winds through the middle levels of the atmospheric column.

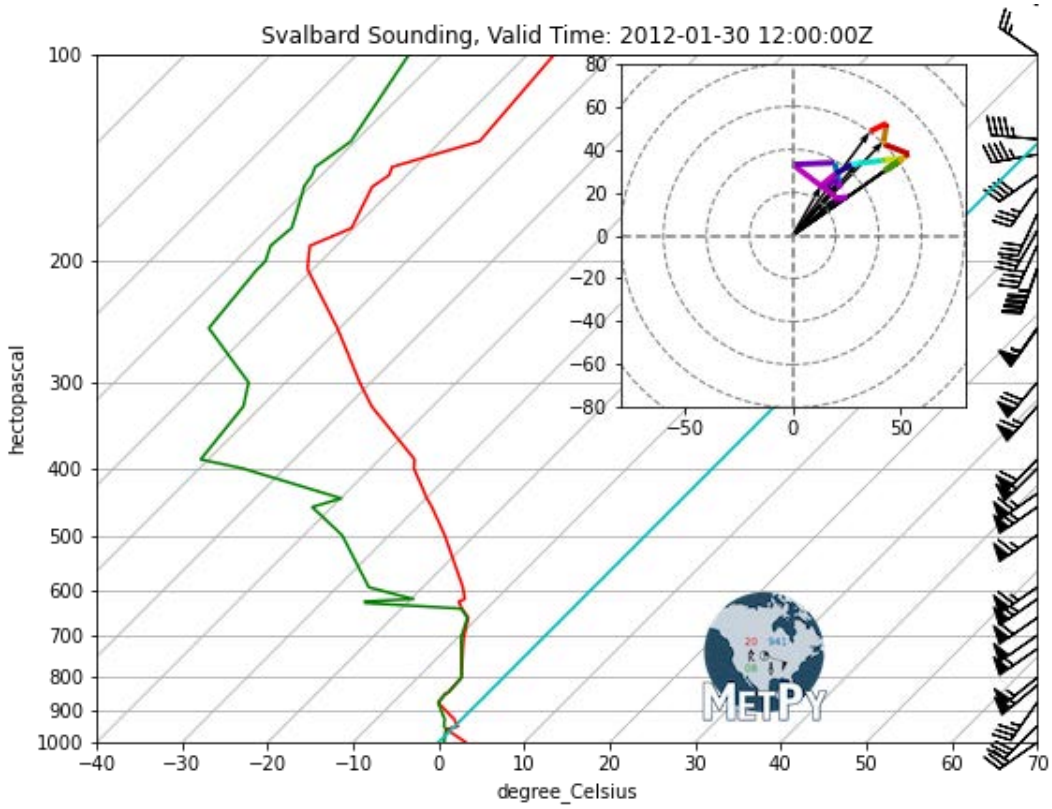

Figure 3.2.13: Ny Alesund Sounding for January 30, 2012, at 12Z. The red and green lines represent the temperature and dewpoint temperature, respectively, recorded with height.

The atmospheric profile changed dramatically in days following the ROS event. A much drier air mass was evident from the sounding derived PWAT value of 5.59 millimeters, represented in Figure 3.2.14. Winds were now largely out of the west, northwest – directing this cooler, drier air to Svalbard. Winds had also diminished throughout much of the column. Air temperatures were below freezing at all heights this weather balloon ascended through, exemplifying the new air mass that followed the warm and moist one required for the earlier ROS event.

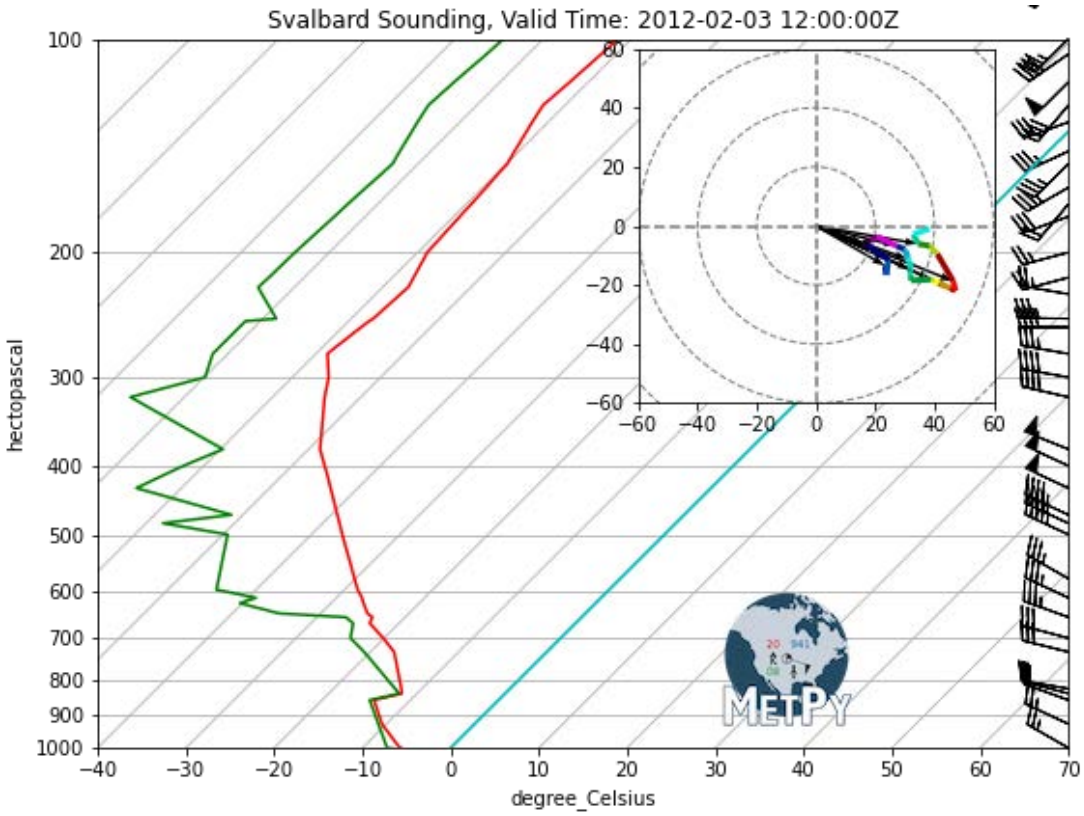

Figure 3.2.14: Ny Alesund Sounding for February 3, 2012, at 12Z. The red and green lines represent the temperature and dewpoint temperature, respectively, recorded with height.

Past studies discussed in Chapter 1 explained that air temperatures increase leading up to the eventual liquid precipitation or other types of mixed precipitation – such as freezing rain or a rain-snow mix – that then precede a period of falling temperatures. When station observations are available, they generally show these characteristics. The observations available at the Svalbard airport are revealing (Figure 3.2.15). Air temperatures rose, allowing precipitation to transition to liquid. As the system generating the precipitation moved on, temperatures fell to ranges typical for this time of year, and precipitation changed back to solid types. It is known from Figure 3.1.2, subsection 3.1.1, that lower heights were encroaching on Svalbard between

January 31 and February 1. With this colder air mass, one expected air temperatures to remain below freezing, except for some brief periods of above freezing conditions.

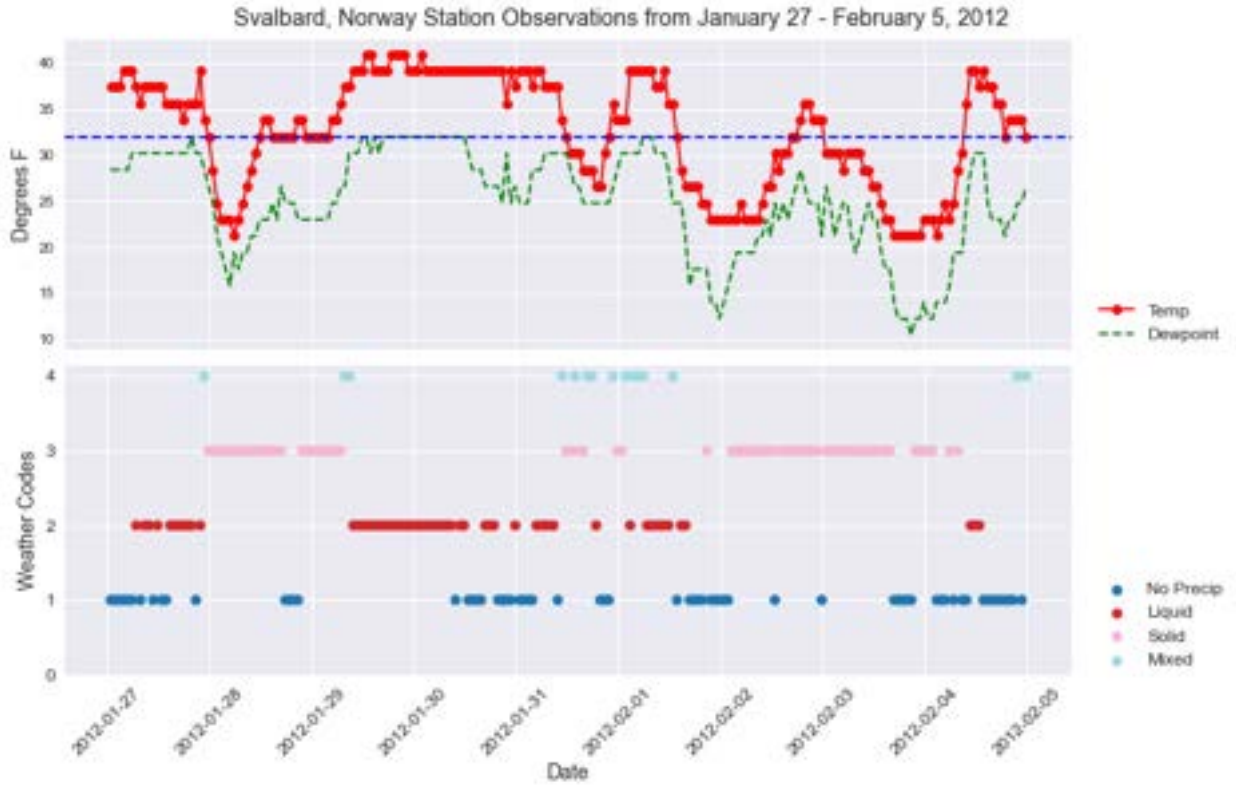

Figure 3.2.15: 2012 Svalbard ROS Event Observations. This image includes Svalbard station observations from January 27-February 5, 2012. Temperature and dewpoint temperature are plotted in the upper graph in °F, and the corresponding precipitation types are plotted in the bottom graph.

A supplemental observation set from Reykjavik in Iceland (Figure 3.2.16), which was also affected by this system, reiterates two key points regarding ROS events. First, it confirms similar conditions at the surface noted in previous studies. Air temperatures rose above freezing, leading up to some type of liquid precipitation event. Second, ROS conditions may be linked to an ideal position relative to the overall synoptic setup and (importantly) in relation to the blocking pattern. This ideal position was one that fell within the gradient between the ridge and western-most trough, where the strongest

southerly winds took place. This area then pivots to Svalbard a few days later, as evidenced in the observations there.

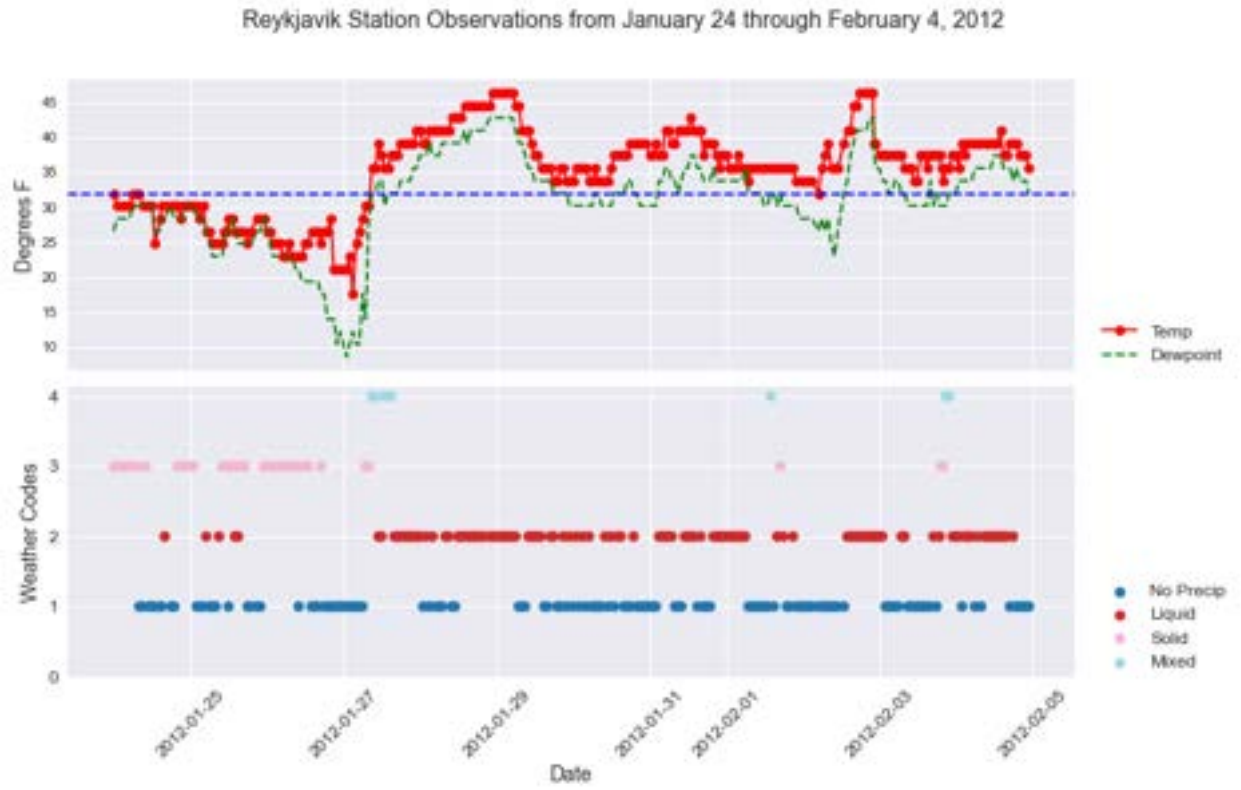

Figure 3.2.16: 2012 Reykjavik ROS Event Observations. Reykjavik, Iceland, station observations from January 24-February 4, 2012. Temperature and dewpoint temperature are plotted in the upper graph in °F, and the corresponding precipitation types are plotted in the bottom graph.

3.2.2.4: Level of Contribution from Atmospheric Rivers

The ROS event from Svalbard represents an example in which an AR directly played a role in the ROS conditions. Serreze et al. (2015) alluded to this in their paper but were unable to provide confirmation. The confirmation follows from Figure 3.1.30, showing high IVT through the North Atlantic and increased PWAT values beginning in the subtropics. Results from the HYSPLIT model (Figure 3.2.17) confirm this as well. A backward trajectory from Svalbard reveals that in the 96-hour period, the air mass – consistent with the 850-mb and 700-mb equivalent heights – originated at around 30° N latitude, southwest of Portugal and Spain. This demonstrates a subtropical source. The

lowest height, exemplified at the 925-mb equivalent level, originated a little further north; however, this would have also presented a warm and moist air mass. This case also

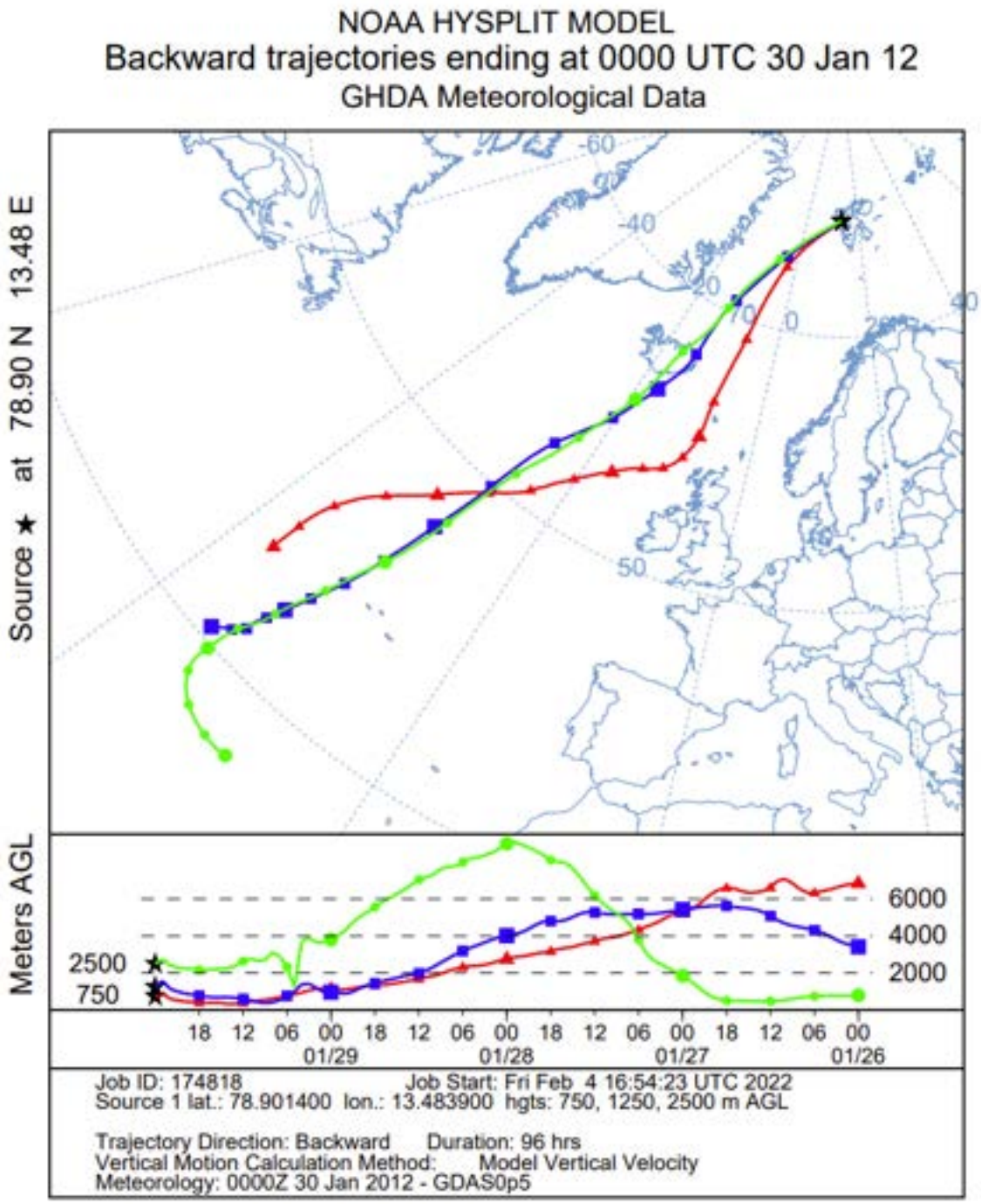

Figure 3.2.17: 2012 ROS Event HYSPLIT Results (Jan 30). This is the HYSPLIT run for the Svalbard, Norway, ROS event from January 2012.

represents one of two cases where the location of the ROS event was directly impacted by an AR.

3.2.3: Case Study 3 – Yamal Peninsula, Russia (November 2013)

3.2.3.1: Case Background

The Yamal Peninsula is part of the Yamal-Nenet Autonomous Okrug of northwest Siberia, Russia, and extends into the Kara Sea. According to Bruce C. Forbes:

> "This region is the homeland of the largest remaining nomadic pastoralist group active in the Arctic, the Yamal Nenets. The basis for this indigenous but somewhat modernized economy is the seasonal exploitation of extensive tundra 'pastures'," (Forbes 1999).

Low Arctic tundra characterizes much of the peninsula, and there is continuous permafrost throughout the region (Forbes 1999). Annual precipitation averages between 300-500 millimeters (approximately 12-20 inches) (Serreze and Hurst 2000). Decreasing sea ice concentration within the Kara Sea has likely influenced changes in the overall climate across the peninsula, including the occurrence of autumn and winter ROS events (Forbes et al. 2016).

Reindeer herders were strongly impacted by this ROS event that occurred from November 8-10, 2013, and it – in combination with unusually warm conditions continuing into the early part of 2014 – led to the starvation of approximately 61,000 animals (Forbes et al. 2016). Eyewitness accounts from herders point to the worst ROS conditions occurring on November 8-9, and remote sensing data document severe icing on November 10 (Forbes et al. 2016). Ice generated from this event covered an area of

about 27,000 km^2 that effectively blocked animals' access to their normal food source, causing them to starve (Forbes et al. 2016; Mark C. Serreze et al. 2021).

As for the associated meteorology, Forbes et al. (2016) and Serreze et al. (2021) provided some useful background. Remote sensing data showed anomalously high air temperatures and PWAT values across the region leading up to the event (beginning on November 6) and extending to November 9 (Forbes et al. 2016). Data from the ERA-Interim reanalysis showed large precipitation anomalies – in combination with winds moving in from out of the south – on November 6-7 (Forbes et al. 2016). Serreze et al. (2021) also linked ROS conditions to a passing low-pressure system that progressed into the Yamal Peninsula from the northern North Atlantic.

3.2.3.2: Differences in the Block and Upper-Level Wind Behavior

The Yamal Peninsula ROS event shares a similar setup with the Banks Island event from October 2003, in that an anticyclonic ridge was a dominating feature. However, with the Yamal Peninsula ROS event, the 250-mb geopotential height contours at the jet stream level (Subsection 3.1.1, Figure 3.1.3) demonstrated an Anticyclonic Wave Breaking Block, like the 2012 Svalbard ROS event, but characterized by a warm air mass excursion, rather than a cold one. Masato et al. (2013) associated a more progressive storm track with Warm Anticyclonic Wave breaking patterns, and these patterns typically exhibited a shorter duration than their cold counterparts. The authors added that they found only 47% of warm anticyclonic events that lasted longer than seven days, whereas 54% of the cold anticyclonic events lasted longer than seven days.

For this case, the ridge of high pressure extended across much of western Russia between an embedded shortwave system of a broad trough across the North Atlantic and another shortwave associated with an additional trough across central Russia. The ridge then proceeded to break over the eastern-most shortwave trough in central Russia on beginning on November 7. The peninsula was positioned beneath the area with the strongest gradient around this time, between the ridge and the embedded shortwave over northeast Europe, just like in other cases. As mentioned previously regarding similarities among cases, this location in relation to the overall block was optimally suited for experiencing ROS conditions due to the strong southerly flow and the resultant warm air mass moving into the region.

Another similarity discussed in the previous section, and detected among many of the cases, was the presence of a strong jet streak (Figure 3.2.18) above the location

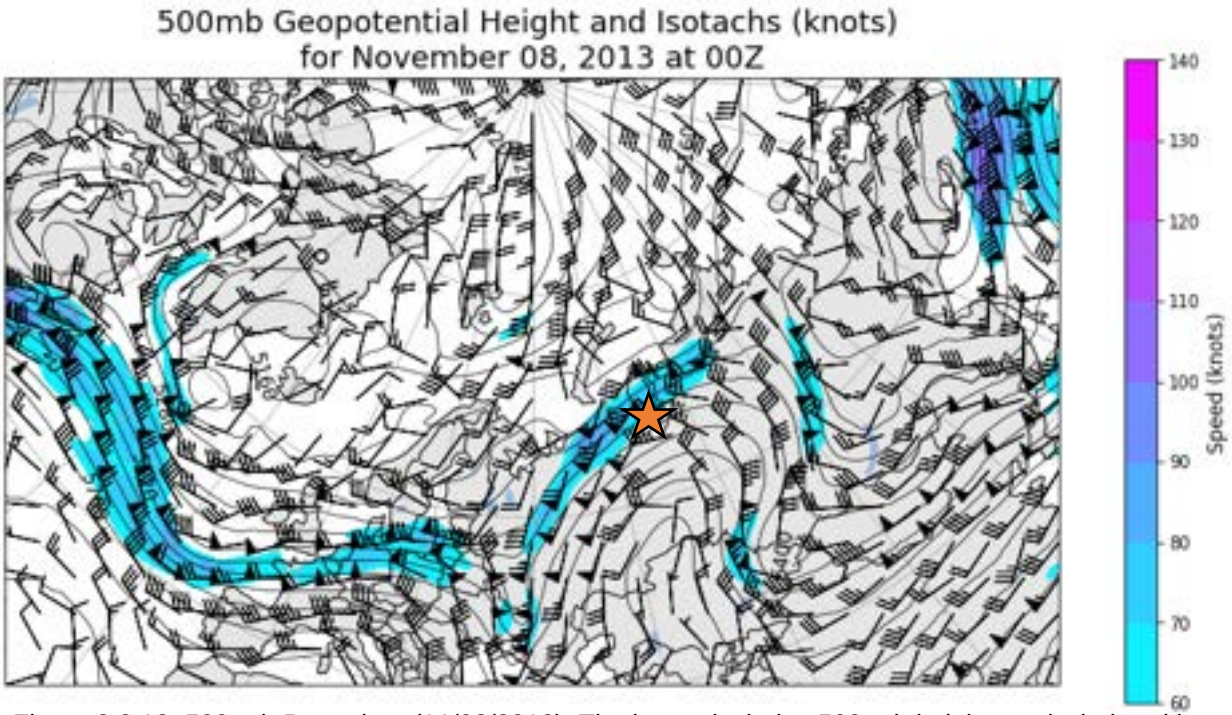

Figure 3.2.18: 500-mb Procedure (11/08/2013). The image includes 500-mb heights and winds, with wind speed realized as filled contours. Data are for November 8, 2013, at 00Z.

of interest. Additionally, it usually represents the sector with the strongest southerly winds on the upstream side of the ridge, west of the ridge axis. Figure 3.2.18 shows southwesterly winds throughout the corridor above the peninsula, and wind speeds range from 60 to 80 knots through this area. Jet dynamics likely also influenced precipitation over the peninsula, with the region briefly targeted within the left exit region of the jet and pointing to divergence aloft. This increased the upward vertical motion needed for precipitation. However, two differences in this case were the shorter duration of the overall block (Figure 3.2.19) – which only appears to persist for about four to five days – and that the block was associated with a more active storm track, as Masato et al. (2013) described of these blocking types.

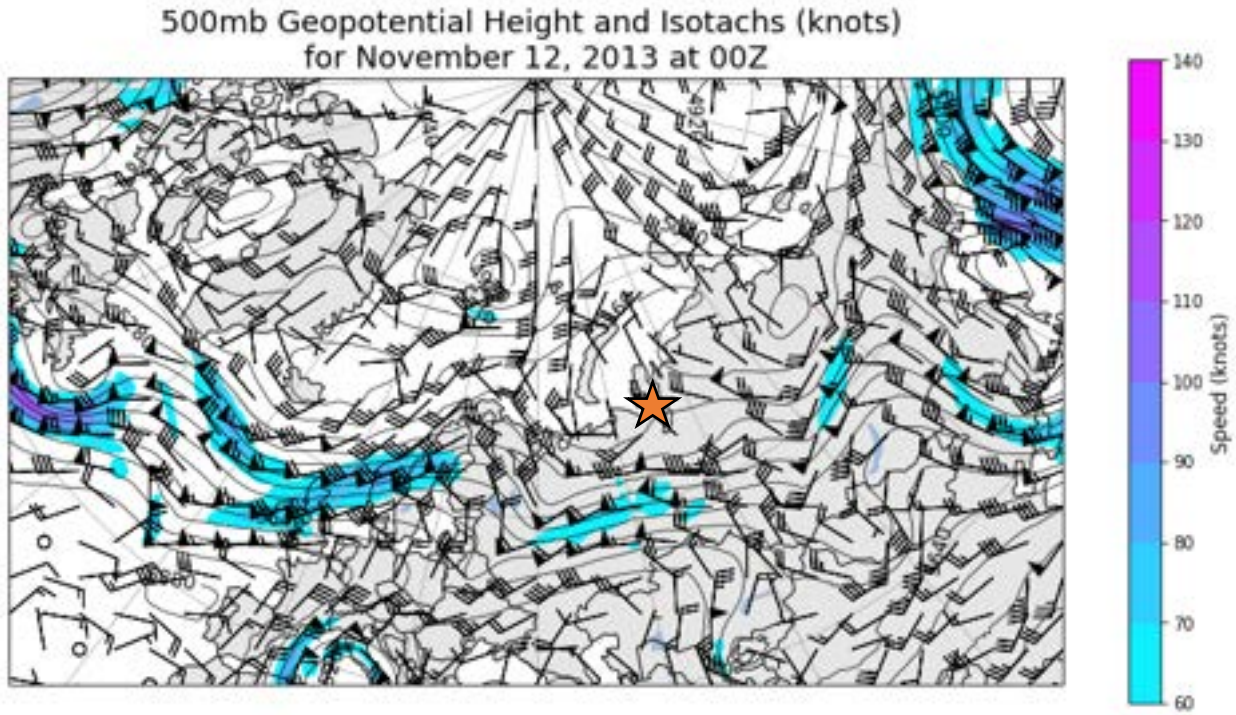

Figure 3.2.19: 500-mb Procedure (11/12/2013). The image includes 500-mb heights and winds, with wind speed realized as filled contours. Data are for November 12, 2013, at 00Z.

3.2.3.3: Differences Among Other Key Atmospheric Components

Unfortunately, no station records were available to assess for surface conditions, but the soundings from Salekhard linked well with the atmospheric reanalysis. From the upper air data on November 8 at 00Z (Figure 3.2.20), another distinct warm nose was seen extending from the surface to about the 800-mb level, with temperatures around 5

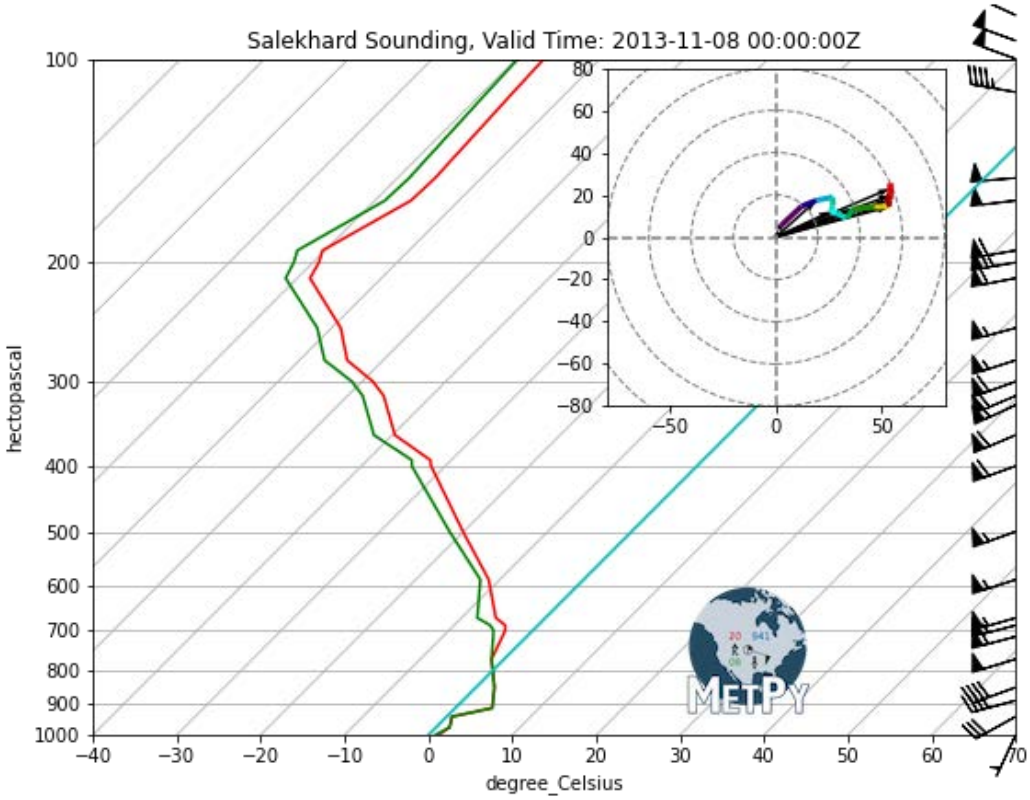

Figure 3.2.20: Salekhard Sounding for November 8, 2013, at 00Z. The red and green lines represent the temperature and dewpoint temperature, respectively, recorded with height.

°C at the 900-mb level. This verifies the data examined in the 925-mb and 850-mb procedures discussed in subsection 3.1.2, Figure 3.1.19. A LLJ of 40-50 knots can be seen from the 900-mb to the 700-mb level. The hodograph also displays the signature veering (turning clockwise) with height, meaning warm air advection with the southwesterly flow. A very large (for this latitude and time) PWAT value of 20.99 millimeters was calculated from this sounding.

In the few days following, a very different air mass replaced the one that led to the ROS conditions. The sounding from November 13 at 12Z (Figure 3.2.21) shows a noticeably colder and drier air mass. Like other cases, temperatures were below freezing to around -5 °C near the surface and further decreased upwards. The PWAT value with this sounding was 6.85 millimeters, a significant drop from the value on

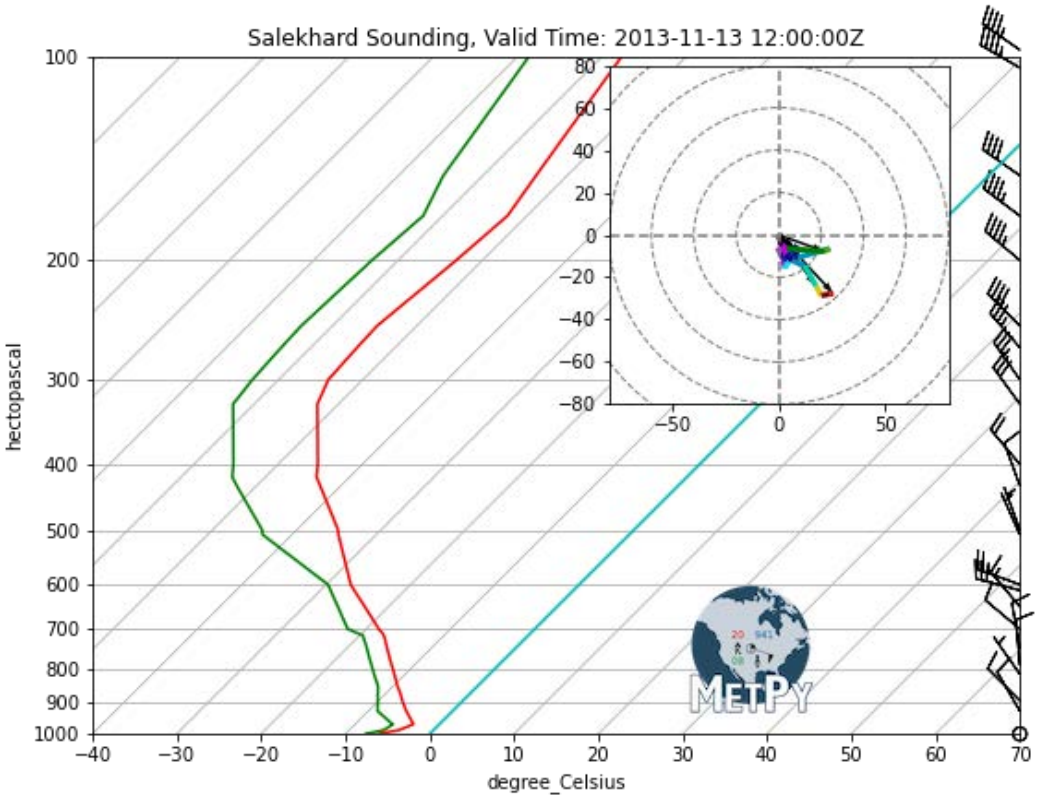

Figure 3.2.21: Salekhard Sounding for November 13, 2013, at 12Z. The red and green lines represent the temperature and dewpoint temperature, respectively, recorded with height.

November 8. The wind behavior also changed through much of the profile. Wind speeds are distinctly lower, not reaching above 50 knots anywhere in the column. Directions were also mostly out of the northwest, which brought in additional drier, polar air.

3.2.3.4: Level of Contribution from Atmospheric Rivers

The Yamal Peninsula does not receive maritime influences comparable to sites near the northern North Atlantic. Other case locations – such as Svalbard and western

Greenland – received direct onshore flow, and the ROS events associated with these cases were heavily influenced by ARs. The synoptic setup with the Yamal case managed to pull moisture from what appears to be an AR impacting western Europe in the North Atlantic. This is based on the IVT and PWAT reanalysis procedures in Subsection 3.1.3, Figures 3.1.25-3.1.31. The IVT plot shows moisture from the Atlantic Ocean following a shortwave over eastern Europe, with the enhanced moisture moving along the gradient between the shortwave and the strong high pressure located over northwest Russia. Additional moisture is being pulled north by a much stronger cyclone centered north of Svalbard. This setup demonstrates an example of an AR providing indirect impacts, like the Banks Island case from 2003.

The HYSPLIT run for this case (Figure 3.2.22) provides additional support for this supposition. A backward trajectory for the peninsula on November 7 at 12Z indicated air mass sources originating around the Mediterranean Sea four days prior. Even in the late autumn months, this region remains relatively warm and moist, so the air mass originating from here may have retained these characteristics. Despite this, this location was above 30 °N and did not classify as a subtropical maritime location. In addition, the HYSPLIT results were likely following the shortwave that moves from the Mediterranean and into eastern Europe.

For the 925-mb, 850-mb, and 700-mb equivalent heights, the trajectories did not change much throughout the 96-hour period or during travel through northern Russia. This implies that the air mass maintained similar properties from what it exhibited near the Mediterranean, undergoing cooling but likely maintaining high moisture content. From the atmospheric reanalysis, moisture from the probable AR in the Atlantic was

streaming through this area and probably contributed more moisture to this air mass.

This reaffirms that, even though the North Atlantic AR did not directly impact the Yamal

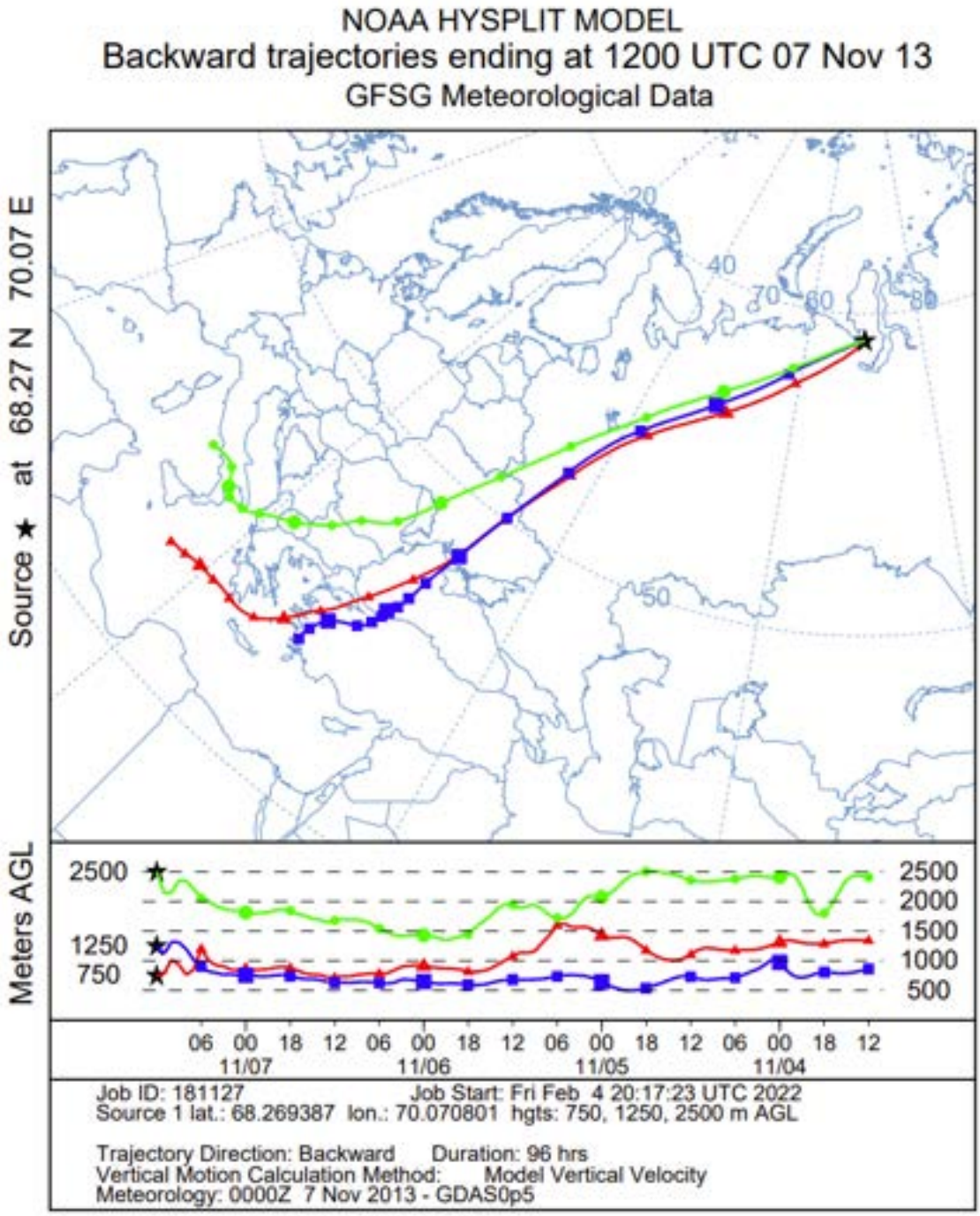

Figure 3.2.22: 2013 ROS Event HYSPLIT Results (Nov 07). This is the HYSPLIT run for the Yamal Peninsula, Russia, ROS event from November 2013.

Peninsula, this ROS event was still influenced by the moisture it produced.

3.2.4: Case Study 4 – Western Greenland (April 2016)

3.2.4.1: Case Background

Greenland has a large influence on weather dynamics for much of the North Atlantic. This island (the largest on the planet) abuts the north Atlantic Ocean, where the Atlantic Meridional Overturning Circulation (AMOC) brings warm surface waters from the tropics (Ahrens 2009). Greenland also possesses the only ice sheet remaining in the Northern Hemisphere. This cold land mass lying tangential to the warmer waters in the North Atlantic generates a substantial air temperature gradient and baroclinic zone to assist in extratropical cyclone generation, maintenance, and intensification (Serreze and Barry 2014). Baroclinicity is strongest in winter, with the frigid land and sea ice margin in proximity to the relatively warmer ocean waters, and contributes to a maximum in extratropical cyclone activity in the North Atlantic during the winter, largely in the region between Iceland and Greenland (Serreze 1995).

Weather systems traversing through or near Greenland are also influenced by the island's topography. In addition to Greenland being an ideal region for cyclogenesis from the natural baroclinic zone, there is a region of lee cyclogenesis just to the southeast of the island. High precipitation amounts also characterize the southeast Greenland coast, reflecting orographic uplift (Schuenemann, Cassano, and Finnis 2009). The area along western Greenland is also known for cyclolysis or weakening of cyclones as they travel into higher latitudes and navigate complex terrain. Cyclones that approach from the west, typically out of Baffin Bay, can become blocked against the higher terrain inland, and the Greenland Ice Sheet also provides for additional

orographic blocking in these instances (Schuenemann, Cassano, and Finnis 2009; Serreze 1995). Additionally, the high elevation and the ice sheet work in tandem to cause cyclone bifurcation or splitting – especially at the southern tip of Greenland – which further complicates cyclone behavior (Tsukernik, Kindig, and Serreze 2007; Schuenemann, Cassano, and Finnis 2009).

This ROS event over Greenland took place over the course of a few days in early to mid-April in 2016 and impacted the southwestern coastline. Previous researchers studied this event from the context of wet snow and slush avalanches, deploying remote sensing tools and analysis (Abermann et al. 2019). Abermann et al. (2019) conclude that over 800 wet snow avalanches occurred during this period based on radar and satellite imagery prior to and after the avalanche occurrences. They also examined some of the meteorological setup that led to the event.

Abermann et al. (2019) noted that a high-pressure ridge began building on April 9 and continued to strengthen into April 10. The warm sector of an advancing warm front encroached on southwest Greenland, and moisture provided from the North Atlantic (in addition to enhanced orographic lift from the complex terrain) produced substantial precipitation rates during this period. The combination of rapid warming and high precipitation amounts occurred between April 9 and 11, 2016, at their observation station of interest near Nuuk, Greenland. According to Abermann et al. (2019), most of the precipitation fell prior to and during the rapid warming early on April 11. One automated station was destroyed on April 11 at approximately 10:45 am due to avalanche activity; this also coincided with the highest surface temperatures and after the strongest precipitation rates (Abermann et al. 2019).

3.2.4.2: Differences in the Block and Upper-Level Wind Behavior

This ROS event demonstrated a textbook example of an Omega Block early in the period, beginning to take shape on April 9, 2016 (Figure 3.2.23). The block then strengthened to the structure seen in Section 3.1.1, Figure 3.1.4. No other case takes on the distinct shape of the Omega Block quite like this case, and the upper-level winds correspond to this formation with high speeds at the 500-mb level. Even the initial winds around both the broad trough across Canada and the cutoff low over northwestern Europe on April 9 exhibited strong winds aloft and likely led to the strengthening of the overall block.

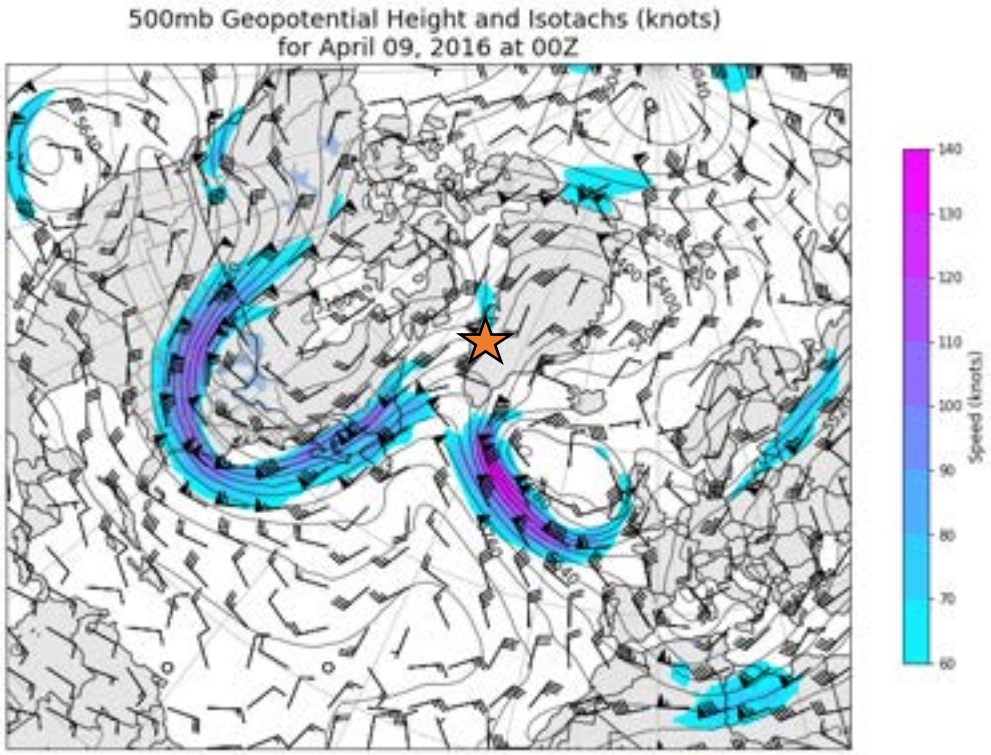

Figure 3.2.23: 500-mb Procedure (04/09/2016). The image includes 500-mb heights and winds, with wind speed realized as filled contours. Data are for April 9, 2016, at 00Z.

An embedded shortwave over Canada exited over Baffin Bay on April 10, which allowed the stronger winds around the Canadian trough to pivot northeast and target

western Greenland with wind speeds greater than 80 knots. This case produced some of the strongest winds of all cases throughout the entire atmosphere, as depicted in the reanalysis data. In addition, the location studied in Abermann et al. (2019) that experienced the highest wet snow avalanche activity on April 11 was in line with the strongest southerly winds aloft at the time. This was discussed in section 3.1.1 as prime placement for a ROS event to occur. This was also like other case studies – except for the Banks Island event – in that it revealed a strong jet streak aloft. Recall for the Banks Island case that that ROS event was linked to the occurrence of drizzle, whereas this event (conversely) coincided with heavy accumulating rain.

Like other cases, the ridge remained in place across much of southern Greenland for a few days following April 11, the main day of ROS conditions. By April 13, the trough over Canada weakened progressively, allowing the ridge to overtop the cutoff low near Europe on the eastern edge of the block. The pattern became more reminiscent of a Rex Block, as demonstrated by the reanalysis for April 16 (Figure 3.2.24). Lower heights had also begun to move in across much of Greenland, replacing the warm, moist air that had moved in previously with a much drier, cooler air mass.

Additionally, wind speeds decreased substantially in the upper levels, as seen in Figure 3.2.24.

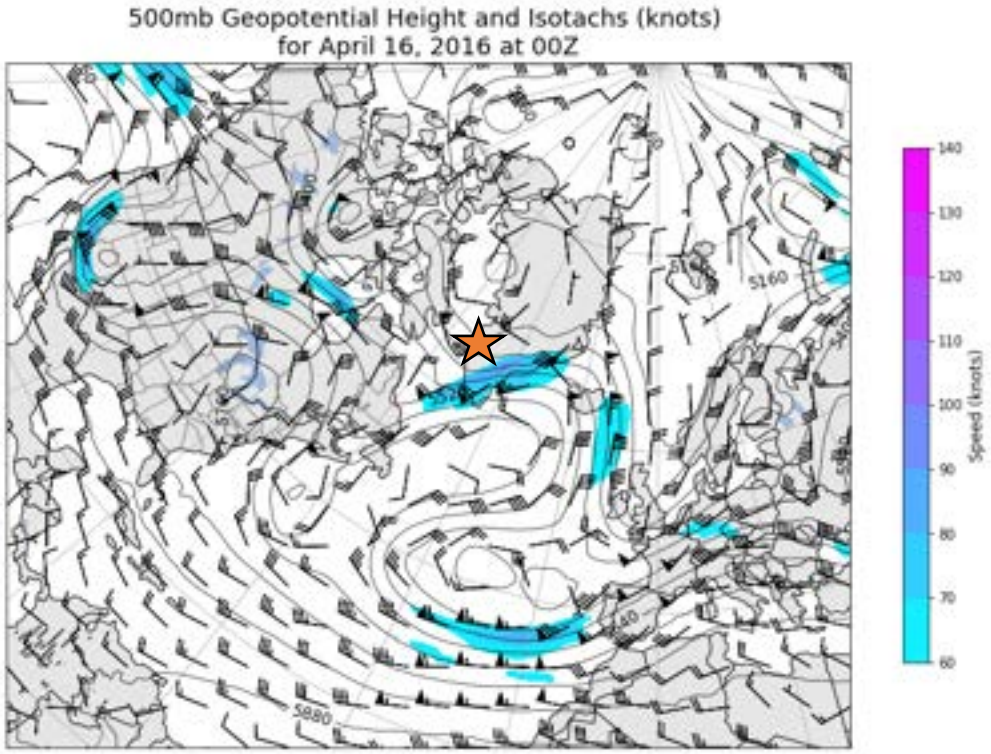

Figure 3.2.24: 500-mb Procedure (04/16/2016). The image includes 500-mb heights and winds, with wind speed realized as filled contours. Data are for April 16, 2016, at 00Z.

3.2.4.3: Differences Among Other Key Atmospheric Components

Recall from Subsection 3.1.2 (Figure 3.1.20) that above freezing air temperatures extended into the 850-mb level of the atmosphere, as the 5 °C isotherm stretched across the southern tip of Greenland. The 925-mb procedure also revealed air temperatures in the 5-15 °C range across the southern half of the island. Moisture variables – indicated by the mixing ratio and PWAT values – were well above average. This event exhibited some of the highest temperature and moisture values among all the cases.

Not only were winds strong in the upper levels, but speeds ranged from 50-70 knots in a tight corridor over Baffin Bay from the 925-mb to the 850-mb level. This was

one of the more noteworthy LLJs of the five ROS cases. Winds were naturally strong in this corridor, since there was less frictional influence over the ocean waters. However, one can still see 40-50 knot winds making headway inland in the 925-mb and 850-mb procedures. The positioning of this corridor (directly over the warmer waters of the North Atlantic) also produced enhanced warm air advection and onshore flow, directing south to north flow right through Baffin Bay and targeting the west, southwest coast of Greenland.

Soundings taken during the event confirm the strength of the warm nose, moisture transport, and the LLJ. The sounding is from Aasiaat, Greenland, which lies just to the north of Nuuk, the site of interest in the Abermann et al. (2019) study. On April 11 at 12Z (Figure 3.2.25), the upper air data revealed similar parameters as what was discerned from the reanalysis. PWAT calculated from this sounding was 19.58 millimeters, a significantly moist environment for this latitude and time of year. The

warm nose was very prominent, extending from the surface to about the 850-mb level. A very sharp inversion was also evident at the surface, with air temperatures increasing in height up to the 950-mb level. The LLJ was evident in the sounding as well, with additional onshore flow, and the hodograph shows the warm air advection occurring

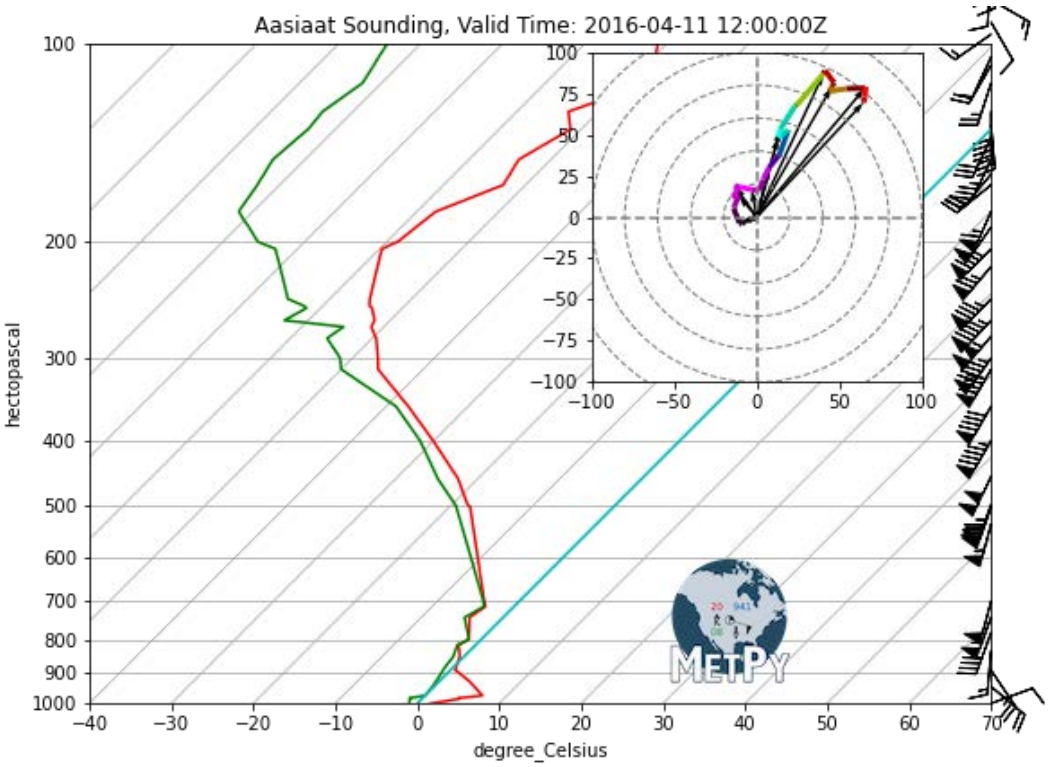

Figure 3.2.25: Aasiaat Sounding for April 11, 2016, at 12Z. The red and green lines represent the temperature and dewpoint temperature, respectively, recorded with height.

with height. Based on this sounding, this profile would have generated all rain, with the surface being above freezing and with this much of a warm nose. This is also evident in the station data (Figure 3.2.26).

Using surface observations from the station in Godthaab, one can see the changes in air temperature and the consequent changes in precipitation types that were recorded. Like the observations from the earlier Svalbard case, there was a pattern of air temperatures increasing prior to the ROS event with a corresponding change to

liquid precipitation. The surface air temperature increased to above 60 °F on April 11, a surprising (even shocking) value for Greenland in April. Temperatures then decreased in the following days, and precipitation generally transitioned to solid categories, with periods of mixed precipitation scattered throughout. Air temperatures dropped below freezing starting on April 13, and then remained mostly below freezing beginning on April 15. This would have allowed the previous liquid that fell with the initial storm system to freeze on or within the snowpack.

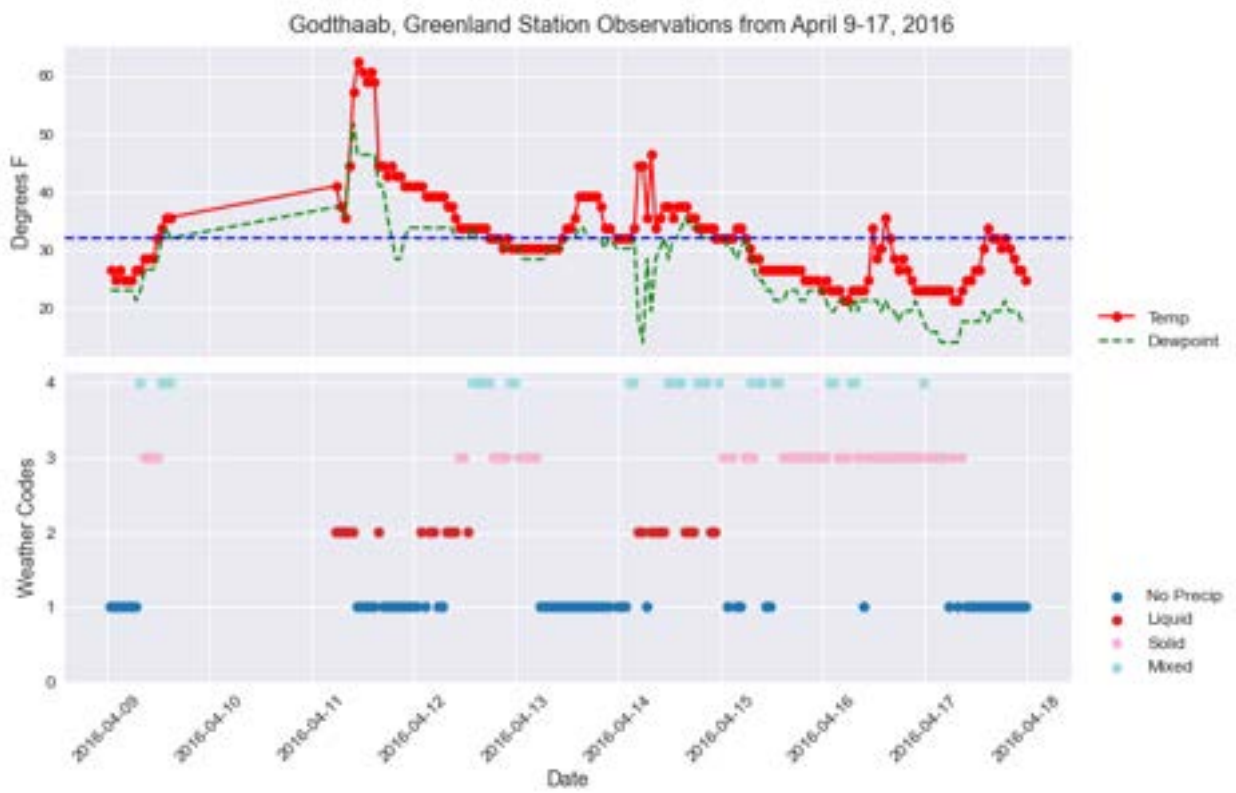

Figure 3.2.26: 2016 Western Greenland ROS Event Observations. The image includes Godthaab station observations from April 9-17, 2016. Temperature and dewpoint temperature are plotted in the upper graph in °F, and the corresponding precipitation types are plotted in the bottom graph.

A post-ROS event skew-t image (Figure 3.2.27) is included to demonstrate the changes in the atmospheric profile following ROS conditions. Again, this was a sounding taken at Aasiaat, north of Godthaab, but it stayed in line with the atmospheric reanalysis findings. Further, it followed the evolution of the atmosphere after a ROS

event, as evidenced in other cases. As the lower geopotential heights moved in aloft, a much cooler and drier air mass replaced the previous wet and warm air mass across

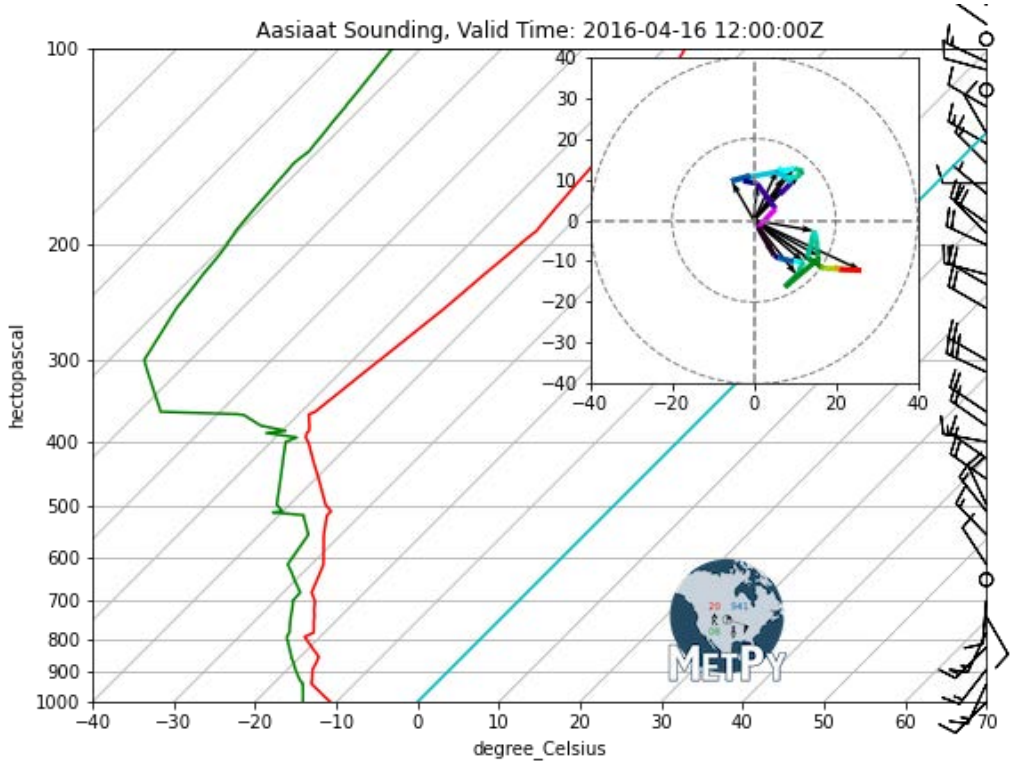

Figure 3.2.27: Aasiaat Sounding for April 16, 2016, at 12Z. The red and green lines represent the temperature and dewpoint temperature, respectively, recorded with height.

Greenland. This is seen in the sounding in several ways: 1) the temperature is below freezing throughout the entire profile (even at the surface), 2) moisture has decreased (calculated PWAT fell to 3.99 millimeters), and 3) the tropopause height noticeably lowers, where temperatures begin increasing with height moving into the stratosphere. Wind speeds were also much lighter throughout the atmospheric column, and the directions were largely out of the northwest in the middle to upper levels, indicating cold air advection.

3.2.4.4: Level of Contribution from Atmospheric Rivers

Much of the coastal region of Greenland is heavily influenced by the waters of the North Atlantic, but the evidence provided by the atmospheric reanalysis shows that

an AR directly impacted western Greenland. This feature likely led to major contributions through increasing air temperatures, initiating precipitation, and generating higher accumulation amounts. The results from the HYSPLIT model (Figure 3.2.28) provide additional evidence that an AR directly impacted this ROS event. Air masses at the approximate 925-mb, 850-mb, and 700-mb heights originated from the tropics south of 30° N latitude. Specifically, they originated from the Caribbean, which the PWAT procedure also showed in Subsection 3.1.3, Figure 3.1.32. The relative heights also

lowered throughout the 96-hour period relative to their place of origin, likely reflecting moving north into a more polar environment.

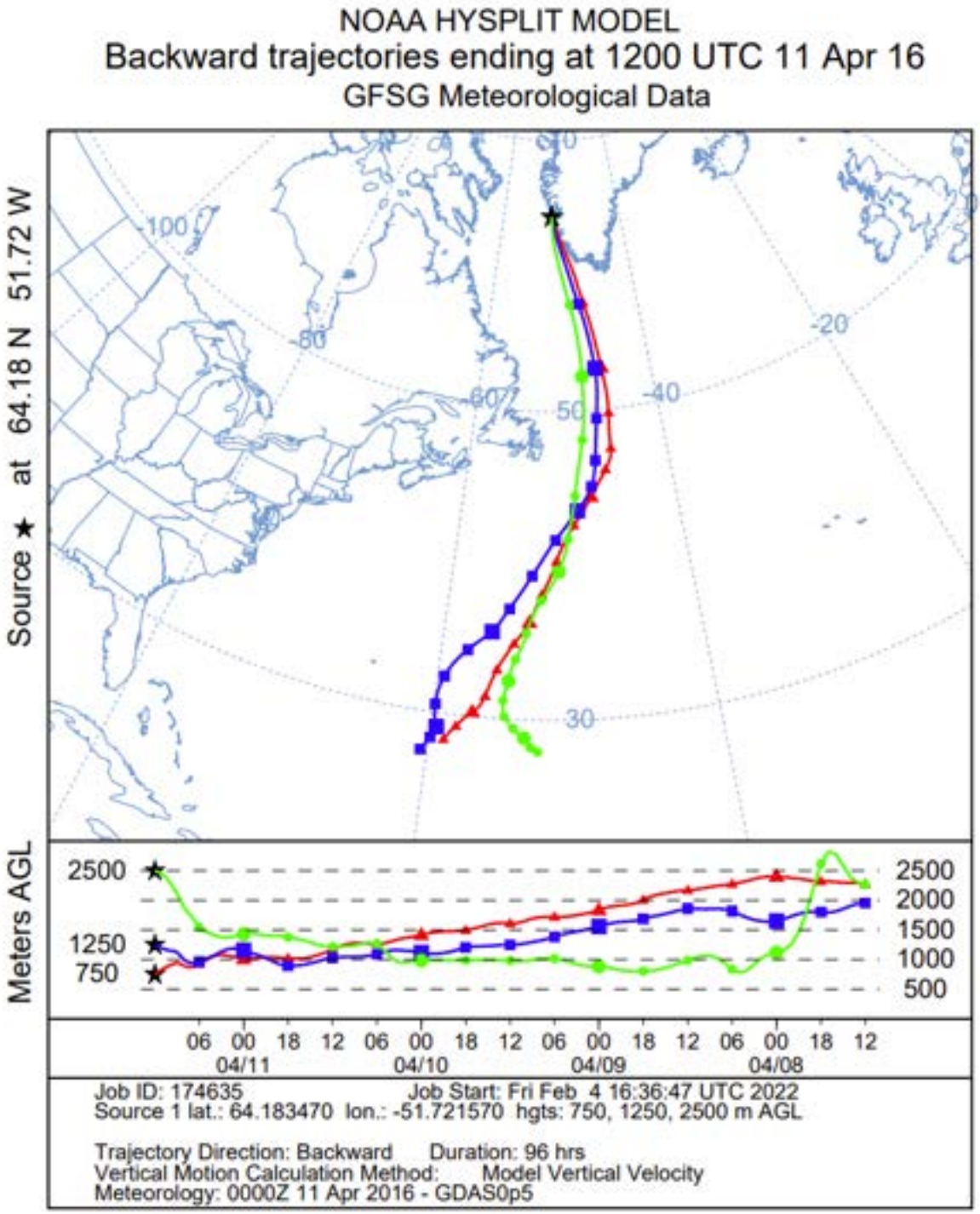

Figure 3.2.28: 2016 ROS Event HYSPLIT Results (April 11). This is the HYSPLIT run for the Western Greenland ROS event from April 2016.

3.2.5: Case Study 5 – Iqaluit, Canada (January 2021)

3.2.5.1: Case Background

Interest in this case began with an email sent from one of the Arctic Rain-on-Snow Study (AROSS) team members on the afternoon of January 19, 2021. The team member reported that rain was falling that day in Iqaluit, Canada, a community located on Baffin Island in the Canadian Arctic Archipelago. It experiences similar climate as to what was described earlier for the Banks Island case study. However, this area lies on the eastern periphery of the archipelago and is subject to precipitation influences from the North Atlantic and Baffin Bay. During the lead up to this ROS event, much of Canada had also been experiencing anomalously high temperatures. In early January, temperatures had actually been fairly cold but rapidly warmed – by more than 30 °C at some locations across the archipelago – proceeding into the second week of January (CBC News 2021).

From an article published on January 18, 2021, for the “Nunatsiaq News,” Iqaluit was expected to continue seeing unseasonably high temperatures in the middle of January. The article describes a low-pressure system moving in for the coming week (bringing warm air from the south) and causing temperatures to hover around the freezing mark (Nunatsiaq. News 2021). Climate data for Iqaluit (provided by the Government of Canada – https://climate.weather.gc.ca/historical_data/search_historic_data_e.html) shows a snow-on-the-ground depth of 25 centimeters (9.84 inches) for January 6, 2021. Unfortunately, there is a period of missing data from January 7 through January 19. The next observation for snow depth was on January 20, with another snow depth of 25

centimeters. However, one can surmise from this that there was a snowpack at the time rain was reported in Iqaluit on January 19.

3.2.5.2: Differences in the Block and Upper-Level Wind Behavior

As opposed to an Omega block, this case initially began with more of a Rex Block pattern (Subsection 3.1.1, Figure 3.1.5). This resulted from a deep trough across Canada undercutting the weak ridge of high pressure centered over southern Greenland (Figure 3.2.29). Later in the period, there was a brief setup demonstrating a weak Omega Block on January 21. However, this quickly transitioned to what appears to be a cutoff ridge, more exemplary of a Rex Block again. This represented a unique

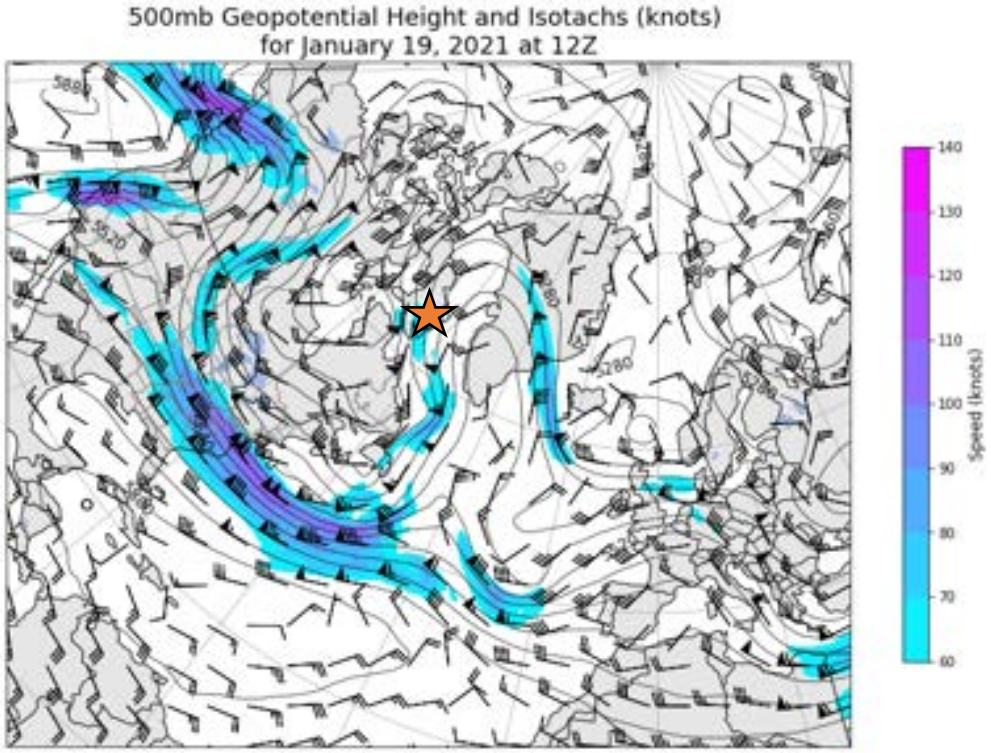

Figure 3.2.29: 500-mb Procedure (01/19/2021). The image includes 500-mb heights and winds, with wind speed realized as filled contours. Data are for January 19, 2021, at 12Z.

aspect of this case with the closing contours of the ridge by January 24, indicating a

cutoff feature from the jet stream aloft, which was also consistent with the upper-level wind recorded in the 500-mb level reanalysis (Figure 3.2.30).

Winds aloft were not especially strong compared to some of the previous cases, but there was still a jet streak located in the same region of interest (Figure 3.2.29). Wind speeds generally ranged from 50-70 knots through the area with the most southerly flow, which crosses through the Labrador Sea north into Baffin Bay and just west of Greenland. An even stronger pocket of winds collocated with the approaching

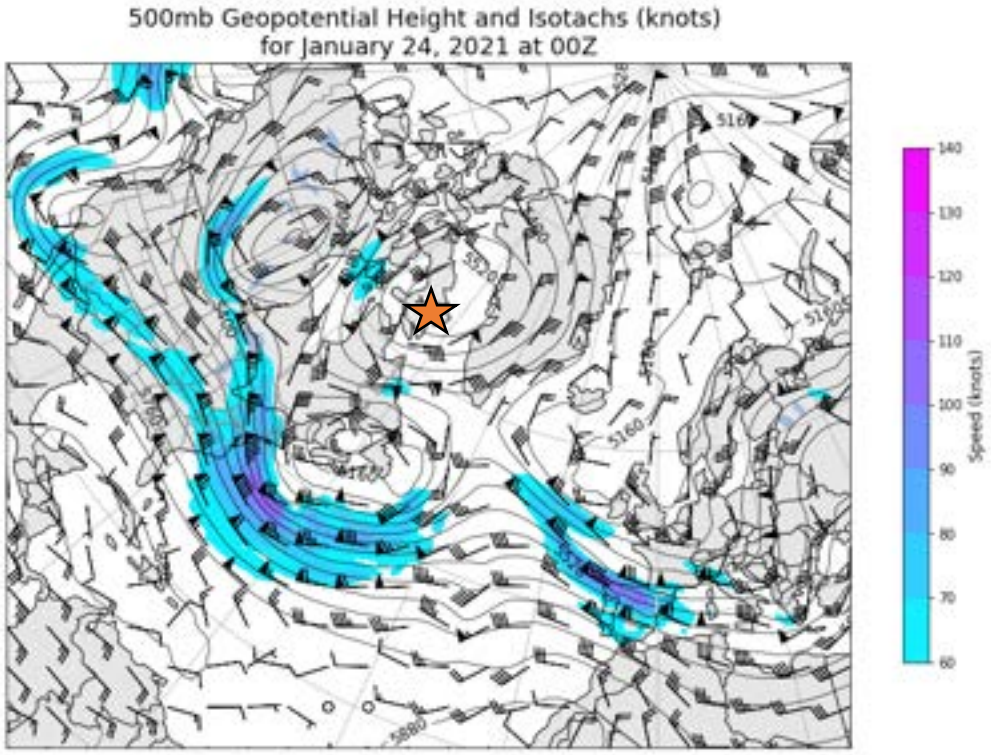

Figure 3.2.30: 500-mb Procedure (01/24/2021). The image includes 500-mb heights and winds, with wind speed realized as filled contours. Data are for January 24, 2021, at 00Z.

shortwave south of Baffin Island and east of Newfoundland and Labrador Province in Canada. A stronger jet streak was present rounding the deepest point of the Canadian trough, which is likely assisting in maintaining the Rex Block and managed to cut the ridge off from the flow aloft later.

3.2.5.3: Differences Among Other Key Atmospheric Components

This case also revealed significant differences among other atmospheric components previously identified as playing key roles in ROS events. Remember from the discussion in Subsection 3.1.2, regarding Figure 3.1.21, that the warm layer did not extend much above the surface. The 925-mb procedure showed temperatures between 0 and -8 °C across the southern tip of Baffin Island. This warm layer was very much limited to just the surface, and this is well represented in the sounding. The skew-t for January 19 at 12Z (Figure 3.2.31) showed air temperatures reaching the freezing point just at the lowest point where the data first began recording. The moisture profile

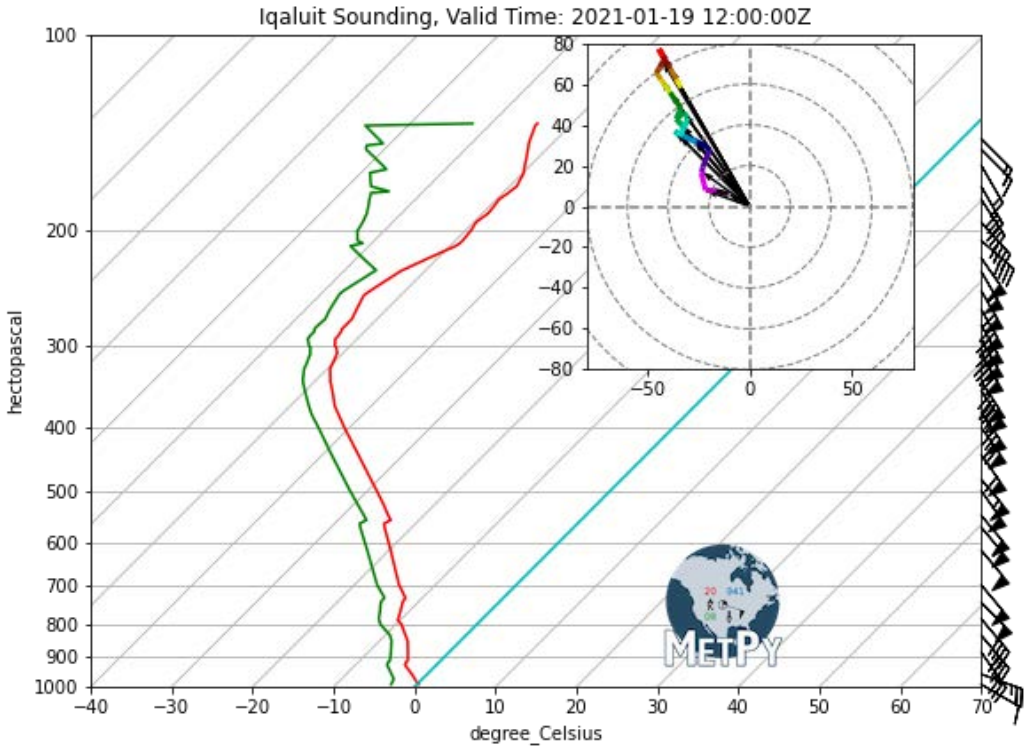

Figure 3.2.31: Iqaluit Sounding for January 19, 2021, at 12Z. The red and green lines represent the temperature and dewpoint temperature, respectively, recorded with height.

yielded a PWAT of 9.19 millimeters, high for the region and time but still modest compared to other cases. This connected well to what was depicted in the ERA5

reanalysis. A noticeable LLJ did occur with this case in the low- to mid-levels with wind speeds of 40-50 knots and included the same veering with height (indicating warm air advection) and substantial onshore flow with winds out of the southeast.

The sounding on January 25 (Figure 3.2.32) also produced similar atmospheric traits as other cases following the ROS event. As lower geopotential heights moved in aloft, air temperatures fell, especially after the passage of the cold front. A drier

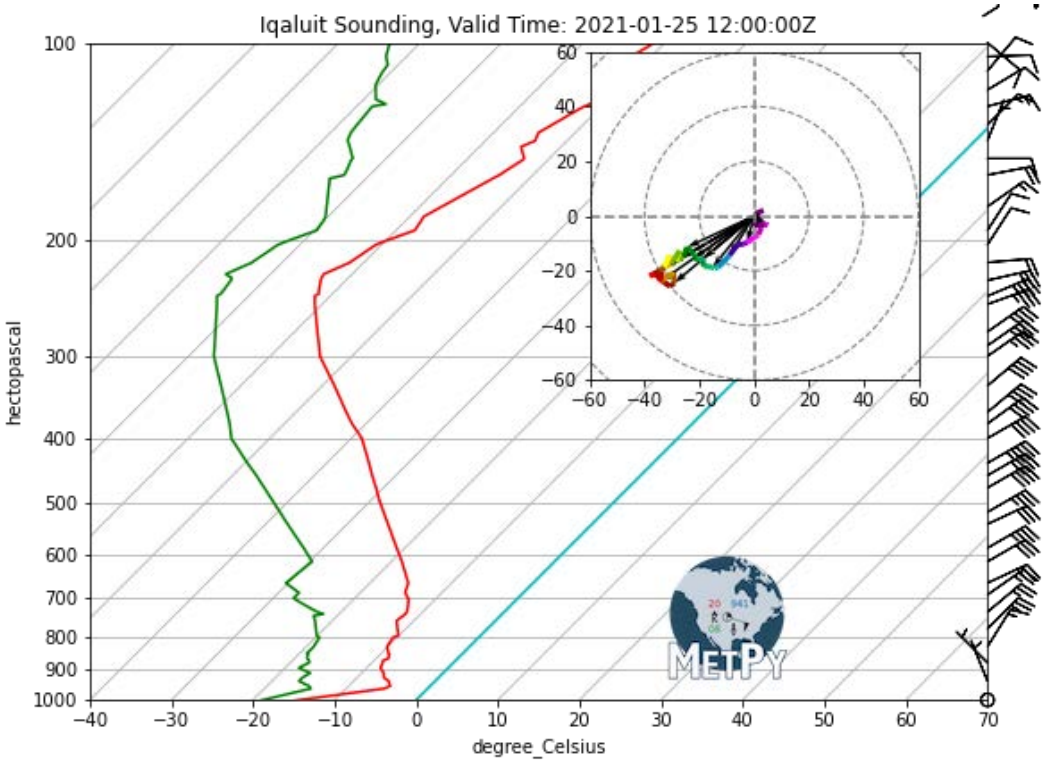

Figure 3.2.32: Iqaluit Sounding for January 25, 2021, at 12Z. The red and green lines represent the temperature and dewpoint temperature, respectively, recorded with height.

moisture profile also took the place of the moist air mass concurrent with the time of ROS conditions. This sounding produced a PWAT value of 4.28 millimeters, much less than the 9.19 millimeters recorded on January 19. Winds throughout the entire atmosphere also changed drastically from a few days prior. Wind speeds slackened, and they backed to the northeast, meaning cold air advection.

Another unique aspect with this case was the lack of liquid or even mixed precipitation types in the station observations at the time of ROS occurrence (Figure 3.2.33). Recall that an eyewitness account confirmed this ROS event. This exemplified a situation where the automated surface observation station (usually collocated with a major airport in the area) may not have been representative of all conditions that occurred during a winter precipitation event. During a typical significant winter storm

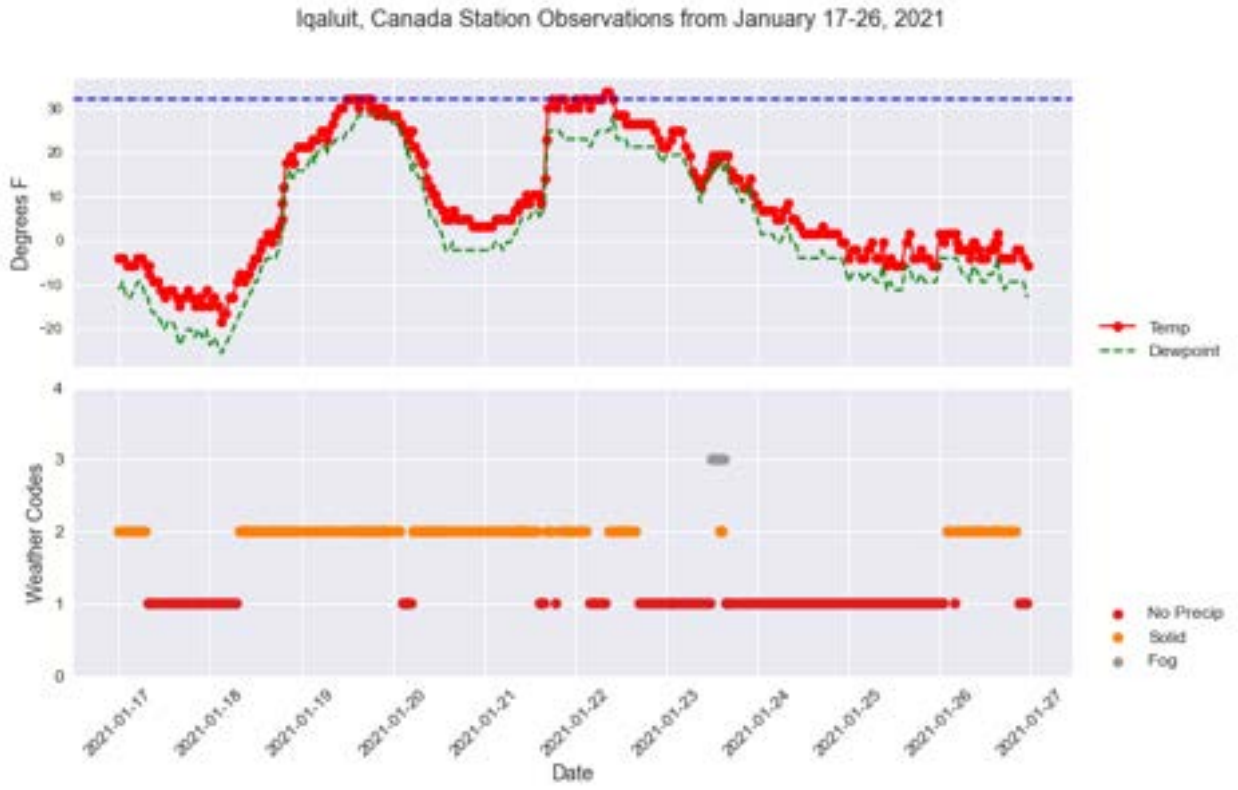

Figure 3.2.33: 2021 Iqaluit ROS Event Observations. This image includes Iqaluit station observations from January 17-26, 2021. Temperature and dewpoint temperature are plotted in the upper graph in °F, and the corresponding precipitation types are plotted in the bottom graph.

system, precipitation types may range from rain or freezing rain to snow based on the positions of locations in relation to various topographic or geographic features and based on the strength and location of the warm nose.

Nevertheless, the station records demonstrated the same pattern seen with other cases when observations were available. Air temperatures increased to just the freezing

point on January 19 but with solid precipitation (snow) continuing. Falling temperatures in successive days would have allowed ice to form from liquid precipitation that accumulated on the underlying snowpack, with only one brief period on January 22 where air temperatures reached the freezing point again. Recall from the previous subsection that Iqaluit reported a snow on the ground of 25 centimeters (around 9.8 inches) on January 5, with a period of missing data, and then another observation of 25 centimeters on January 20.

3.2.5.4: Level of Contribution from Atmospheric Rivers

The HYSPLIT model (Figure 3.2.34) for the Iqaluit ROS event in January of 2021 showed air masses largely originating from the northeastern region of the US. The lowest represented height of 750 meters – demonstrating the 925-mb pressure level equivalent – even began in the midwestern US, around the state of Missouri. This is understandable, based on the interpretation of the ERA5 data with this case presented in Subsection 3.1.3, Figure 3.2.27 and Figure 3.2.33. This case represented an instance of an AR playing an indirect role in the occurrence of ROS conditions at Iqaluit. An AR was positioned along the US eastern seaboard, carrying moisture largely northeast. A potent shortwave system (guided by the block) then proceeded to pull some of this moisture directly north into the southern tip of Baffin Island. What the HYSPLIT model

was following in the backwards trajectory was the progression of this shortwave over the 96-hour period.

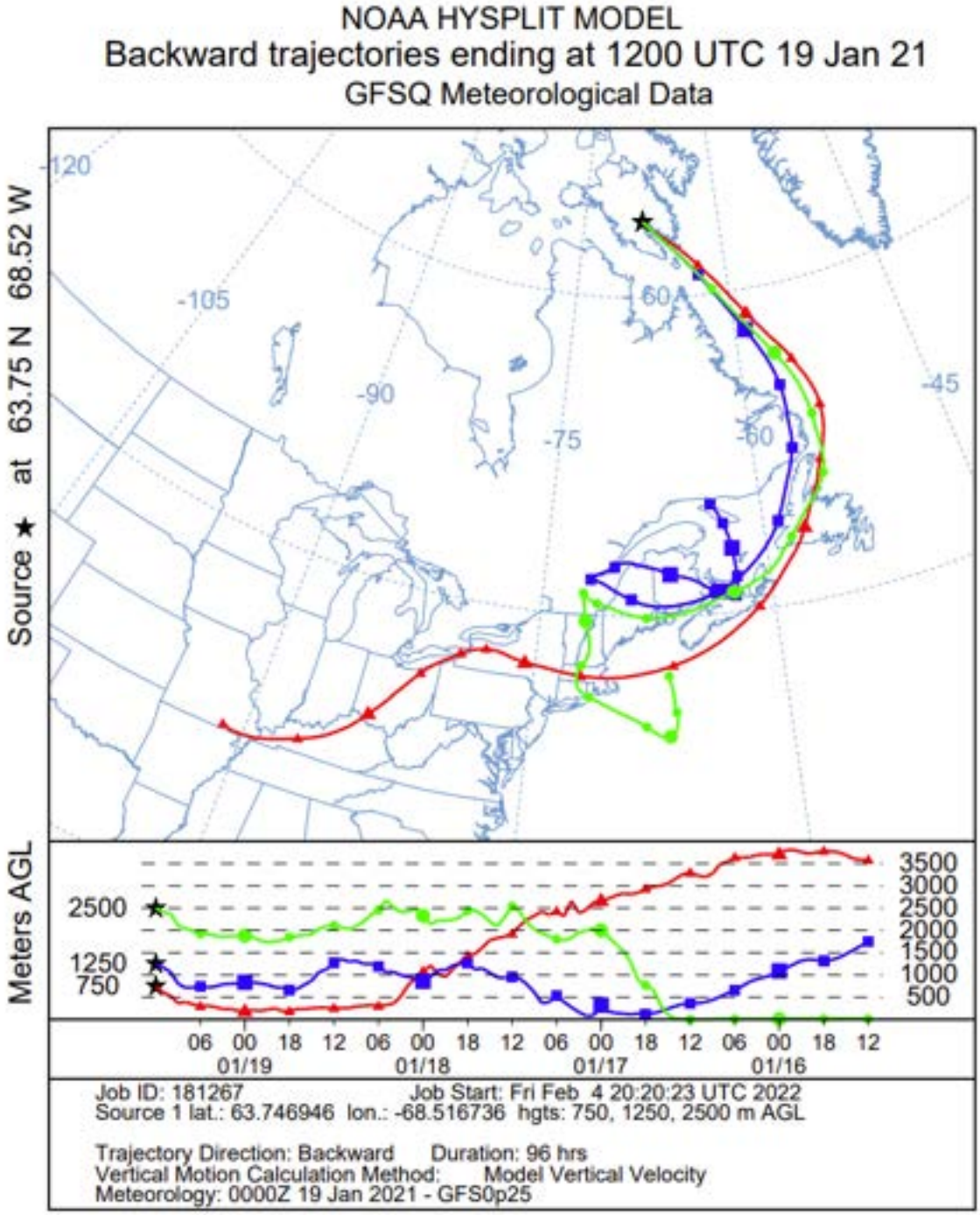

Figure 3.2.34: 2021 ROS Event HYSPLIT Results. This is the HYSPLIT run for the Iqaluit, Canada, ROS event from January 2021.

Chapter 4: Conclusions and Future Work

4.1 Key Findings from This Thesis

Through visualization of ERA5 atmospheric reanalysis data, it was determined from five case studies that blocks and blocking patterns play large roles – if not, the largest role – in the initiation of rain-on-snow (ROS) conditions over the Arctic. Additionally, the overall location of the ROS event in relation to the upper-level block is crucial to these conditions, with many locations positioned under the strongest gradient between the anticyclonic ridge and western most trough. This position in relation to the overall block allowed the location to be beneath the greatest southerly flow aloft. This flow typically takes the form of a jet streak with winds greater than 50 knots at the 500-mb level for most cases. These robust, southerly winds formed west of the axis of the ridge of high pressure – opposite the northerlies on the east side – allowing the blocking formation to persist for several days due to the lack of westerlies present to maintain the wave pattern through a progressive geostrophic flow.

The synoptic setup associated with blocking patterns also drives other meteorological features essential to ROS events. As seen in ERA5 data, the blocks provide the duration necessary for the buildup of a long fetch of higher temperatures and increased moisture in the middle to lower levels. In addition, blocking patterns act to guide shortwaves and low-pressure systems that impact an area located within the enhanced gradient between the blocking ridge and westerly approaching trough. These processes contribute to the formation of other mesoscale features, such as pronounced “warm noses,” low-level jets (LLJs), and enhanced streams of moisture transport. In

some cases, these blocking patterns led to the development of atmospheric rivers (ARs) that directly impacted the ROS conditions.

Supplemental data – including surface station observations, upper air soundings, HYSPLIT models, and eyewitness accounts – proved valuable in verifying the meteorological setup and resulting conditions. Station observations helped confirm similar patterns at the surface documented in previous research, with the initial rise in air temperatures, the consequent initiation of liquid precipitation, and the freezing conditions that followed. Sounding data were used to examine the strength of important meteorological features (e.g., the pronounced warm noses, moisture variables, and atmospheric wind behavior) and provided an additional look at the entire atmospheric column that led to (and followed) the ROS event. In addition, HYSPLIT results confirmed moisture sources provided for ROS event locations to identify indirect or direct effects from ARs, and eyewitness accounts were helpful when observational data was lacking.

With this research, the primary meteorological mechanisms that lead to the occurrence of ROS conditions over a particular area were established, which addresses the first research question posed in Chapter 1, Section 1.5 (the primary meteorological conditions necessary for major Arctic ROS events). It was also determined that the geographic placement of many of these ROS events in relation to the overall blocking pattern (west of the ridge axis and between the ridge and western-most trough) also influenced the weather conditions witnessed at these locations. In addressing the second research question (blocking patterns' role in creating large gradients that allow ARs to form), blocks provide the duration to permit the growth of these long corridors of

higher temperatures and moisture transport. Some cases appear to show ARs forming from blocking patterns. However, two of the five cases did not follow this pattern, but other meteorological features contributed to the warm air advection and moisture transport that occurred with these ROS events. For the two cases where ARs led to a direct impact on ROS conditions, these were cases where ARs made landfall at the location, and they resulted from the overall blocking pattern.

4.2: The Role of Climate Change in the Context of ROS Events

Uncertainties abound regarding how climate change may affect overall atmospheric circulations, in both the Arctic and in middle and lower latitudes. There are several ways and feedback loop relationships that may influence extreme weather events in the future. Arctic ROS events embody the characteristics of an extreme weather event, which may be described as short-lived events that cause devastating impacts to communities and the natural ecosystem. Arctic ROS events may be classified as such, in that they are an unusual and short-lived occurrence for the Arctic – especially through the fall to early spring months – and generate hazards ranging from the transportation sector to infrastructure and resource availability. Many climate scientists conduct extreme weather event research by using an “ingredients-based approach.” This means that if we understand the meteorological components and features that drive these extreme events, one can infer whether these events may become more frequent or severe in the future.

In the warming environment, there may be impacts to blocking patterns as well, and some papers have attempted to find correlations between climate change and any alterations in these patterns. One noted that blocking patterns might decrease in the

middle latitudes, or areas that experience a high number of blocking episodes in the climatology may see a shift in those locations (Woollings et al. 2018). However, Woollings et al. (2018) caution that climate models still struggle in handling blocks and blocking patterns and that natural variability is likely to have a strong influence on blocking patterns in the coming decades (Woollings et al. 2018). Woollings et al. (2018) also add that “the impact of wintertime blocking on temperature is largely due to thermal advection which is likely to weaken in the future, but in contrast the temperature impacts of summertime blocking may strengthen due to soil moisture feedbacks.” Basically, it remains difficult to generalize how blocking patterns will change in a warming world.

Different climate models are in agreement that warming will be attended by an increase in Arctic precipitation (McCrystall et al. 2021). The Clausius-Clapeyron equation codifies the relationship between saturation vapor pressure (e_s) and temperature (T). Recall from Chapter 1 that the equation dictates that for every degree Celsius of warming, the saturation vapor pressure increases by six to seven percent. This leads to the idea that a warmer atmosphere yields more water vapor for storm systems to utilize. In addition, increased air temperatures also increase evaporation rates, adding additional moisture to the atmosphere.

The Arctic is also expected to become a more rain dominated region. According to McCrystall et al. (2021):

> “There is general agreement that Arctic precipitation will increase through the twenty-first century, with estimates ranging from 30% to 60% by the year 2100. A wetter Arctic results from [1] increased evaporation as a result of more open water due to sea-ice loss; [2] higher air temperatures, increasing the

> atmosphere's ability to carry moisture; and [3] increased poleward moisture transport. The Arctic is also expected to transition from a largely snow-dominated to a rain-dominated precipitation regime, a transition already being observed over the Atlantic sector," (McCrystall et al. 2021).

With this resultant shift to a more rain-dominated climate and expected increases in poleward moisture transport, more Arctic ROS events are likely in the future, which McCrystall et al. (2021) allude to in their paper. The authors also suggest that this shift may occur one to two decades earlier than previously thought, with the most alterations to precipitation occurring during the autumn months. On the other hand, a shorter snow cover season implies a reduction in ROS frequency in the shoulder seasons of fall and spring – or perhaps more occurrence of icing from rain over frozen ground, like Bienek et al. (2018) describe in their methodology – and a shift towards more ROS events in midwinter.

A recent paper addressed how the frequency and strength of ARs may respond to climate change. It was found that models project a 10% decrease in the number of ARs, based on the RCP8.5 "worst-case" global emissions scenario from the Intergovernmental Panel on Climate Change (Espinoza et al. 2018). However, they noted that models also projected ARs to be 25% longer, 25% wider, and have larger integrated water vapor transport (IVT) values; they mentioned that this might be largely due to the increasing moisture available in a warming atmosphere (Espinoza et al. 2018). This means that more ARs may potentially reach high Arctic regions, and more extreme IVT values may lead to more high precipitation events associated with ROS events, like the Svalbard ROS case from 2012.

4.3: Next Steps and Prospective Projects

This research fills part of the knowledge gap regarding the synoptic setup and other meteorological features driving Arctic ROS events. The author of this thesis identifies several diverse methodologies that could be applied to future work. The main synoptic patterns of interest were determined, as well as ideal locations for a site to be positioned within the overall pattern to experience ROS. However, there is potential to expand upon this. Applications in machine learning technologies can be used for pattern recognition using atmospheric reanalysis. Results from the case studies examined here could also contribute to better modeling of ROS events and monitoring changes in their behavior. Additionally, these same methods may be deployed in the realm of detections of past events that may have gone unnoticed by observations or that lack eyewitness accounts.

Self-organizing maps (SOMs) hold promise, leveraging machine learning capabilities. According to Sheridan and Lee (2011):

> SOMs use “a neural network algorithm to determine and display the distribution function of a multidimensional dataset. It accomplishes this by creating an array or lattice (the SOM or master SOM) that is generally a two-dimensional matrix of nodes, which (for the purposes of synoptic climatology) can be thought of as analogous to clusters,” (Sheridan and Lee 2011).

This node array is basically used to discern patterns among the data, based on the classification of similar versus dissimilar nodes, which reduces large and complex datasets (Cassano and Cassano 2010; Sheridan and Lee 2011). One example from Cassano and Cassano (2010) describes using SOMs to self-classify daily sea level

pressure anomalies in ERA40 atmospheric reanalysis data in various river basins in Alaska. SOMs represent a viable option in recognizing patterns among reanalysis pertaining to ROS events (notably atmospheric blocks). Another option would be to apply the SOM approach to sounding data, since one can recognize certain meteorological features with these datasets that promote ROS.

Finally, remote sensing methodologies utilizing passive microwave satellite sensors to detect changes in brightness temperatures – like research by Grenfell and Putkonen (2008) – may find further use in combination with other data sources. The combination of passive microwave technologies to detect liquid water on the snow surface and the use of atmospheric reanalysis data, soundings, and surface data (like what was deployed within this thesis) offers paths to better detect ROS events across the Arctic. This approach is also being explored as an ongoing part of the AROSS study. In turn, while as mentioned in Subsection 3.1.3, climate scientists use several algorithms in models and other statistical data in detecting ARs. There is ample room to improve upon and implement such algorithms for Arctic applications, including expanding on AR research in the context of Arctic ROS events.

References

Abermann, Jakob, Markus Eckerstorfer, Eirik Malnes, and Birger Ulf Hansen. 2019. “A Large Wet Snow Avalanche Cycle in West Greenland Quantified Using Remote Sensing and in Situ Observations.” *Natural Hazards* 97 (2): 517–34. https://doi.org/10.1007/s11069-019-03655-8.

Ahrens, C. Donald. 2009. *Meteorology Today: An Introduction to Weather, Climate, and the Environment*. Ninth Edition. Belmont, CA: Brooks/Cole, Cengage Learning.

Barriopedro, David, Ricardo García-Herrera, Anthony R. Lupo, and Emiliano Hernández. 2006. “A Climatology of Northern Hemisphere Blocking.” *Journal of Climate* 19 (6): 1042–63. https://doi.org/10.1175/JCLI3678.1.

Benedict, James J., Amy C. Clement, and Brian Medeiros. 2019. “Atmospheric Blocking and Other Large-Scale Precursor Patterns of Landfalling Atmospheric Rivers in the North Pacific: A CESM2 Study.” *Journal of Geophysical Research: Atmospheres* 124 (21): 11330–53. https://doi.org/10.1029/2019JD030790.

Bernstein, Ben C. 2000. “Regional and Local Influences on Freezing Drizzle, Freezing Rain,and Ice Pellet Events.” *Weather and Forecasting* 15 (5): 485–508. https://doi.org/10.1175/1520-0434(2000)015<0485:RALIOF>2.0.CO;2.

Bieniek, Peter A., Uma S. Bhatt, John E. Walsh, Rick Lader, Brad Griffith, Jennifer K. Roach, and Richard L. Thoman. 2018. “Assessment of Alaska Rain-on-Snow Events Using Dynamical Downscaling.” *Journal of Applied Meteorology and Climatology* 57 (8): 1847–63. https://doi.org/10.1175/JAMC-D-17-0276.1.

“Blocking - Glossary of Meteorology.” n.d. Accessed November 19, 2021. https://glossary.ametsoc.org/wiki/Blocking.

Bluestein, Howard B. 1993. *Synoptic-Dynamic Meteorology in Midlatitudes: Observations and Theory of Weather Systems*. Vol. Volume II. New York, NY: Oxford University Press.

Bourne, S. M., U. S. Bhatt, J. Zhang, and R. Thoman. 2010. “Surface-Based Temperature Inversions in Alaska from a Climate Perspective.” *Atmospheric Research*, Special Section: Little Alaska Weather Symposium 2008, 95 (2): 353–66. https://doi.org/10.1016/j.atmosres.2009.09.013.

Cassano, Elizabeth N., and John J. Cassano. 2010. “Synoptic Forcing of Precipitation in the Mackenzie and Yukon River Basins.” *International Journal of Climatology* 30 (5): 658–74. https://doi.org/10.1002/joc.1926.

Cohen, Judah, James A. Screen, Jason C. Furtado, Mathew Barlow, David Whittleston, Dim Coumou, Jennifer Francis, et al. 2014. “Recent Arctic Amplification and Extreme Mid-Latitude Weather.” *Nature Geoscience* 7 (9): 627–37. https://doi.org/10.1038/ngeo2234.

Cohen, Judah, Hengchun Ye, and Justin Jones. 2015. “Trends and Variability in Rain-on-Snow Events.” *Geophysical Research Letters* 42 (17): 7115–22. https://doi.org/10.1002/2015GL065320.

Cordeira, Jason M., F. Martin Ralph, Andrew Martin, Natalie Gaggini, J. Ryan Spackman, Paul J. Neiman, Jonathan J. Rutz, and Roger Pierce. 2017. “Forecasting Atmospheric Rivers during CalWater 2015.” *Bulletin of the American Meteorological Society* 98 (3): 449–59. https://doi.org/10.1175/BAMS-D-15-00245.1.

Crawford, Alex D., Karen E. Alley, Anna M. Cooke, and Mark C. Serreze. 2020. “Synoptic Climatology of Rain-on-Snow Events in Alaska.” *Monthly Weather Review* 148 (3): 1275–95. https://doi.org/10.1175/MWR-D-19-0311.1.

Dee, Dick, John Fasullo, Dennis Shea, John Walsh, and National Center for Atmospheric Research Staff. 2016. “The Climate Data Guide: Atmospheric Reanalysis: Overview & Comparison Tables,” December. https://climatedataguide.ucar.edu/climate-data/atmospheric-reanalysis-overview-comparison-tables.

Espinoza, Vicky, Duane E. Waliser, Bin Guan, David A. Lavers, and F. Martin Ralph. 2018. “Global Analysis of Climate Change Projection Effects on Atmospheric Rivers.” *Geophysical Research Letters* 45 (9): 4299–4308. https://doi.org/10.1029/2017GL076968.

Forbes, Bruce C. 1999. “Land Use and Climate Change on the Yamal Peninsula of North-West Siberia: Some Ecological and Socio-Economic Implications.” *Polar Research* 18 (2): 367–73. https://doi.org/10.3402/polar.v18i2.6597.

Forbes, Bruce C., Timo Kumpula, Nina Meschtyb, Roza Laptander, Marc Macias-Fauria, Pentti Zetterberg, Mariana Verdonen, et al. 2016. “Sea Ice, Rain-on-Snow and Tundra Reindeer Nomadism in Arctic Russia.” *Biology Letters* 12 (11): 20160466. https://doi.org/10.1098/rsbl.2016.0466.

Francis, Jennifer A., and Stephen J. Vavrus. 2012. “Evidence Linking Arctic Amplification to Extreme Weather in Mid-Latitudes.” *Geophysical Research Letters* 39 (6). https://doi.org/10.1029/2012GL051000.

———. 2015. “Evidence for a Wavier Jet Stream in Response to Rapid Arctic Warming.” *Environmental Research Letters* 10 (1): 014005. https://doi.org/10.1088/1748-9326/10/1/014005.

GISTEMP Team. 2022: *GISS Surface Temperature Analysis (GISTEMP), version 4*. NASA Goddard Institute for Space Studies. Dataset accessed 2022-03-01 at data.giss.nasa.gov/gistemp/.

Gorodetskaya, Irina V., Maria Tsukernik, Kim Claes, Martin F. Ralph, William D. Neff, and Nicole P. M. Van Lipzig. 2014. “The Role of Atmospheric Rivers in Anomalous Snow Accumulation in East Antarctica.” *Geophysical Research Letters* 41 (17): 6199–6206. https://doi.org/10.1002/2014GL060881.

Graham, Robert M., Stephen R. Hudson, and Marion Maturilli. 2019. “Improved Performance of ERA5 in Arctic Gateway Relative to Four Global Atmospheric Reanalyses.” *Geophysical Research Letters* 46 (11): 6138–47. https://doi.org/10.1029/2019GL082781.

Grenfell, T. C., and J. Putkonen. 2008. “A Method for the Detection of the Severe Rain-on-Snow Event on Banks Island, October 2003, Using Passive Microwave Remote Sensing.” *Water Resources Research* 44 (3). https://doi.org/10.1029/2007WR005929.

Guan, Bin, and Duane E. Waliser. 2015. “Detection of Atmospheric Rivers: Evaluation and Application of an Algorithm for Global Studies.” *Journal of Geophysical Research: Atmospheres* 120 (24): 12514–35. https://doi.org/10.1002/2015JD024257.

Guan, Bin, Duane E. Waliser, F. Martin Ralph, Eric J. Fetzer, and Paul J. Neiman. 2016. “Hydrometeorological Characteristics of Rain-on-Snow Events Associated with Atmospheric Rivers.” *Geophysical Research Letters* 43 (6): 2964–73. https://doi.org/10.1002/2016GL067978.

Hall, Richard, Róbert Erdélyi, Edward Hanna, Julie M. Jones, and Adam A. Scaife. 2015. “Drivers of North Atlantic Polar Front Jet Stream Variability.” *International Journal of Climatology* 35 (8): 1697–1720. https://doi.org/10.1002/joc.4121.

Hansen, Brage B., Ketil Isaksen, Rasmus E. Benestad, Jack Kohler, Åshild Ø Pedersen, Leif E. Loe, Stephen J. Coulson, Jan Otto Larsen, and Øystein Varpe. 2014. “Warmer and Wetter Winters: Characteristics and Implications of an Extreme Weather Event in the High Arctic.” *Environmental Research Letters* 9 (11): 114021. https://doi.org/10.1088/1748-9326/9/11/114021.

Hersbach, Hans, Bill Bell, Paul Berrisford, Shoji Hirahara, András Horányi, Joaquín Muñoz-Sabater, Julien Nicolas, et al. 2020. “The ERA5 Global Reanalysis.” *Quarterly Journal of the Royal Meteorological Society* 146 (730): 1999–2049. https://doi.org/10.1002/qj.3803.

Holton, James R. 2004. *An Introduction to Dynamic Meteorology*. Fourth Edition. Burlington, MA; San Diego, CA; London, UK: Elsevier Academic Press.

Intrieri, J. M., G. de Boer, M. D. Shupe, J. R. Spackman, J. Wang, P. J. Neiman, G. A. Wick, T. F. Hock, and R. E. Hood. 2014. “Global Hawk Dropsonde Observations of the Arctic Atmosphere Obtained during the Winter Storms and Pacific Atmospheric Rivers (WISPAR) Field Campaign.” *Atmospheric Measurement Techniques* 7 (11): 3917–26. https://doi.org/10.5194/amt-7-3917-2014.

Keeley, Sarah. 2013. “Climate Reanalysis.” Text. ECMWF. December 17, 2013. https://www.ecmwf.int/en/research/climate-reanalysis.

Lackmann, Gary. 2011. *Midlatitude Synoptic Meteorology: Dynamics, Analysis, and Forecasting*. Boston, MA: American Meteorological Society.

Lackmann, Gary M. 2002. “Cold-Frontal Potential Vorticity Maxima, the Low-Level Jet, and Moisture Transport in Extratropical Cyclones.” *Monthly Weather Review* 130 (1): 59–74. https://doi.org/10.1175/1520-0493(2002)130<0059:CFPVMT>2.0.CO;2.

Leavesley, George H. 1997. *Destructive Water: Water-Caused Natural Disasters, Their Abatement and Control*. International Association of Hydrological Sciences.

Lenssen, Nathan J. L., Gavin A. Schmidt, James E. Hansen, Matthew J. Menne, Avraham Persin, Reto Ruedy, and Daniel Zyss. 2019. “Improvements in the GISTEMP Uncertainty Model.” *Journal of Geophysical Research: Atmospheres* 124 (12): 6307–26. https://doi.org/10.1029/2018JD029522.

Lindsay, R., M. Wensnahan, A. Schweiger, and J. Zhang. 2014. “Evaluation of Seven Different Atmospheric Reanalysis Products in the Arctic.” *Journal of Climate* 27 (7): 2588–2606. https://doi.org/10.1175/JCLI-D-13-00014.1.

Masato, Giacomo, Brian J. Hoskins, and Tim Woollings. 2013. “Wave-Breaking Characteristics of Northern Hemisphere Winter Blocking: A Two-Dimensional Approach.” *Journal of Climate* 26 (13): 4535–49. https://doi.org/10.1175/JCLI-D-12-00240.1.

McCabe, Gregory J., Martyn P. Clark, and Lauren E. Hay. 2007. “Rain-on-Snow Events in the Western United States.” *Bulletin of the American Meteorological Society* 88 (3): 319–28. https://doi.org/10.1175/BAMS-88-3-319.

McCrystall, Michelle R., Julienne Stroeve, Mark Serreze, Bruce C. Forbes, and James A. Screen. 2021. “New Climate Models Reveal Faster and Larger Increases in Arctic Precipitation than Previously Projected.” *Nature Communications* 12 (1): 6765. https://doi.org/10.1038/s41467-021-27031-y.

Melling, Humfrey. 2002. “Sea Ice of the Northern Canadian Arctic Archipelago.” *Journal of Geophysical Research: Oceans* 107 (C11): 2-1-2–21. https://doi.org/10.1029/2001JC001102.

Moon, Twila, Andreas Ahlstrøm, Heiko Goelzer, William Lipscomb, and Sophie Nowicki. 2018. “Rising Oceans Guaranteed: Arctic Land Ice Loss and Sea Level Rise.” *Current Climate Change Reports* 4 (3): 211–22. https://doi.org/10.1007/s40641-018-0107-0.

News, Bradlyn Oakes · CBC. 2021. “Mild Start to 2021 in the North with Record-Breaking Temperatures | CBC News.” CBC. January 9, 2021. https://www.cbc.ca/news/canada/north/2021-north-record-breaking-temperatures-1.5867219.

News, Nunatsiaq. 2021. “Mild Stretch Sets the Stage for Record-Breaking Warmth in Iqaluit.” *Nunatsiaq News* (blog). January 18, 2021. https://nunatsiaq.com/stories/article/mild-stretch-sets-the-stage-for-record-breaking-warmth-in-iqaluit/.

Pan, Caleb G., Peter B. Kirchner, John S. Kimball, Youngwook Kim, and Jinyang Du. 2018. “Rain-on-Snow Events in Alaska, Their Frequency and Distribution from Satellite Observations.” *Environmental Research Letters* 13 (7): 075004. https://doi.org/10.1088/1748-9326/aac9d3.

Petty, Grant W. 2008. *A First Course in Atmospheric Thermodynamics*. Madison, WI: Sundog Publishing.

Putkonen, J., and G. Roe. 2003. “Rain-on-Snow Events Impact Soil Temperatures and Affect Ungulate Survival.” *Geophysical Research Letters* 30 (4). https://doi.org/10.1029/2002GL016326.

Ralph, F. M., and M. D. Dettinger. 2011. “Storms, Floods, and the Science of Atmospheric Rivers.” *Eos, Transactions American Geophysical Union* 92 (32): 265–66. https://doi.org/10.1029/2011EO320001.

Ralph, F. M., M. Dettinger, D. Lavers, I. V. Gorodetskaya, A. Martin, M. Viale, A. B. White, et al. 2017. “Atmospheric Rivers Emerge as a Global Science and Applications Focus.” *Bulletin of the American Meteorological Society* 98 (9): 1969–73. https://doi.org/10.1175/BAMS-D-16-0262.1.

Ralph, F. Martin, Paul J. Neiman, and Richard Rotunno. 2005. “Dropsonde Observations in Low-Level Jets over the Northeastern Pacific Ocean from CALJET-1998 and PACJET-2001: Mean Vertical-Profile and Atmospheric-River Characteristics.” *Monthly Weather Review* 133 (4): 889–910. https://doi.org/10.1175/MWR2896.1.

Rauber, Robert M., Larry S. Olthoff, Mohan K. Ramamurthy, Dianne Miller, and Kenneth E. Kunkel. 2001. “A Synoptic Weather Pattern and Sounding-Based Climatology of Freezing Precipitation in the United States East of the Rocky Mountains.” *Journal of Applied Meteorology and Climatology* 40 (10): 1724–47. https://doi.org/10.1175/1520-0450(2001)040<1724:ASWPAS>2.0.CO;2.

Rennert, Kevin J., Gerard Roe, Jaakko Putkonen, and Cecilia M. Bitz. 2009. “Soil Thermal and Ecological Impacts of Rain on Snow Events in the Circumpolar Arctic.” *Journal of Climate* 22 (9): 2302–15. https://doi.org/10.1175/2008JCLI2117.1.

Rex, Daniel F. 1950. “Blocking Action in the Middle Troposphere and Its Effect upon Regional Climate.” *Tellus* 2 (4): 275–301. https://doi.org/10.1111/j.2153-3490.1950.tb00339.x.

Rigor, Ignatius G., Roger L. Colony, and Seelye Martin. 2000. “Variations in Surface Air Temperature Observations in the Arctic, 1979–97.” *Journal of Climate* 13 (5): 896–914. https://doi.org/10.1175/1520-0442(2000)013<0896:VISATO>2.0.CO;2.

Rolph, Glenn, Ariel Stein, and Barbara Stunder. 2017. “Real-Time Environmental Applications and Display SYstem: READY.” *Environmental Modelling & Software* 95 (September): 210–28. https://doi.org/10.1016/j.envsoft.2017.06.025.

Rutz, Jonathan J., W. James Steenburgh, and F. Martin Ralph. 2014. “Climatological Characteristics of Atmospheric Rivers and Their Inland Penetration over the Western United States.” *Monthly Weather Review* 142 (2): 905–21. https://doi.org/10.1175/MWR-D-13-00168.1.

Schuenemann, Keah C., John J. Cassano, and Joel Finnis. 2009. “Synoptic Forcing of Precipitation over Greenland: Climatology for 1961–99.” *Journal of Hydrometeorology* 10 (1): 60–78. https://doi.org/10.1175/2008JHM1014.1.

Screen, James A., and Ian Simmonds. 2010. “The Central Role of Diminishing Sea Ice in Recent Arctic Temperature Amplification.” *Nature* 464 (7293): 1334–37. https://doi.org/10.1038/nature09051.

———. 2013. “Exploring Links between Arctic Amplification and Mid-Latitude Weather.” *Geophysical Research Letters* 40 (5): 959–64. https://doi.org/10.1002/grl.50174.

Semmens, Kathryn Alese, Joan Ramage, Annett Bartsch, and Glen E Liston. 2013. “Early Snowmelt Events: Detection, Distribution, and Significance in a Major Sub-Arctic Watershed.” *Environmental Research Letters* 8 (1): 014020. https://doi.org/10.1088/1748-9326/8/1/014020.

Serreze, M C, A P Barrett, J C Stroeve, D N Kindig, and M M Holland. 2009. “The Emergence of Surface-Based Arctic Amplification.” *The Cryosphere*, 9.

Serreze, Mark C. 1995. “Climatological Aspects of Cyclone Development and Decay in the Arctic.” *Atmosphere-Ocean* 33 (1): 1–23. https://doi.org/10.1080/07055900.1995.9649522.

Serreze, Mark C., and Roger G. Barry. 2011. “Processes and Impacts of Arctic Amplification: A Research Synthesis.” *Global and Planetary Change* 77 (1): 85–96. https://doi.org/10.1016/j.gloplacha.2011.03.004.

———. 2014. *The Arctic Climate System*. Second. New York, New York: Cambridge University Press.

Serreze, Mark C., Alex D. Crawford, and Andrew P. Barrett. 2015. “Extreme Daily Precipitation Events at Spitsbergen, an Arctic Island.” *International Journal of Climatology* 35 (15): 4574–88. https://doi.org/10.1002/joc.4308.

Serreze, Mark C., and Jennifer A. Francis. 2006. “The Arctic Amplification Debate.” *Climatic Change* 76 (3–4): 241–64. https://doi.org/10.1007/s10584-005-9017-y.

Serreze, Mark C., Julia Gustafson, Andrew P. Barrett, Matthew L. Druckenmiller, Shari Fox, Jessica Voveris, Julienne Stroeve, et al. 2021. “Arctic Rain on Snow Events: Bridging Observations to Understand Environmental and Livelihood Impacts.” *Environmental Research Letters* 16 (10): 105009. https://doi.org/10.1088/1748-9326/ac269b.

Serreze, Mark C., and Ciaran M. Hurst. 2000. “Representation of Mean Arctic Precipitation from NCEP–NCAR and ERA Reanalyses.” *Journal of Climate* 13 (1): 182–201. https://doi.org/10.1175/1520-0442(2000)013<0182:ROMAPF>2.0.CO;2.

Serreze, Mark C., Jonathan D. Kahl, and Russell C. Schnell. 1992. “Low-Level Temperature Inversions of the Eurasian Arctic and Comparisons with Soviet Drifting Station Data.” *Journal of Climate* 5 (6): 615–29. https://doi.org/10.1175/1520-0442(1992)005<0615:LLTIOT>2.0.CO;2.

Sheridan, Scott C., and Cameron C. Lee. 2011. “The Self-Organizing Map in Synoptic Climatological Research.” *Progress in Physical Geography: Earth and Environment* 35 (1): 109–19. https://doi.org/10.1177/0309133310397582.

Sommer, Lauren, Mose Buchele, Molly Samuel, Patty Wight, Michael Elizabeth Sakas, Amy Mayer, and Nat Herz. 2020. “How Warming Winters Are Affecting Everything.” *NPR*, February 18, 2020. https://www.npr.org/2020/02/18/803125282/how-warming-winters-are-affecting-everything.

Stein, A. F., R. R. Draxler, G. D. Rolph, B. J. B. Stunder, M. D. Cohen, and F. Ngan. 2015. “NOAA’s HYSPLIT Atmospheric Transport and Dispersion Modeling System.” *Bulletin of the American Meteorological Society* 96 (12): 2059–77. https://doi.org/10.1175/BAMS-D-14-00110.1.

Stroeve, Julienne C., Mark C. Serreze, Marika M. Holland, Jennifer E. Kay, James Malanik, and Andrew P. Barrett. 2012. “The Arctic’s Rapidly Shrinking Sea Ice Cover: A Research Synthesis.” *Climatic Change* 110 (3–4): 1005–27. https://doi.org/10.1007/s10584-011-0101-1.

Stull, Roland B. 2000. *Meteorology for Scientists and Engineers*. Second Edition. Belmont, CA: Brooks/Cole, Cengage Learning.

Trubilowicz, Joel W., and R. Dan Moore. 2017. “Quantifying the Role of the Snowpack in Generating Water Available for Run-off during Rain-on-Snow Events from Snow Pillow Records.” *Hydrological Processes* 31 (23): 4136–50. https://doi.org/10.1002/hyp.11310.

Tsukernik, Maria, David N. Kindig, and Mark C. Serreze. 2007. “Characteristics of Winter Cyclone Activity in the Northern North Atlantic: Insights from Observations and Regional Modeling.” *Journal of Geophysical Research: Atmospheres* 112 (D3). https://doi.org/10.1029/2006JD007184.

US Department of Commerce, NOAA. n.d. “Full Weather Glossary.” NOAA’s National Weather Service. Accessed February 2, 2022. https://www.weather.gov/otx/Full_Weather_Glossary.

Viñas, Kelsey Simpkins, Maria-Jose. n.d. “Arctic Winter Warming Events Becoming More Frequent, Longer-Lasting.” Climate Change: Vital Signs of the Planet. Accessed February 10, 2022. https://climate.nasa.gov/news/2605/arctic-winter-warming-events-becoming-more-frequent-longer-lasting.

Wallace, John M., and Peter V. Hobbs. 2006. *Atmospheric Science: An Introductory Survey*. Second Edition. Burlington, MA; San Diego, CA; London, UK: Academic Press, an imprint of Elsevier.

“What Is NetCDF? | National Snow and Ice Data Center.” n.d. Accessed December 1, 2021. https://nsidc.org/support/faq/what-netcdf.

Woollings, Tim, David Barriopedro, John Methven, Seok-Woo Son, Olivia Martius, Ben Harvey, Jana Sillmann, Anthony R. Lupo, and Sonia Seneviratne. 2018. “Blocking and Its Response to Climate Change.” *Current Climate Change Reports* 4 (3): 287–300. https://doi.org/10.1007/s40641-018-0108-z.

Zhou, Yang, Travis A. O’Brien, Paul A. Ullrich, William D. Collins, Christina M. Patricola, and Alan M. Rhoades. 2021. “Uncertainties in Atmospheric River Lifecycles by Detection Algorithms: Climatology and Variability.” *Journal of Geophysical Research: Atmospheres* 126 (8): e2020JD033711. https://doi.org/10.1029/2020JD033711.